Structural studies of human CD23 and its complexes

Yuan, Daopeng

Awarding institution:
King's College London

Structural studies of human CD23 and its complexes

Daopeng Yuan

A thesis submitted in partial fulfilment of the requirements for the degree of Doctor of Philosophy in King's College London

Randall Division of Cell and Molecular Biophysics
School of Biomedical Sciences
King's College London
New Hunt's House
Guy's Campus
London
SE1 1UL

August 2012

Abstract

IgE plays a central role in the pathogenesis of immediate hypersensitivity reactions through interacting with its receptors, in particular the high affinity receptor FcεRI. The low-affinity IgE receptor, CD23, affects IgE-dependent immune responses by regulating the synthesis of IgE, facilitating allergen presentation to the immune system, and influencing the activation and differentiation of B- and T-cells. Surprisingly, CD23 is different from other Ig receptors and belongs to the C-type (calcium-dependent) lectin family. Calcium binding to CD23 affects IgE binding to CD23, but previous NMR and crystal structures of CD23 gave conflicting results concerning the calcium binding sites. Investigation of calcium binding site(s) in CD23 and its complexes may assist CD23-targeted drug design.

DerCD23 (a fragment of human CD23 that consists of the lectin domain and part of the C-terminal tail) and derCD23 mutants designed to remove each of the two potential calcium binding sites, were expressed and purified. The crystal structures of Ca^{2+}-bound wild type derCD23, the complex with the Fcε3-4 sub-fragment of IgE-Fc, and four putative calcium binding site mutants of derCD23 were solved. Binding affinities of derCD23 and its mutants for calcium and for IgE-Fc were measured with ITC and SPR. The results indicate a loop of derCD23 (loop 4) is stabilized upon calcium binding to "site 2" and thereby contributes to the increased binding affinity for IgE. In addition, a residue (D258) in the non-conserved "site 1" is observed to bind IgE directly in the Ca^{2+}-bound derCD23/Fcε3-4 complex. Thus, Ca^{2+} bound to site 2 in CD23 stabilizes loop 4 for IgE binding, whereas site 1 has evolved to bind IgE directly.

Clinical studies of IDEC152 (also known as Lumiliximab), a primatized IgG1, anti-CD23 monoclonal antibody (IDEC Pharmaceuticals, San Diego, CA) show positive clinical effects in patients with allergic asthma and chronic lymphocytic leukemia. The Fab fragment of IDEC152 was prepared by enzymatic digestion from IDEC152 and crystals of the complex of derCD23 with IDEC152-Fab were grown, which diffracted to 2.4 Å resolution.

Acknowledgement

I would firstly like to express thanks and gratitude to my supervisors, Brian Sutton and Andrew Beavil, for providing me with the opportunity to work in their laboratories, and for their patient guidance and encouragement through my studies. I am grateful for their analysis of my research training needs and suggestions on research skills development.

This work would not have been possible without the help from Balvinder Dhaliwal for crystallography and many other experiments. I particularly want to thank James McDonnell for his help in SPR and NMR experiments. I would like to say many thanks to Anthony Keeble for his help with ITC experiments.

I am indebted to a number of other people for their help, suggestions and advice on my project. I would like to thank Rebecca Beavil, Michael (Wen-Pin) Kao, Marie Pang, Nyssa Drinkwater, Anna Davies, Louisa James, Rosaleen Calvert, Ali Cooper and Norhakim Yahya.

I would like to thank my office mates: Heather Bax, Yih-Chih Chan, Tihomir Dodev, Faruk Ramadani, Mary Holdom and people in other offices: Hannah Gould, Saba Shakib, Philip Hobson, Seema Agrawal, Holly Bowen, Clare Harper, Katy Ginger, Sakshi Khosa. They helped me with so many things.

Finally, I would like to thank my wife, Danping Liu, for her support on anything I want to do.

Table of contents

List of figures

List of tables

Abbreviations

Å	Angstrom (10^{-10} meters)
ADAM10	A disintegrin and metalloproteinase
APC	Antigen presenting cell
ASGPR-I	Asialoglycoprotin receptor
CD21	Complement receptor type 2 (CR2)
CD23	Low affinity IgE receptor or FcεRII
CD40L	CD40 ligand
CTLD	C-type lectin-like domain
C-type	Calcium dependent
Cγ	Constant domain of IgG
Cε	Constant domain of IgE
D1, D2	Domain 1, domain 2
Da	Dalton
derCD23	16 kDa CD23 fragment
E. coli	*Escherichia Coli*
EMPD	Extracellular membrane proximal domain
EPT	Residues 249-251 of CD23 (Glu-Pro-Thr)
Fab	Fragment antigen binding
FAP	Facilitated antigen presentation
F_{calc}	Calculated structure factor amplitudes
Fcε3-4	Fc sub-fragment of IgE consisting of the dimer of Cε3 and Cε4 domains
FcεRI	High affinity IgE receptor

γ-chain	Immunoglobulin G heavy chain
ε-chain	Immunoglobulin E heavy chain
IDEC152	A primatized IgG1, known as Lumiliximab
Ig	Immunoglobulin
IgE	Immunoglobulin E
IgE-Fc	Fc fragment of IgE consisting of the dimer of Cε2, Cε3 and Cε4 domains
IgG	Immunoglobulin G
IgG-Fc	Fc fragment of Immunoglobulin G
IgM	Immunoglobulin M
IL	Interleukin
IL-13	Interleukin-13
IL-4	Interleukin-4
IPTG	Isopropyl-beta-D-1-thiogalactopyranoside
ITC	Isothermal Titration Calorimetry
K_A	Association equilibrium constant
K_D	Dissociation equilibrium constant
MAN	Mannose
MBP	Mannose binding protein
NAG	N-acetyl-glucosamine
NCS	Non-crystallographic symmetry
NMR	Nuclear magnetic resonance
°C	Celsius degrees
PCR	Polymerase chain reaction
PDB	Protein Data Bank

R_{free}	Reliability factor calculated on a test set
R_{work}	Reliability factor calculated on a working set
RMSD	Root mean square deviation
SDS	Sodium dodecyl sulphate
SPR	Surface Plasmon Resonance
T_H1	T helper 1 subset of T cells
T_H2	T helper 2 subset of T cells
TriCD23	Trimeric CD23

Chapter 1:
Introduction

1.1 Background

The term allergy was introduced about one hundred years ago (Jackson, 2001). Allergy is a modern disease that is mainly found in developed countries. The type I hypersensitivity reaction is caused by harmless environmental substances and results in an inflammatory response. Although scientists and clinicians have developed many approaches to combat this disease, the number of patients with this disease is still increasing. Reasons for the increase may be excessive cleanliness, severe virus infections, vaccinations and pollution, although it is still unclear.

IgE plays an important role in allergic disease (Sutton and Gould, 1993). There are two principal receptors for it: FcεRI (high-affinity Fc receptor) and FcεRII or CD23 (low-affinity Fc receptor). Although structures of IgE-Fc and interactions with FcεRI have been well characterised (section 1.2.2), there is no structural study of the CD23/IgE complex, and the role calcium plays in CD23 binding to IgE is still not clear.

1.2 IgE

1.2.1 IgE in allergy and asthma

It is well established that the role of IgE in allergic diseases is mediated through its interactions with two receptors: FcεRI and CD23. The central function of IgE is performed by interaction with FcεRI on mast cells, APCs (antigen-presenting cells) in mucosal tissues and basophils in the blood. The synthesis of IgE in B cells follows heavy-chain class switching from IgM to IgE, either directly or via IgG. On mast cells and basophils, crosslinking of the FcεRI-bound IgE by allergen mediates immediate hypersensitivity that is the hallmark of an allergic response. Cytokines and chemokines

are liberated and involve recruitment and activation of inflammatory cells. Crosslinking of the FcεRI-bound IgE by allergen on APCs, which express both FcεRI and CD23, leads to the presentation of allergen to the immune system. T_H2 cells and mast cells produce IL-4, IL-13 and CD40L, which in turn promote IgE synthesis by B cells (Figure 1.1) (Gould and Sutton, 2008). The low-affinity receptor of IgE, CD23 is involved in regulating IgE synthesis and the processing of allergen for presentation of peptides to T cells (Section 1.3.2).

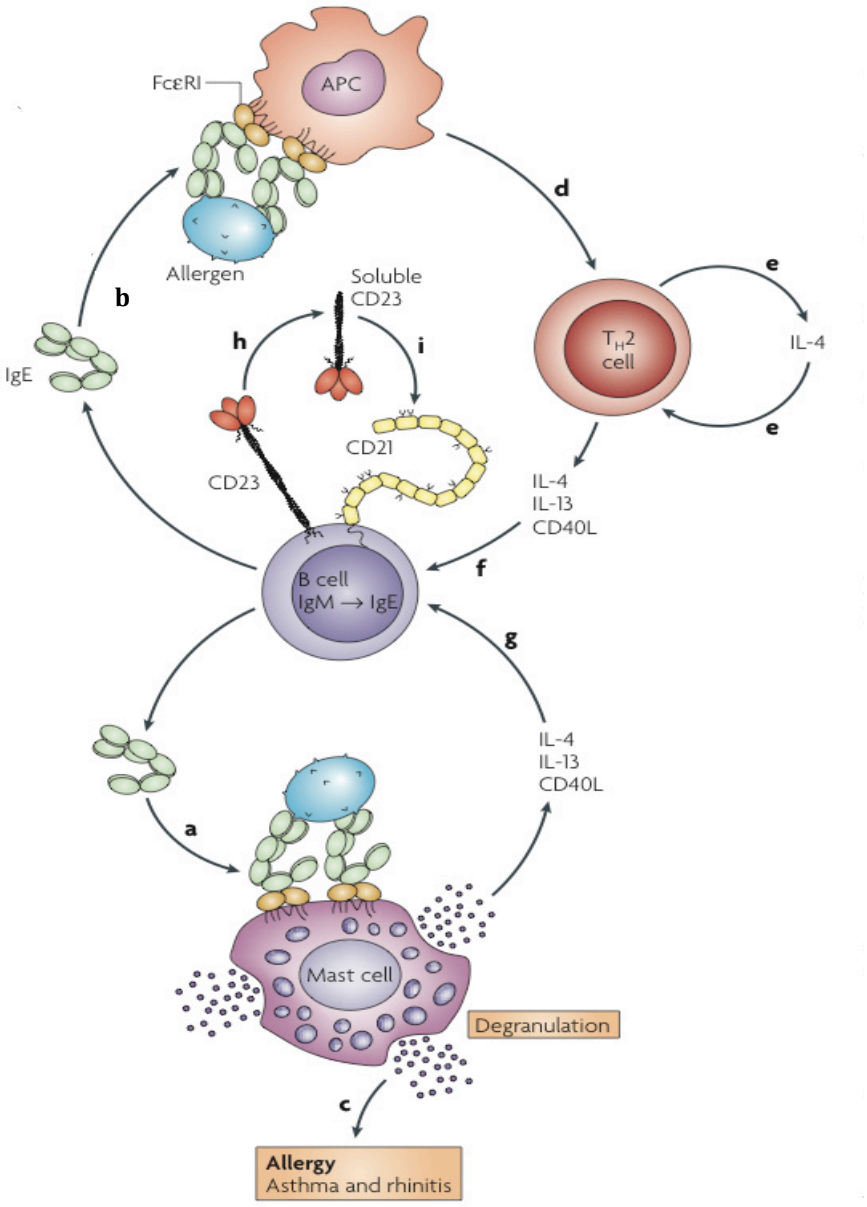

Figure 1.1 Pathway of IgE-mediated allergic responses.
Expression of IgE by B cells requires heavy-chain class switching from IgM to IgE. Secreted IgE binds to FcεRI on mast cells, basophils and APCs to sensitize these cells (**a** and **b**). Allergen crosslinks FcεRI-bound IgE on mast cells and triggers degranulation to cause allergic responses (**c**). Crosslinking of FcεRI-bound IgE by allergen on APCs leads to the presentation of allergen to the immune system (**d**). T_H2 cells secreted interleukin-4 (IL-4) is involved in maintaining the T_H2 lineage and recruiting more T_H cells into the lineage (**e**). T_H2 cells and mast cells produce IL-4, IL-13 and CD40L, and stimulate heavy-chain class switching to IgE and expression of CD23 (**f**, **g** and **h**). Human CD23 regulates IgE synthesis through interaction with CD21 (**i**). (Figure adapted from Gould and Sutton, 2008)

1.2.2 Structures of IgE

1.2.2.1 Domain structures of IgE

As one of five major antibody isotypes (IgA, IgD, IgE, IgG, and IgM) found in mammals, IgE was named in 1968 (Stanworth, 1993). IgE exists in both soluble and membrane-bound form. The membrane-bound form of IgE contains an additional extracellular membrane proximal domain (EMPD) and transmembrane sequence compared to the soluble IgE (Bestagno *et al*., 2001; Gould and Sutton, 2008). Soluble IgE consists of two heavy chains and two light chains, and the heavy ε-chain contains one more immunoglobulin domain than the γ-chain of IgG (Figure 1.2) (Gould and Sutton, 2008).

IgE consists of an Fc region (Cε2, Cε3, Cε4) and two identical Fab fragments. IgE-Fc has the ability to bind two receptors (FcεRI and CD23), whereas the Fab sub-fragment is the antigen-binding fragment. IgE-Fc can be truncated to produce smaller fragments for structural study, such as Fcε3-4, and the Cε3 and Cε2 domains. Fcε3-4 consists of only the Cε3 and Cε4 domains as a disulphide-linked dimer. The disulphide bridge (between residues 328 in each chain) in Fcε3-4 does not exist in the full IgE-Fc, which has two "crossed" disulphide bridges between residues 241 and 328 (Section 1.2.2.3). In contrast, the hinge regions of IgG subclasses contain parallel disulphide bridges, and intra-chain disulphides in the hinge of some IgG4 immunoglobulins (Aalberse and Schuurman, 2002; Kessler *et al*., 1991). The high mannose type carbohydrate composition of the IgE-Fc is not required for binding to receptors (Basu *et al*., 1993; Bjorklund *et al*., 1999; Geha *et al*., 1985; Helm *et al*., 1988). This is also different from the high dependence of receptor binding on the complex-type glycosylation in IgG (Mimura *et al*., 2001; Tao and Morrison, 1989).

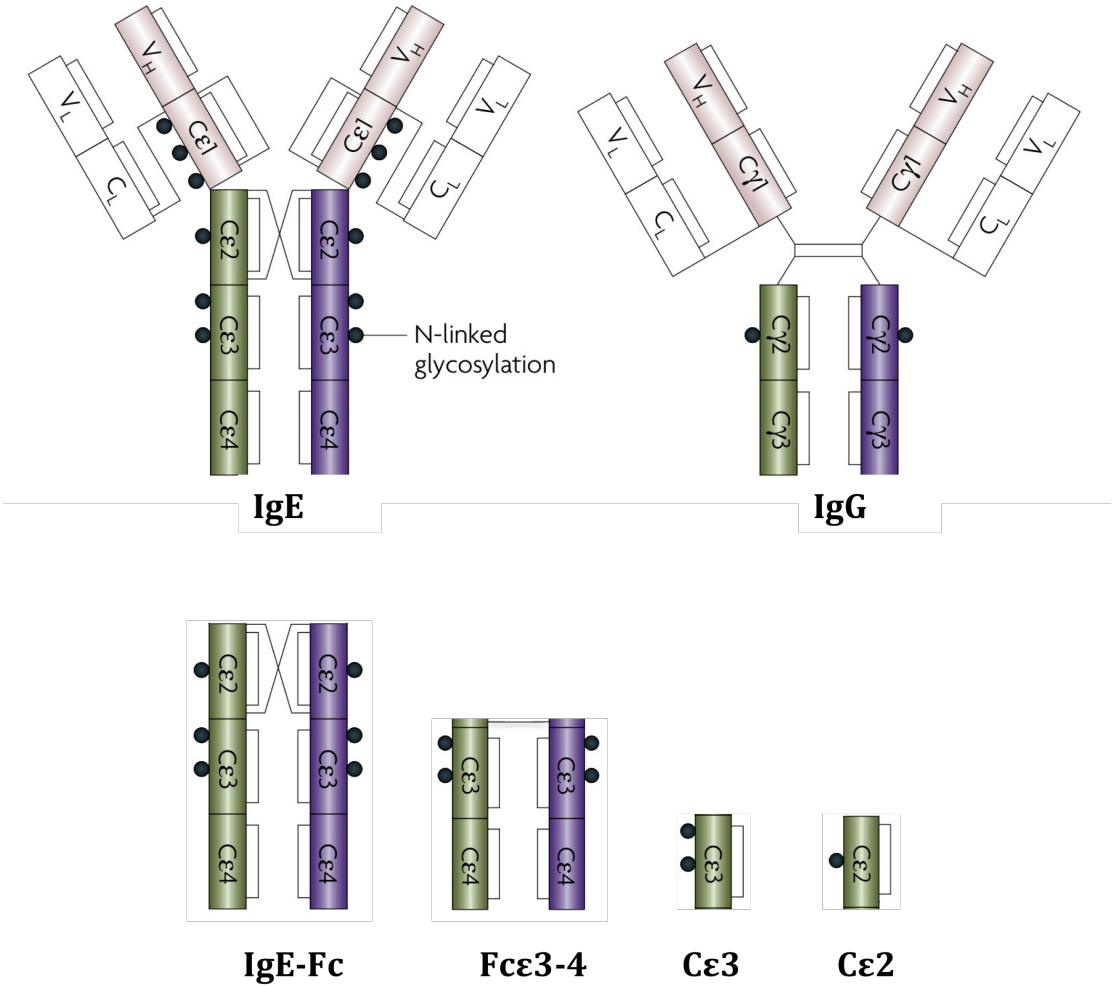

Figure 1.2 Schematic representations of the domain structures of human IgE and IgG. IgE-Fc consists of Cε2, Cε3 and Cε4. IgE-Fc can be truncated to produce smaller fragments for structural study, such as Fcε3-4, and the Cε3 and Cε2 domains. IgG-Fc has only two domains (Cγ2 and Cγ3) and a flexible hinge which takes the place of the Cε2 in IgE. Disulphide bridges and sites of N-linked glycosylation are indicated as black lines and dots, respectively. (Figure adapted from Gould and Sutton 2008)

1.2.2.2 Structure of Fcε3-4

The crystal structure of Fcε3-4 confirms that this domain pair is homologous to Fcγ2-3 in the IgG-Fc. However, Fcε3-4 appears much more compact than the Fcγ2-3 as a result of a smaller angle between Cε3 and Cε4 (Wurzburg *et al.*, 2000). Comparison of this single Fcε3-4 molecule (closed) with the one (open) in complex with FcεRI reveals a conformational flexibility (Figure 1.3). Fcε3-4 also exhibits flexibility *within* Cε3, compared with less structural flexibility of Cγ2 in Fcγ2-3.

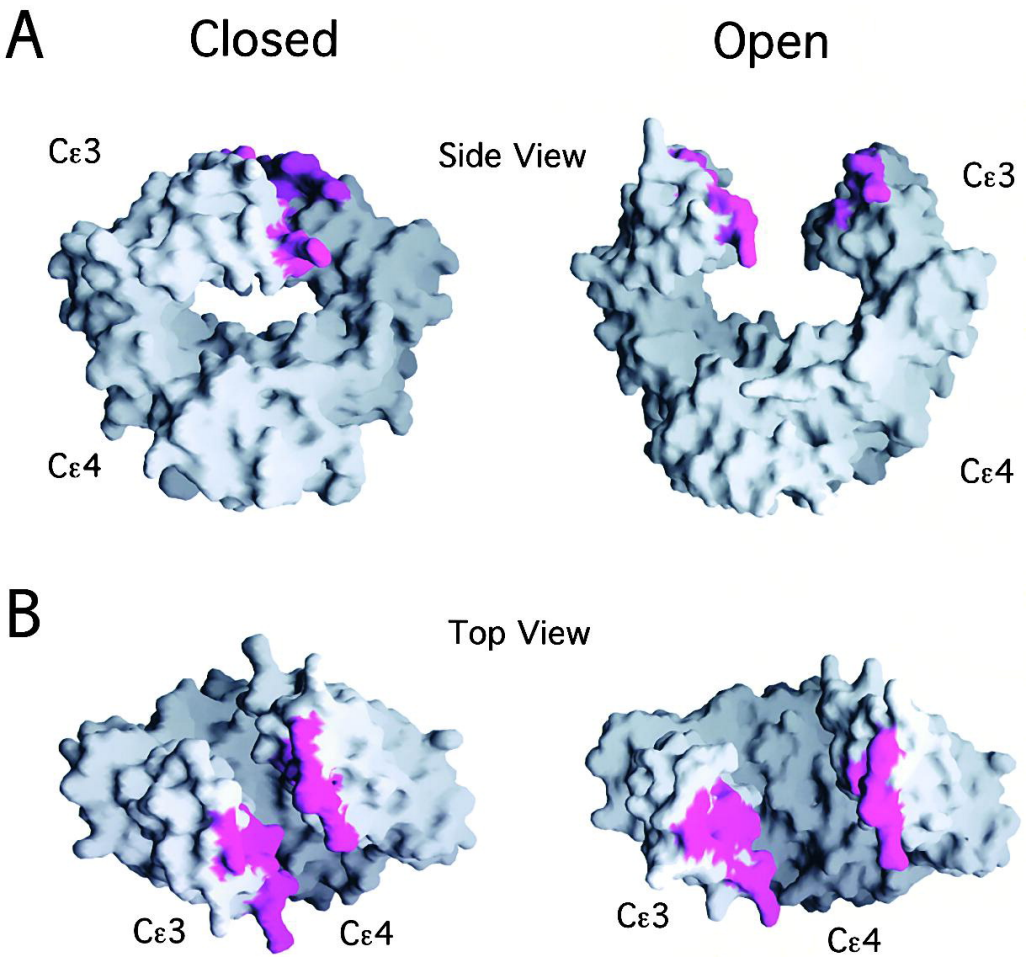

Figure 1.3 Surface representation of the "closed" and "open" conformations of Fcε3-4 structures (PDB code 1FP5 and 1F6A).
A: Side view of the "closed" conformation of uncomplexed Fcε3-4 and "open" conformation in complex with FcεRI (FcεRI not shown). B: Top view of "closed" and "open" conformations of Fcε3-4 structures. FcεRI-binding residues are coloured as magenta. (Figure taken from Wurzburg *et al*., 2000)

1.2.2.3 Structure of IgE-Fc

The structure of Cε2 was solved by nuclear magnetic resonance (NMR) after publication of the crystal structure of Fcε3-4. A combination of this structure with biophysical studies revealed many clues to the role of Cε2 domain in allergic reactions (McDonnell *et al*., 2001). Then the structure of the IgE-Fc was determined by X-ray crystallography (Wan *et al*., 2002). The IgE-Fc structure has one Cε2 domain that makes extensive contacts with both Cε3 and Cε4 domains, whereas the other Cε2 has

few contacts with Fcε3-4 (Figure 1.4). The acutely bent conformation of IgE-Fc confirms previous analytical ultracentrifuge results showing one Cε2 binding to one Fcε3-4 (McDonnell *et al*., 2001). The interface between the two Cε2 domains is different to the earlier predicted models (Helm *et al*., 1991; Padlan and Davies, 1986). The two Cε2 domains are disulfide-linked between C241 and C328 in a "crossed" arrangement.

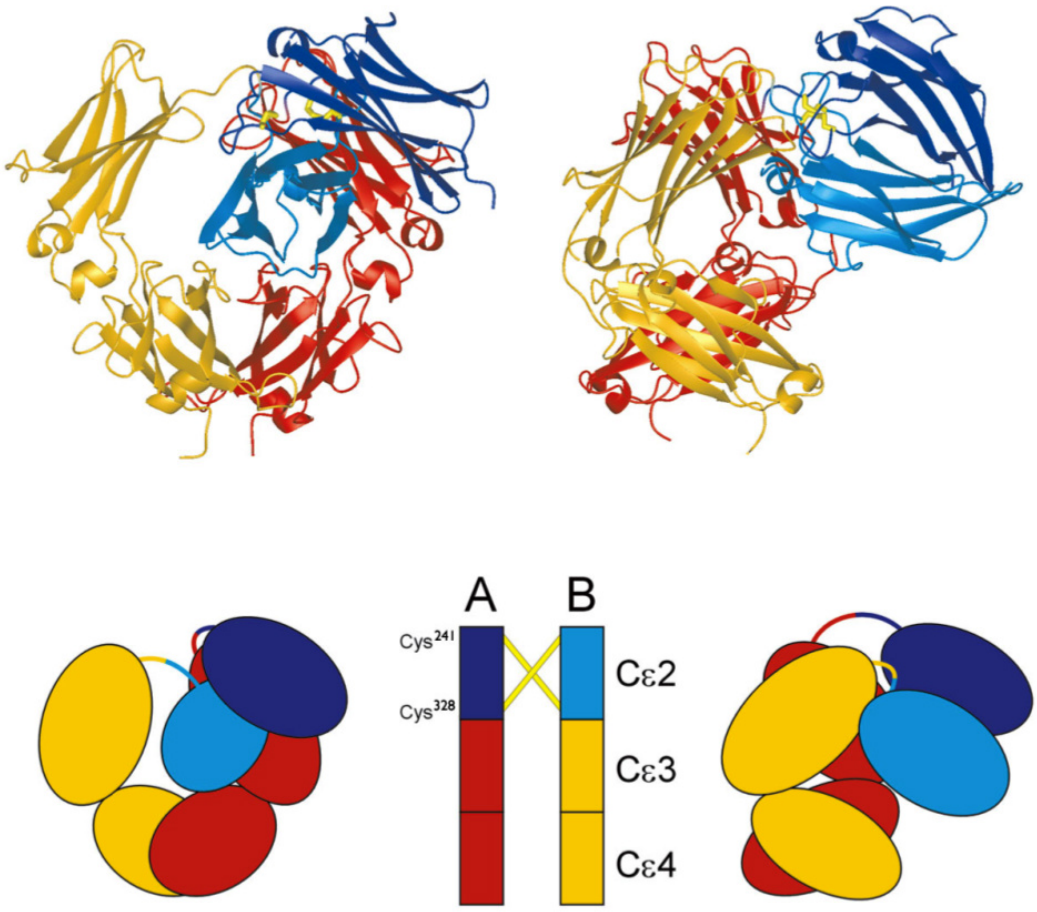

Figure 1.4 Structure of IgE-Fc (PDB code 1O0V).
Front and side views of IgE-Fc in cartoon and schematic representation. Inter-chain disulphides are shown in yellow. (Figure taken from Wan *et al*., 2002)

Comparison of the IgE-Fc structure with uncomplexed and complexed Fcε3-4 reveals further asymmetry. The Fcε3-4 region of IgE-Fc adopts a conformation that differs from both the "closed" and "open" conformations (Figure 1.5). One Cε3 domain in IgE-Fc adopts a "closed" conformation by contact with a Cε2 domain, whereas the other Cε3 domain is in an "open" conformation.

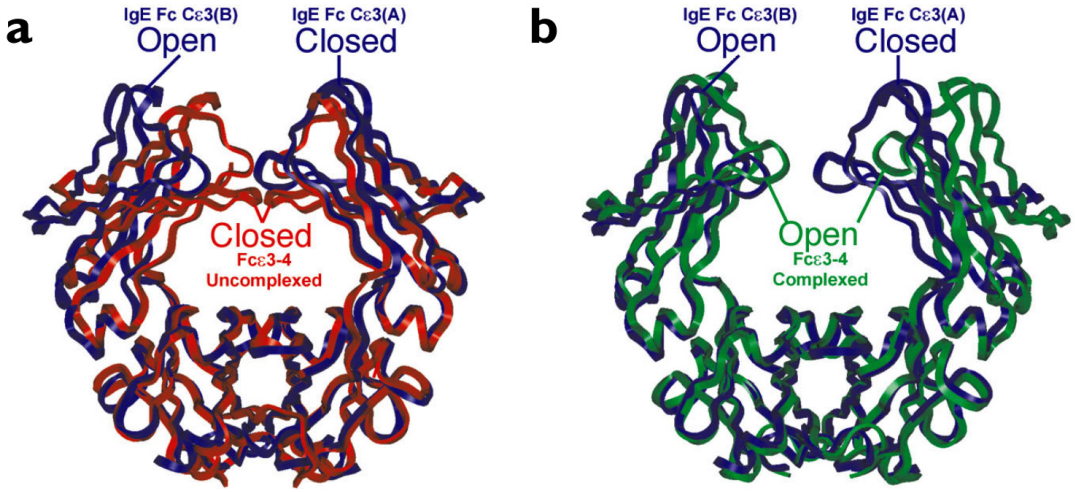

Figure 1.5 Comparison of the Fcε3-4 region in the full IgE-Fc structure (PDB code 1O0V) with the "closed" and "open" conformations of Fcε3-4 (PDB code 1FP5 and 1F6A). Fcε3-4 of the IgE-Fc, "closed" and "open" Fcε3-4 structures are shown as blue, red and green respectively. (Figure taken from Wan *et al*., 2002)

1.2.2.4 Structure of IgE-Fc in complex with FcεRI

The complex of IgE-Fc with the soluble, extracellular domains of the α-chain of FcεRI was reported recently (Holdom *et al*., 2011). The FcεRI bound IgE-Fc has a more acutely bent structure than the structure of free IgE-Fc (Figure 1.6). Cε2 domains have no direct contact with the FcεRI in this even more acutely bent IgE-Fc structure. However, the non-contacting Cε2 domains enhance stabilization of the complex, which is supported by thermodynamic analysis (Holdom *et al*., 2011).

Comparison of all free or FcεRI-bound IgE-Fc and Fcε3-4 structures reveal the flexibility of Cε3. As the binding site of both FcεRI and CD23 (Section 1.4.1), Cε3 exhibits unusual flexibility that may be required for interaction with these two IgE receptors (Wurzburg *et al*., 2000).

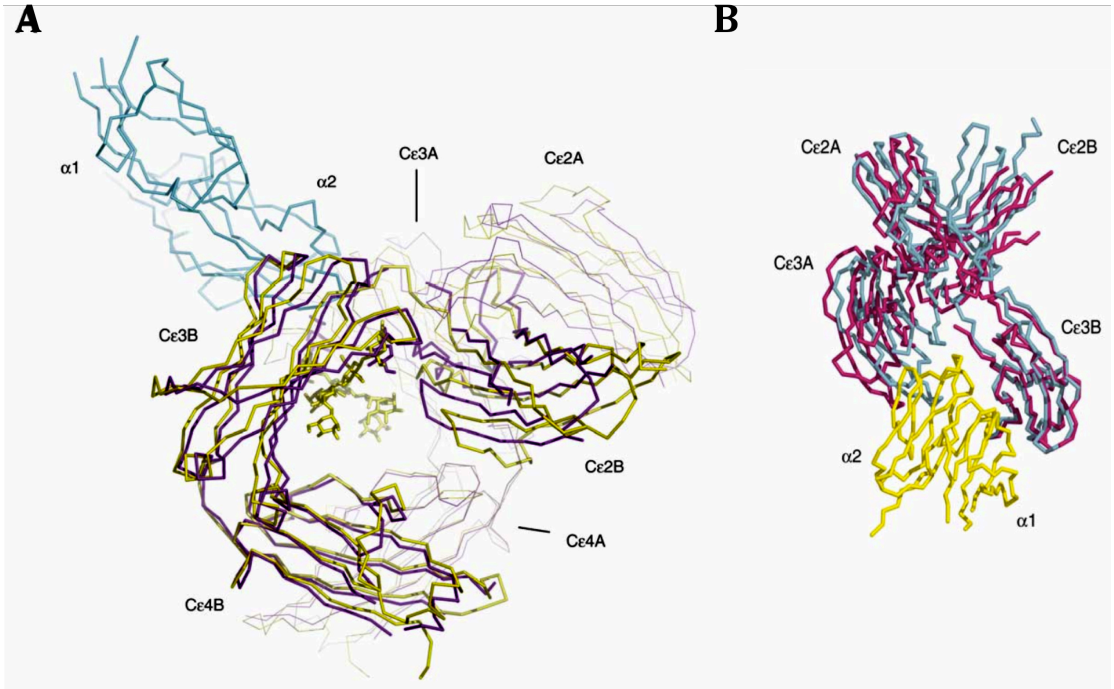

Figure 1.6 Comparison of the full IgE-Fc structure (PDB code 1O0V) with the IgE-Fc in IgE-Fc/FcεRI complex (PDB code 2Y7Q).
The FcεRI bound IgE-Fc is more acutely bent than free IgE-Fc. A: Free IgE-Fc (with carbohydrate) is shown as yellow. FcεRI and FcεRI-bound IgE-Fc are shown as blue and purple respectively. B: Cε4 domains are hidden in this view. Free IgE-Fc, FcεRI and FcεRI bound IgE-Fc are shown as light blue, yellow and pink respectively. (Figure taken from Holdom *et al*., 2011)

1.3 CD23

1.3.1 CD23 expression

The low-affinity IgE receptor, CD23, was discovered over 30 years ago (Gonzalez-Molina and Spiegelberg, 1976; Lawrence *et al*., 1975). There are two forms of CD23 (CD23a and CD23b) that differ by 6 or 7 amino acids at the N-terminal (intracellular) sequence (Gould and Sutton, 2008; Yokota *et al*., 1988). They are present on various cell types, including macrophages, monocytes, eosinophils, platelets, follicular dendritic cells, B cells and T cells (Capron *et al*., 1981; Delespesse *et al*., 1991; Melewicz *et al*., 1982; Sarfati *et al*., 1986). CD23 is also expressed on some epithelial cells (Billaud *et al*., 1989). In addition to expression in this wide range of cell types, CD23 is treated as a disease marker playing important roles in many different diseases: atopy, autoimmunity and chronic lymphocytic leukemia (Gordon, 1991).

1.3.2 Functions of CD23

1.3.2.1 Regulation of IgE synthesis

IgE-sensitized APCs bind allergen via FcεRI, but CD23 also facilitaes allergen presentation by binding IgE/allergen complexes; both processes lead to the presentation of allergen to T helper 2 (T_H2) cells. This promotes IgE synthesis by B cells through producing IL-4 and IL-13 (Miescher and Vogel, 2002). T_H2 cells express CD40L, which together with IL-4 promote IgE synthesis by stimulating heavy-chain class switching to IgE (Gould and Sutton, 2008).

CD23 and CD21 molecules are also involved in regulating IgE synthesis (Bonnefoy *et al*., 1996; Gould and Sutton, 2008; Gould *et al*., 2003). CD23 plays a central role in IgE synthesis, and a model has been proposed as described below (Gould and Sutton, 2008) (Figure 1.7). A soluble, trimeric form of cleaved membrane CD23 upregulates IgE synthesis by co-ligation of membrane bound IgE and CD21 (Cooper *et al*., 2012). However, monomeric soluble CD23, cleaved by proteases such as *Der p* I (house dust mite protease), has opposite effects on IgE regulation (Bonnefoy *et al*., 1996; Gould *et al*., 2003; McCloskey *et al*., 2007). Membrane CD23 and membrane IgE are co-ligated by allergen-IgE complexes in negative signalling for IgE synthesis. Previous experiments using inhibitors of CD23 proteolysis and CD23-specific antibodies showed decreased IgE levels (Gould and Sutton, 2008; McCloskey *et al*., 2007; Rosenwasser and Meng, 2005). Thus, CD23 can be a promising therapeutic target for the treatment of allergic diseases.

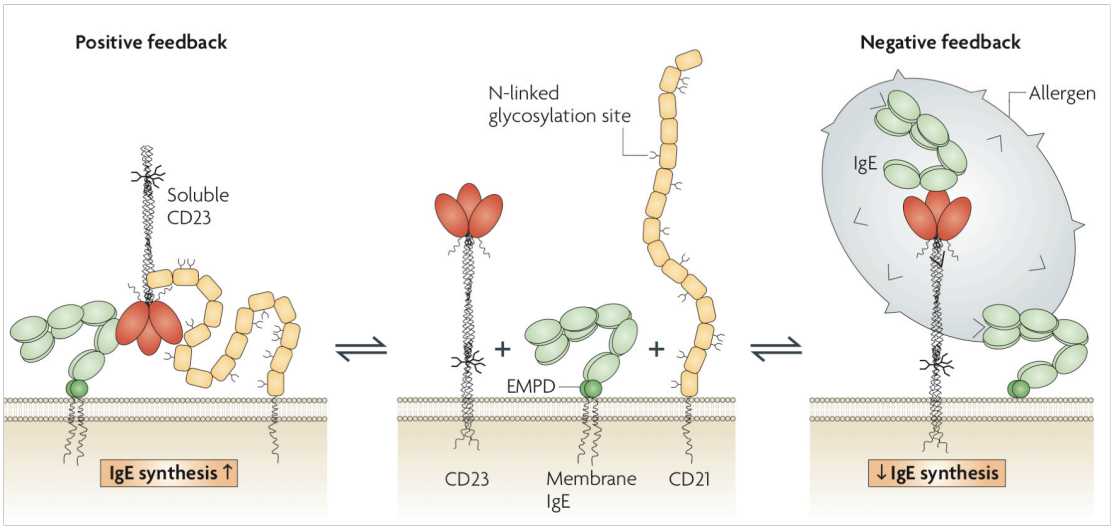

Figure 1.7 Positive and negative regulation of IgE by CD23.
Co-ligation of membrane bound IgE and CD21 on a human B cell by soluble trimeric CD23 leads to positive regulation of IgE synthesis. Membrane bound CD23 delivers a negative signal for IgE synthesis by the co-crosslinking of membrane CD23 and membrane IgE by an allergen-IgE complex. EMPD: extra-cellular membrane-proximal domain. CD21, a member of the complement system, has domains 1-2 and 5-8 involved in the binding to CD23 (Section 1.5). (Figure taken from Gould and Sutton, 2008)

1.3.2.2 Other functions of CD23

APCs express both FcεRI and CD23, crosslinking of the FcεRI-bound IgE by allergen on APCs leads to the presentation of processed allergen to the T cells, and CD23 is involved in allergen presentation by facilitating internalisation of IgE-allergen complexes (Carlsson *et al*., 2007; Gould and Sutton, 2008). In addition, CD23 contributes to the spreading of sensitivity to a single allergen to unrelated allergens in allergen presentation (Gould and Sutton, 2008; Mudde *et al*., 1995).

CD23 also plays important roles in transporting allergen-IgE complexes across epithelial barriers in the gut and airways (Gould and Sutton, 2008; Palaniyandi *et al*., 2011; Tu *et al*., 2005). CD23, expressed on intestinal or airway epithelial cells, captures allergen-IgE complexes on the luminal side and transports them into the mucosa. The transported allergen may then crosslink FcεRI-bound IgE on mast cells to cause degranulation, and on APCs to present allergen to the immune system.

CD23 is also involved in the germinal centre reaction to rescue selected B cells from apoptosis (Bonnefoy *et al*., 1993; Gould *et al*., 2003; Liu *et al*., 1991), and in monocyte activation in inflammation through interactions with CD18/CD11b and CD18/CD11c (Lecoanet-Henchoz *et al*., 1995).

1.3.3 Structure of CD23

1.3.3.1 Membrane bound CD23 and its soluble fragments

This 45 kDa molecular weight type II integral membrane protein, whose carboxy-terminus is outside the membrane, is different from other Ig receptors and belongs to the C-type lectin family (Kikutani *et al*., 1986; Kintner and Sugden, 1981; Thorley-Lawson *et al*., 1986). The C-type lectin family is a group of calcium dependent and carbohydrate binding proteins (Zelensky and Gready, 2005). The extracellular sequence of membrane-bound CD23 consists of an α-helical coiled-coil stalk, C-type lectin head domain, C-terminal tail and N-linked glycosylation (Figure 1.8) (Beavil *et al*., 1992; Gould and Sutton, 2008). The C-terminal tail is absent in the mouse form of CD23, which also has a shorter stalk region (Beavil *et al*., 1992).

The stalk region can be cleaved to release soluble CD23 by various proteases, such as ADAM10 that is a disintegrin and metalloproteinase (Lemieux *et al*., 2007; Weskamp *et al*., 2006). CD23 can also be cleaved by the house dust mite allergen *Der p* I (Schulz *et al*., 1995). Monomeric derCD23, S156-E298 of the full-length CD23, is a recombinant protein corresponding to the fragment released by *Der p* I which contains the lectin domain and part of the C-terminal tail (Schulz *et al*., 1997). TriCD23 is a recombinant trimeric CD23 which consists of the lectin domain, C-terminal tail, part of the coiled-coil stalk and a synthetic isoleucine zipper motif to form a high affinity trimer. Monomeric CD23 binds to IgE with relatively low affinity ($K_A \approx 10^6$-10^7 M^{-1}) (Dierks *et al*., 1993), but trimeric CD23 binds to IgE with higher affinity ($K_A \approx 10^8$-10^9 M^{-1}) (McCloskey *et al*., 2007; Hibbert *et al*., 2005). This avidity effect is due to the combined strength of multiple bond interactions through more than one head domain.

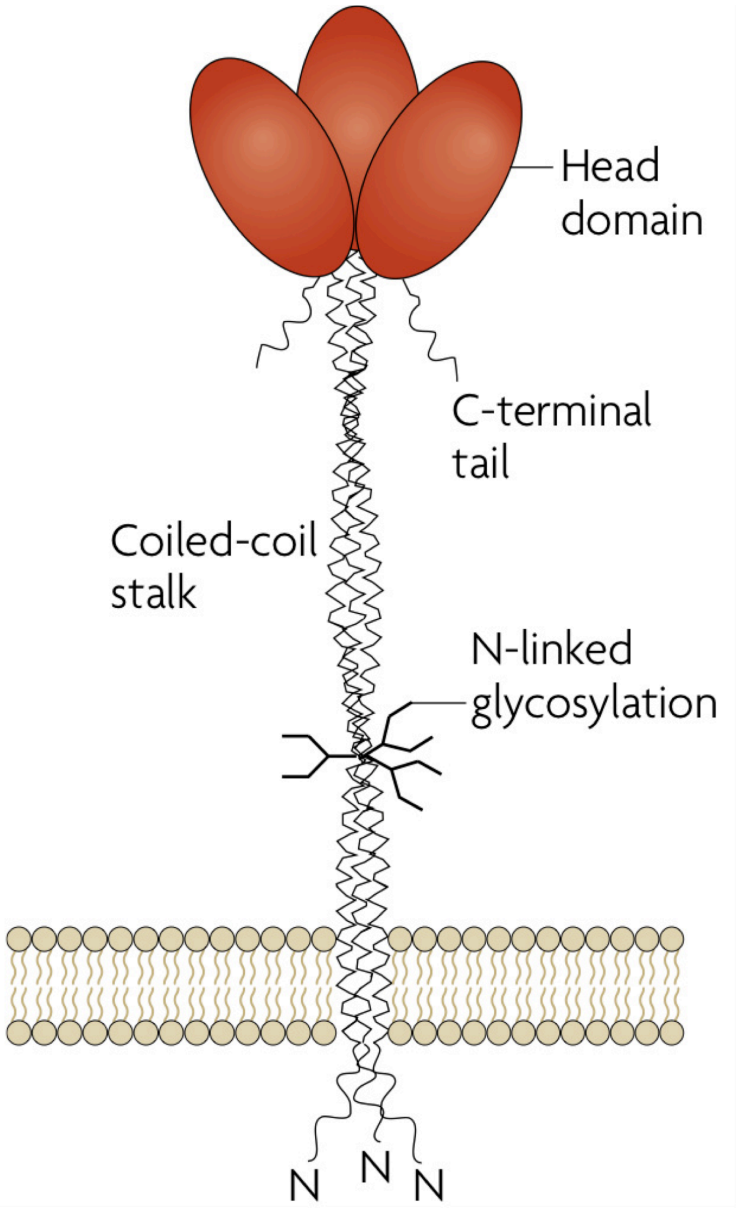

Figure 1.8 A schematic presentation of membrane-bound CD23.
The extracellular sequence of membrane-bound CD23 consists of an α-helical coiled-coil stalk, C-type lectin head domain, C-terminal tail and N-linked glycosylation. (Figure taken from Gould and Sutton, 2008)

1.3.3.2 Three-dimensional structure of CD23 head domain

Initially, the structure of the CD23 head domain was modelled based on the crystal structure of rat mannose binding protein (MBP) and E-selectin (Bajorath and Aruffo, 1996; Padlan and Helm, 1993; Schulz *et al*., 1997). Then, the three-dimensional structure of derCD23 (the amino acids from S156 to E298 of human CD23) was solved by nuclear magnetic resonance (NMR) spectroscopy (Hibbert *et al*., 2005). The NMR structure consists of two α helices and eight β strands (Figure 1.9). With NMR titration experiments, chemical shifts suggest calcium "site 1" (Figure 1.10) is the calcium-binding site, including backbone amides for I221, N225, K229, G230, E231, D270, A271, D274 and side-chain amide of N225 (Hibbert *et al*., 2005).

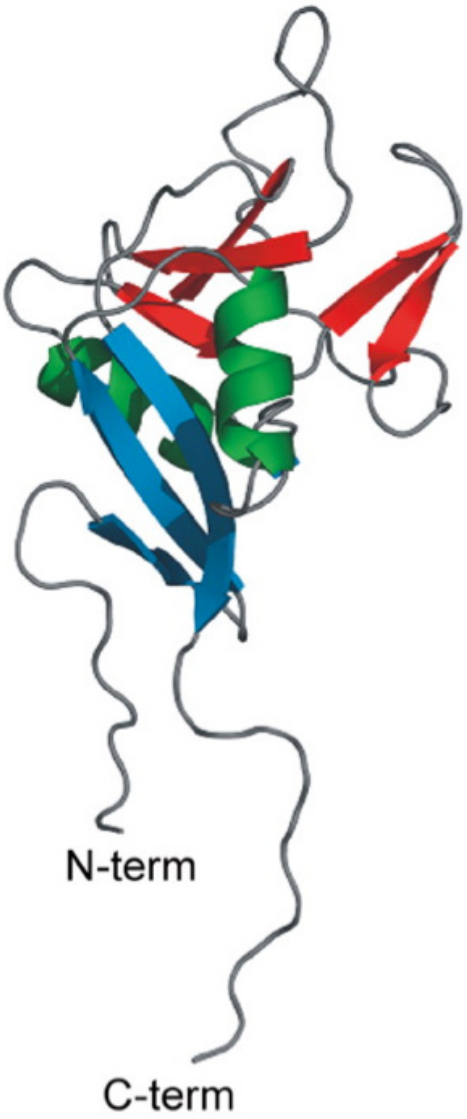

Figure 1.9 Structure of derCD23 determined by NMR.
A cartoon representation of the structure of derCD23 determined by NMR (PDB code 1T8D), with secondary structure identified. (Figure taken from Hibbert *et al*., 2005)

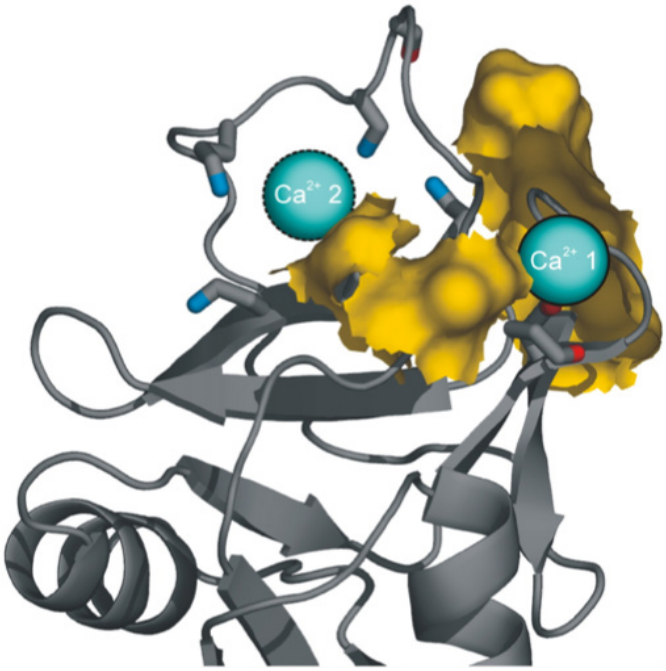

Figure 1.10 The calcium binding site in derCD23 (PDB code 1T8D).
Gray region is the backbone of derCD23. Residues showing substantial chemical shifts in NMR titration experiments with calcium are indicated in yellow. Blue balls are two possible calcium binding sites. (Figure taken from Hibbert *et al*., 2005)

Two crystal structures of human CD23 double mutant (residues 150-321, with two non-silent mutations of H213R and G256S) were determined later by X-ray crystallography, one with calcium and one without calcium (Wurzburg *et al*., 2006). The crystal structure of the CD23 double mutant showed that residues E249, T251, N269 and D270 bind to calcium (Figure 1.11) in contrast to the NMR structure, whereas residue R253 occupies the calcium position in the calcium-free form of the CD23 structure. This indicates calcium "site 2", which is labelled Ca^{2+} 2 in Figure 1.10, is the calcium-binding site. Another unusual feature of the calcium-bound structure is the disordered loop 4 (253-257), which is ordered in the calcium-free structure.

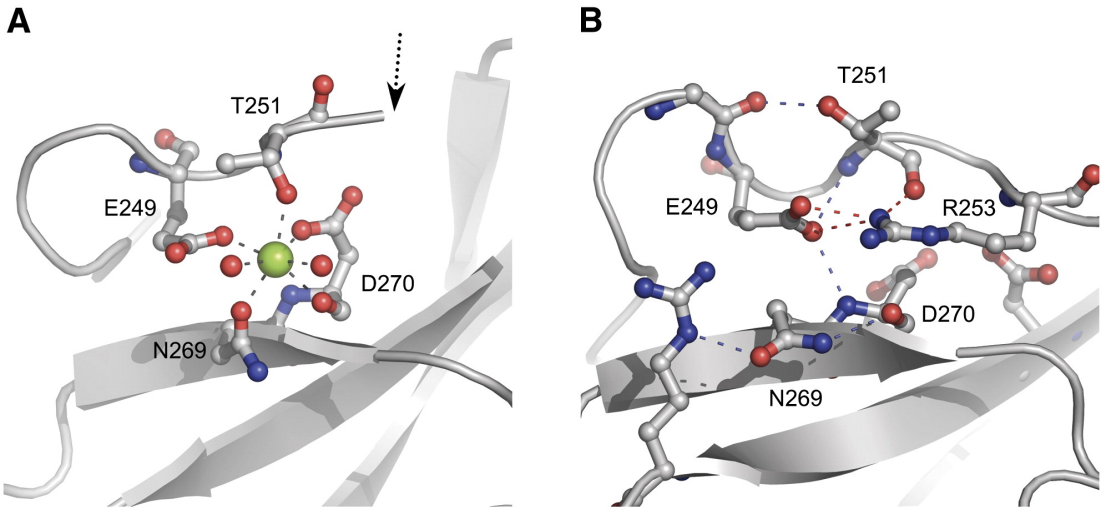

Figure 1.11 The calcium binding site.
A: Calcium bound crystal structure of CD23 (PDB code 2H2T) indicates calcium (green ball) binds to residues E249, T251, N269 and D270. The beginning of missing loop 4 (253-257) is indicated with a black arrow. B: Residue R253 occupies the calcium position in the apo form of the CD23 structure (PDB code 2H2R). (Figure taken from Wurzburg *et al*., 2006)

1.4 CD23 interactions with IgE

1.4.1 CD23 interactions with IgE

It is clear that CD23 plays important roles through interaction with IgE in allergic disease (Gould and Sutton, 2008). Understanding of the CD23-IgE interaction may reveal many aspects of the mechanism of allergic disease and provide a possible target for therapeutic intervention. Although structures of IgE-Fc and CD23 head domain have been reported, no crystal structure has yet been solved for the CD23-IgE complex.

The binding site of CD23 on IgE has been studied using a number of monoclonal antibodies or mutations. Binding of CD23 to IgE was not affected by antibodies that recognized the Cε4 domain or a spanning part of the Cε2 and Cε3 domains, but was inhibited by antibodies that recognized residues 367-376 of Cε3 domain (Chretien *et al*., 1988). CD23 binding on the Cε3 domain was confirmed by a separate study using monoclonal antibodies against Cε2 and Cε3 domains (Vercelli *et al*., 1989). Keegan and coworkers found that antibodies directed at Cε3 and Cε4 prevent the CD23-IgE

interaction (Keegan *et al*., 1991). In addition, a single mutation of Lys352 on Cε3 disrupted the CD23-IgE interaction completely (Sayers *et al*., 2004). Therefore, the binding site of CD23 on IgE is believed to be within Cε3 domain.

The first indication of the IgE binding site on CD23 came in 1989, with mutagenesis and monoclonal antibody binding studies which suggested that residues 165-190 and 224-256 were involved (Bettler *et al*., 1989; Bettler *et al*., 1992). In addition, NMR titration experiments by adding Cε3 to isotopically labelled derCD23 showed residues in the CD23 head domain that were involved in binding to IgE (Hibbert *et al*., 2005). Ultracentrifugation data indicate that both IgE-Fc and Fcε3-4 bind CD23 with a 2:1 stoichiometry (McCloskey *et al*., 2007; Shi *et al*., 1997).

1.4.2 The role calcium plays in CD23 binding to IgE

C-type lectin-like domains (CTLDs) are a large group of proteins with diverse functions. Mannose binding protein (MBP) is a C-type lectin that possesses a calcium-dependent carbohydrate-binding activity (Weis *et al*., 1992). Calcium-dependent structural changes in this protein are well understood, and provide a good model to investigate the role calcium plays in other CTLDs. Calcium stabilizes the structure of loops in MBP that are essential for carbohydrate-binding (Ng *et al*., 1998; Ng and Weis, 1998).

Unlike MBP, CD23 appears to have lost the function to bind carbohydrate, and carbohydrate is not required for CD23 binding to IgE (Hibbert *et al*., 2005; Vercelli *et al*., 1989). However, it was reported that the binding of IgE to CD23 is calcium-dependent (Richards and Katz, 1990). Calcium increases CD23 binding affinity to IgE in SPR experiments 7-fold (Hibbert *et al*., 2005). NMR titration experiments showed that residues I221, N225, K229, G230, E231, D270, A271 and D274 displayed substantial chemical shifts after binding with calcium, while residues W184, R188, Y189, A190, L198, H202, I221, G222, R224, N225, L226, W234, V235, A271, C273, D274, K276, and A279 in derCD23 were involved in binding to the Cε3 domain of IgE

(Hibbert *et al*., 2005). The chemical shifts of some residues were observed in both experiments. According to the two crystal structures and mutagenesis study (Bettler *et al*., 1992) of CD23, loop 1 (226-231) and loop 4 (253-257) are the overlap regions of calcium binding and IgE binding (Figure 1.12) (Wurzburg *et al*., 2006). Taking all this evidence together, calcium is believed to be involved in IgE binding. However, loop 4 is disordered in the calcium-bound structure of CD23 double mutant (Figure 1.11A). This is inconsistent with the role of calcium in stabilizing the loop as seen in other CTLDs (Ng *et al*., 1998; Sun, 2006).

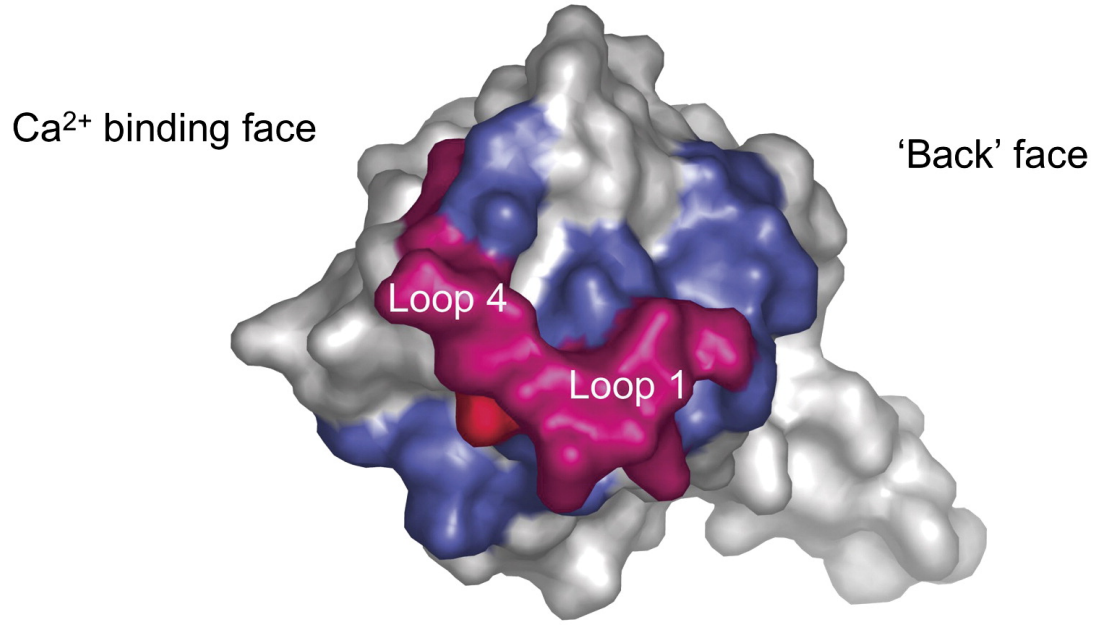

Figure 1.12 overlap regions of calcium binding and IgE binding.
Blue: regions implicated in IgE binding by mutagenesis study.
Red: residues whose positions are different in the apo and calcium bound form of CD23 (PDB code 2H2R and 2H2T). Magenta: the overlap regions of calcium binding and IgE binding. (Bettler *et al*., 1992; Figure taken from Wurzburg *et al*., 2006)

1.5 CD21

CD21, depicted in Figure 1.7, also known as complement receptor type 2 (CR2), belongs to the complement system, a family of soluble proteins and cell surface receptors (Roozendaal and Carroll, 2007). This membrane protein functions as counter-receptor for CD23 to regulate IgE synthesis in the network of allergic disease (Aubry *et*

al., 1992; Sutton and Gould, 1993). Domain1 and Domain2 (D1D2), and also D5-D8 have been implicated in IgE binding (Aubry *et al*., 1992). N-linked carbohydrates on domains 5 to 8 of human CD21 were reported to be involved in the CD23/CD21 interaction (Aubry *et al*., 1994). The binding surface for CD21 D1D2 on derCD23 has already been mapped at the start of the "tail" (residues E294, G295, S296 and E298) by NMR titration experiments (Hibbert *et al*., 2005). Although there are already crystal structures of domains D1 and D2 of CD21 (Prota *et al*., 2002; Szakonyi *et al*., 2001), the complex structure of CD21 with CD23 has not been reported. Since CD23 binds to both CD21 and IgE, it has been hypothesised that CD23 regulates IgE synthesis by forming IgE-CD23-CD21 trimolecular complex on a human B cell (Figure 1.7) (Gould and Sutton, 2008).

1.6 IDEC152

IDEC152 (also known as Lumiliximab) is a primatized, IgG1, anti-CD23 monoclonal antibody (IDEC Pharmaceuticals, San Diego, CA). In clinical trials this antibody resulted in sustained and dose-dependent decreases in serum IgE concentrations (Rosenwasser *et al*., 2003). It was also reported that IDEC152 inhibited allergen-induced responses in antigen-presenting cells and T cells (Poole *et al*., 2005). Thus, it is a potential therapeutic antibody for the treatment of allergic asthma. What is more, IDEC152 is promising therapy for chronic lymphocytic leukemia through binding to CD23 (Byrd *et al*., 2007; Mavromatis and Cheson, 2004). Nothing is known of the IDEC152 binding site on CD23, or any structural details of its mechanism of action.

1.7 Aims of project

a) Although three-dimensional structures of CD23 and IgE have been reported, there are still many important issues concerning the two proteins, which need to be described clearly. Understanding of CD23 and its complexes may lead to CD23-targeted drug design. However, there is a controversy concerning the location of the calcium binding site(s) in CD23, and their roles in IgE binding. The calcium binding sites in the NMR and crystal structures are different from each other. Although it was reported that the

binding of IgE to CD23 is calcium-dependent (Richards and Katz, 1990), there is no three-dimensional structure of the complex to support it. Thus, determining the calcium-binding site of CD23 can help to study the interaction of IgE and CD23. Mutants of derCD23 have been designed to probe the calcium binding site(s) for expression, biophysical analysis by ITC, SPR and for X-ray structure determination.

b) The structures of Fcε3-4 and IgE-Fc with FcεRI (high-affinity receptor) have been determined and exploited for the development of inhibitors of allergic disease (Garman *et al*., 2000; Holdom *et al*., 2011). CD23 is important in the regulation of IgE synthesis (Gould and Sutton, 2008). Thus, determining the structure of Fcε3-4 or IgE-Fc with CD23 may also provide a structural basis for anti-allergy drug design. Because CD23 binds to the Cε3 domain of IgE-Fc (Section 1.4.1), it is possible to attempt to crystallise the complex of derCD23 with the Fcε3-4 part of IgE-Fc.

c) CD23 is a disease marker in atopy, autoimmunity and chronic lymphocytic leukemia. IDEC152 (Lumiliximab) is a primatized, IgG1, anti-CD23 monoclonal antibody. Clinical trials of IDEC152 indicated therapeutic action in allergy and chronic lymphocytic leukemia. Thus, co-crystallisation of IDEC152-Fab with derCD23 will reveal the mechanism of its therapeutic action in allergy and chronic lymphocytic leukemia.

Chapter 2:
Materials and methods

2.1 Materials

2.1.1 Chemicals, reagents

1,6-Hexanediol (Sigma-Aldrich)
Acrylamide/Bis-acrylamide (Severn Biotech Ltd)
Ammonium persulfate (Sigma-Aldrich)
Ammonium sulfate (Sigma-Aldrich)
Ampicillin (Sigma-Aldrich)
Bis-tris-propane (Sigma-Aldrich)
BL21(DE3) Competent Cells (New England Biolabs)
$CaCl_2$ (Fluka)
Cysteine-HCl (Sigma-Aldrich)
DTT (Sigma-Aldrich)
EDTA (BDH)
Ethanol (Sigma-Aldrich)
Glycerol (Sigma-Aldrich)
GuHCl (Sigma-Aldrich)
Hepes (Gibco)
Human IgG (Sigma-Aldrich)
Immobilized Papain slurry (PIERCE)
Isopropyl β-D-1-thiogalactopyranoside (Sigma-Aldrich)
LB agar powder (Invitrogen)
LB powder (Invitrogen)
MES (Sigma-Aldrich)
NaCl (Sigma-Aldrich)
Oxidized glutathione (Sigma-Aldrich)
PEG (Fluka)

Pyridinio propanesulfonate (Sigma-Aldrich)
Potassium thiocyanate (Sigma-Aldrich)
Reduced glutathione (Sigma-Aldrich)
SDS (Severn Biotech Ltd)
SeeBlue® Plus2 molecular weight marker (Invitrogen)
Sodium azide (Sigma-Aldrich)
Surfactant p20 (Sigma-Aldrich)
Streptavidin (Sigma-Aldrich)
TEMED (Sigma-Aldrich)
Tris (Sigma-Aldrich)
Triton-100 (Sigma-Aldrich)
Trizma base (Sigma-Aldrich)
Fcε3-4 was obtained from Dr. Alistair Henry, UCB

2.1.2 Buffers, solutions and media

Coomassie staining buffer: 0.25% coomassie brilliant blue, 7.5% acetic acid, 5% methanol in ddH_2O
Gel de-staining buffer: 10% acetic acid, 40% methanol in ddH_2O
Gel running buffer: 25 mM Tris pH 8.8; 200 mM glycine; 0.1% (w/v) SDS
Heparin loading buffer: 25 mM Tris pH 7.5
Heparin elution buffer: 25 mM Tris pH 7.5, 200 mM NaCl
NMR buffer: 10 mM Tris pH 6.8, 125 mM NaCl, 4 mM calcium chloride
ITC buffer: 10 mM Tris pH 6.8, 125 mM NaCl
Sample buffer for SDS-PAGE: 10% w/v SDS, 10 mM Dithiothreitol, or beta-mercapto-ethanol, 20 % v/v Glycerol, 0.2 M Tris pH 6.8, 0.05% w/v Bromophenol blue

2.2 DNA metheds

2.2.1 Plasmid vectors

The *E.coli* strain BL21(DE3) containing pET5a-derCD23 vector was obtained from Prof. James McDonnell. The pET5a vectors containing derCD23 mutants (E249A, S252A, D258A, D270A) were provided by Dr. Balvinder Dhaliwal.

2.2.2 Site directed mutagenesis

Site directed mutagenesis of derCD23 to produce the mutants N269A and N269D was carried out using QuickChange kit (Stratagene, CA, USA) according to provided protocol. The primers that were used are listed in Table 2.1.

N269A forward	GGC TCC GGT CGC TGG GCC GAC GCC TTC TGC GAC
N269A reverse	GTC GCA GAA GGC GTC GGC CCA GCG ACC GGA GCC
N269D forward	GGC TCC GGT CGC TGG GAC GAC GCC TTC TGC GAC
N269D reverse	GTC GCA GAA GGC GTC GTC CCA GCG ACC GGA GCC

Table 2.1 The primers of derCD23 mutants N269A and N269D synthesized by Sigma.

2.2.3 Transformation

Transformations were performed using BL21(DE3) competent cells (New England Biolabs). 50 microliters cells were thawed on ice and 1 microliter DNA added as soon as the last piece of ice in the tube disappeared. For maximum transformation efficiency, cells and DNA were incubated together on ice for 30 minutes, and then heated for 10 seconds at 42°C. Then cells were grown at 37°C with shaking for 1 hour for cell recovery and for expression of antibiotic resistance. Warm, dry plates were used for the colony formation.

2.2.4 Plasmid purification

Single colonies were picked and grown in 5 ml LB medium (Section 2.3.1) in a 50 ml flask with shaking (200 rpm) overnight at 37°C. Cell culture was spun down at 12000 rpm in a microcentrifuge and the plasmid DNA was purified using Qiagen plasmid purification Mini Kit. DNA concentration was measured with a NanoDrop ND-1000 Spectrophotometer.

2.2.5 DNA sequencing

Samples to be sequenced were sent to Source BioScience LifeSciences for analysis.

2.3 Protein expression in *E.coli*

2.3.1 LB culture medium

20 g LB powder (Invitrogen) was added in MilliQ water and the volume was adjusted to 1 liter. Then the solution was autoclaved. The medium was stored at room temperature. Concentration of Ampicillin (Sigma-Aldrich) was adjusted to 100 μg/ml before use.

2.3.2 LB agar culture plates

16 g LB agar powder (Invitrogen) was added to MilliQ water and the volume was adjusted to 1 liter. After being autoclaved, the solution was cooled to approximately 55°C before addition of ampicillin (Sigma-Aldrich) to 100 μg/ml, and poured into 90 mm diameter Petri dishes (15 ml per dish). Plates were stored in plastic bags at 4°C.

2.3.3 Long term storage of bacterial strains

For each strain to be stored at -80°C, 225 μl sterile 80% glycerol was added into the eppendorf tube and 1.0 ml of the bacterial culture (frozen stock was therefore at 15%

glycerol). Each tube was mixed well (vortexed) and placed at -80°C. The viability of the cells was checked after 1 week.

2.3.4 Protein expression of derCD23 and derCD23 mutants

1 litre culture of *E. coli* BL21 (DE3) cells harbouring the derCD23 gene was grown at 37°C in a shaking flask with LB medium. When the culture reached A600nm = 0.6-0.7, the lac promoter was induced with 1 mM Isopropyl β-D-1-thiogalactopyranoside (IPTG). After 3 hours induction, cells were harvested by centrifugation at 8000 rpm for 20 minutes in a JLA-8.1000 rotor. Cell pellets were resuspended in 30 ml 25 mM Tris pH 7.5 and stored at -20°C.

2.4 Refolding of derCD23 and derCD23 mutants

Cell pellets in resuspension buffer (25 mM Tris pH 7.5) were thawed and Triton X-100 was added to a final concentration of 1%. The mixtures were sonicated in 8 bursts of 1 minute each with breaks of 30 seconds. Samples were centrifuged at 12000 rpm and 4°C for 10 minutes in a SS34 Sorvall rotor. The pellets were resuspended in 25 mM Tris pH 7.5 and centrifuged at 12000 rpm in a SS34 Sorvall rotor and 4°C with slow shaking overnight. The pellet were resuspended in 25 mM Tris pH 7.5, 0.5 M GuHCl and centrifuged at 12000 rpm in a SS34 Sorvall rotor and 4°C for 10 minutes. Finally the pellet was resuspended in solubilisation buffer (25 mM Tris pH 7.5, 6 M GuHCl) and dissolved overnight with slow shaking.

3.5 ml of protein sample in solubilisation buffer was further diluted with solubilisaition buffer to a total volume of 15 ml, and 7.5 µl 1 M DTT was added to the protein sample. The protein sample was diluted into 150 ml refolding buffer (1 M pyridinio propanesulfonate, 10 mM Tris pH 8.0, 1 mM $CaCl_2$ with 0.98 mM oxidized glutathione, 0.65 mM reduced glutathione) as slowly as possible with rapid stirring. Then the protein sample was stored at 4°C for 2 hours. NaCl was added to a final concentration of 50 mM and the mixture was left at 4°C for 2 hours. The protein sample was dialysed into 2

litres of 20 mM Tris pH 7.5 overnight with one buffer change after 14 hours and dialysis for a further 3 hours.

2.5 Purification of derCD23 and derCD23 mutants

2.5.1 Heparin-sepharose chromatography

The HiPrep heparin column (GE Healthcare) was washed with 40 ml of 2 M NaCl, 40 ml water at a flow rate of 3 ml/min, and equilibrated with 100 ml of heparin loading buffer (25 mM Tris pH 7.5). The protein sample (derCD23) was dialyzed into heparin loading buffer. After being filtered with an 0.45 μm filter, the protein sample was loaded onto the heparin column (GE Healthcare) at 2 ml/min with a pump, connected to an AKTA-FPLC (GE Healthcare). The column was washed with 100 ml heparin loading buffer until the UV baseline was stable, and eluted with 50 ml of heparin elution buffer (25 mM Tris pH 7.5, 200 mM NaCl). Fractions containing the protein were collected into 15 ml tubes. The column was cleaned thoroughly every two weeks. The flow direction of the column was reversed and washed at a flow rate of 1 ml/min with 50 ml of 6 M Guanidine hydrochloride. Then the column was washed with 40 ml water, 40 ml of 0.1 M NaOH, 40 ml water and left in 20% ethanol.

2.5.2 Gel filtration chromatography

The HiLoad 16/60 Superdex G75 column (GE Healthcare) was equilibrated with gel filtration buffer (25 mM Tris pH 7.5) at a flow rate of 1 ml/min. Protein samples eluted from the heparin column were concentrated to 1 ml and applied onto the Superdex G75 column, which was washed with gel filtration buffer. After concentrating the fraction containing derCD23, the protein concentration was 10 mg/ml in 25 mM Tris pH 7.5. The protein solution was frozen in liquid nitrogen and stored at -80°C.

2.5.3 Buffer exchange

Buffer exchange was performed by dialysis using dialysis tubing (Fisher Scientific Ltd) with a molecular weight cut-off at 10 kDa.

2.5.4 Concentration methods

Protein samples were concentrated using Amicon® Ultra-15 centrifugal filter devices (Millipore) at 4000 rpm in a PK121R centrifuge, ALC. The devices contained cellulose membranes with a molecular weight cut-off at 10 kDa.

2.6 Protein characterization

2.6.1 Estimation of protein concentration

Protein concentration was measured with a NanoDrop ND-1000 Spectrophotometer at 280 nm wavelength. Predicted extinction coefficients for derCD23 is 2.82 mg/(ml.cm), while the molecular weight of derCD23 is 16.14 kDa.

2.6.2 SDS-PAGE

SDS-PAGE was used throughout the protein purification to assess the quantity and quality of protein (Laemmli, 1970) using a mini gel apparatus (BioRad). Gels were made according to the quantities of solutions listed in Tables 2.2 and 2.3. Samples were mixed in a ratio of 4:1 (protein: sample buffer), boiled for 10 minutes at 100°C and then spun for 10 minutes at 12000 rpm in a microcentrifuge. Protein samples were loaded along with SeeBlue® Plus2 molecular weight marker (Invitrogen). Gels were run at 160V in gel running buffer until the dye reached the bottom. Gels were stained in Coomassie staining buffer for 40 minutes and de-stained in gel de-staining buffer overnight until protein bands were visible.

	7%	10%	12%	15%
H_2O	15.3 ml	12.3 ml	10.2 ml	7.2 ml
1.5 M Tris pH 8.8	7.5 ml	7.5 ml	7.5 ml	7.5 ml
20% (w/v) SDS	0.15 ml	0.15 ml	0.15 ml	0.15 ml
Acrylamide/Bis-acrylamide (30%/0.8% w/v)	6.9 ml	9.9 ml	12.0 ml	15.0 ml
10% (w/v) ammonium persulfate (APS)	0.15 ml	0.15 ml	0.15 ml	0.15 ml
TEMED	0.02 ml	0.02 ml	0.02 ml	0.02 ml

Table 2.2 Running gel.

H_2O	3.075 ml
0.5 M Tris pH 6.8	1.25 ml
20% (w/v) SDS	0.025 ml
Acrylamide/Bis-acrylamide (30%/0.8% w/v)	0.67 ml
10% (w/v) ammonium persulfate (APS)	0.025 ml
TEMED	0.005 ml

Table 2.3 Stacking gel.

2.6.3 1D NMR spectroscopy

One dimensional NMR spectroscopy data can be acquired in a short time and give information about the folded state of the protein. Protein samples were dialyzed into 10 mM Tris pH 6.8, 125 mM NaCl, 4 mM calcium chloride and 5% D_2O. Then the samples were spun at 12000 rpm in a microcentrifuge for 15 minutes to remove precipitations. The concentrations of derCD23 and mutants were adjusted to about 1 mg/ml and the volumes were about 0.5 ml. Samples were placed in a Shigemi NMR tube (Sigma-Aldrich). The folding of derCD23 and mutants were checked at a proton frequency of 500MHz at 35°C.

2.7 Isothermal Titration Calorimetry (ITC)

Isothermal Titration Calorimetry (ITC) is a technique to measure biomolecular interactions, including protein-small molecule, protein-protein, drug target-drug, enzyme-inhibitor, antibody-antigen, protein-DNA, protein-lipid and small molecule-small molecule. ITC can accurately determine thermodynamic parameters (K_A, K_D, ΔS and ΔH) associated with binding. The principle of ITC is to use a cell feedback network to differentially measure and compensate for heat produced or absorbed between the sample and reference cell (Figure 2.1). ITC 200 apparatus (GE Healthcare) was used in the experiment. 1 litre of ITC buffer (Section 2.1.2) was treated by adding 50 g Chelex 100 (Sigma) to remove calcium. Protein samples were dialyzed against 10 mM Tris pH 6.8, 125 mM NaCl, 10 mM EDTA, then against Chelex 100 treated ITC buffer. 400 µl of 50 µM protein solutions were used for ITC experiments, and for the calcium titrations 20 mM calcium chloride in ITC buffer was used for injection at 25°C.

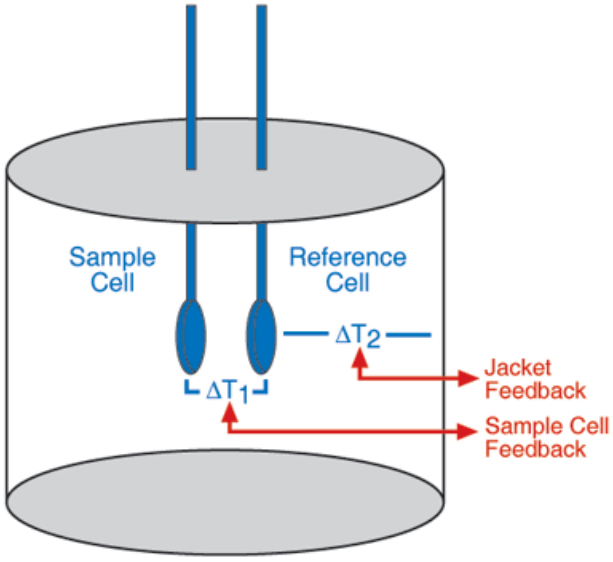

Figure 2.1 The principle of ITC.
Heat is generated or absorbed if there is a chemical reaction or interaction that occurs in the sample cell. Thermoelectric devices measure the temperature difference ($\Delta T1$) between the two cells and the temperature difference ($\Delta T2$) between the cells and the jacket respectively. The temperature difference ($\Delta T1$) is kept the same by the addition or removal of heat to the sample cell. The recorded signal shows in the form of a peak, and parameters of binding are calculated from these signals recorded as a function of the titration of reactants.

2.8 Surface Plasmon Resonance (SPR)

SPR is a technique to analyze the kinetics and thermodynamics of biomolecular interactions without the need to label reactants. Binding of molecules can be measured as a resonance signal as a function of time by detecting shifts in the angle of reflected light (Figure 2.2). Biacore™ T200 equipment (GE Healthcare) was used in the experiment.

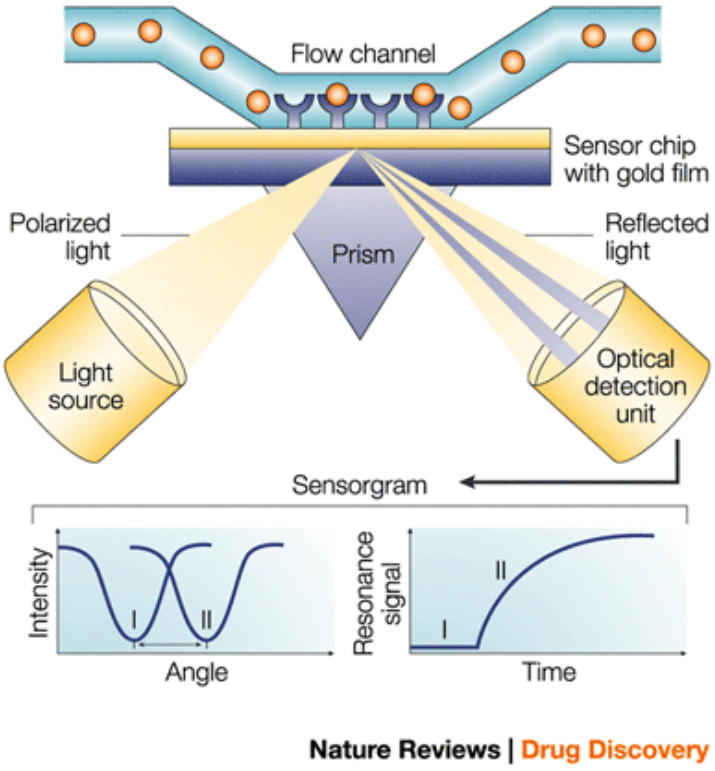

Figure 2.2 The principle of SPR.
SPR detects changes in the refractive index of the medium near the surface caused by binding of molecules (Cooper, 2002). Angle shifts of the reflected light (lower left-hand diagram) can be monitored and plotted as resonance signal versus time (lower right-hand diagram). (Figure taken from Cooper, 2002).

All experiments were performed at 25°C. A specific binding surface was prepared by coupling derCD23 to a CM5 sensor chip through the amine coupling procedure. Coupling densities of 50 resonance units were used. Protein samples in HBS (10 mM Hepes, pH 7.4, 150 mM NaCl, 4 mM $CaCl_2$, and 0.005% (vol/vol) surfactant p20) were injected over the sensor chip at 15 µl/min with a 90 s association phase followed by a 10 minutes dissociation phase. In the reverse binding experiment, a biotinylated Fcε3-4 protein was immobilized at 150 resonance units on a streptavidin chip, and soluble

derCD23 or mutants were injected over the surface. Biotinylation of Fcε3-4 was performed by mixing Fcε3-4 with Biotinamidohexanoic acid 3-sulfo-N-hydroxysuccinimide ester sodium salt (Sigma-Aldrich) at a ratio of 3:1, a process that generally ensures a single biotinylation site per protein, followed by dialysis. Injections over underivatized sensor surfaces were performed to test for non-specific binding. Curve fitting and other data analyses were performed using MicroCal Origin 6.1 (OriginLab Corporation).

2.9 Preparation of IDEC152-Fab

2.9.1 Antibody digestion

10 mg IDEC152 IgG antibody was dialyzed into sample buffer (20 mM sodium phosphate, 10 mM EDTA, pH 7.0) and concentrated to approximately 20 mg/ml (0.5 ml). The digestion buffer was prepared by adding a final concentration of 20 mM cysteine/HCl to the sample buffer and adjusting the pH to 7.0. Immobilized papain beads were mixed by inversion or gentle shaking to obtain an even suspension. Then 0.5 ml of the 50% immobilized papain slurry was added to an Eppendorf tube. To ensure proper gel slurry dispensing, a cut pipette tip was used. 1.0 ml of digestion buffer was added to the gel slurry in order to equilibrate the gel. The gel was separated from the buffer by centrifugation. This wash procedure was repeated 3 times and the gel was resuspended in 0.5 ml of digestion buffer. 0.5 ml of the prepared sample was added to 0.5 ml of digestion buffer and transferred to the eppendorf tube containing the immobilized papain.

The mixture was incubated in a circulating water bath at 37°C at high flow rate with 250 microliter samples for 30 min, 1 hour, 2 hours, 4 hours, 6 hours, 8 hours and overnight. 0.25 ml of 10 mM Tris pH 7.5 was added to end the reaction. Constant mixing of gel was maintained during the incubation.

2.9.2 Ion exchange chromatography

A TSKgel SP-5PW glass column (Tosoh Bioscience) was equilibrated with buffer A (20 mM sodium acetate pH 5.06). Protein samples digested from IDEC152 were dialysed into buffer A and then applied onto the ion exchange column, which was washed with buffer A. Then the proteins were eluted with a sodium chloride gradient elution using 10 times column volume. Peaks were collected after buffer B (20 mM sodium acetate pH 5.06, 200 mM NaCl) reached 100%.

2.10 Crystallisation and treatment of crystals

2.10.1 Principles of protein crystallisation

Like small molecules, proteins can form crystals in appropriate conditions. Proteins align themselves to form a three-dimensional lattice (Figure 2.3). The importance of crystals in structural studies of macromolecules is that they can be used to determine three-dimensional structures by X-ray diffraction.

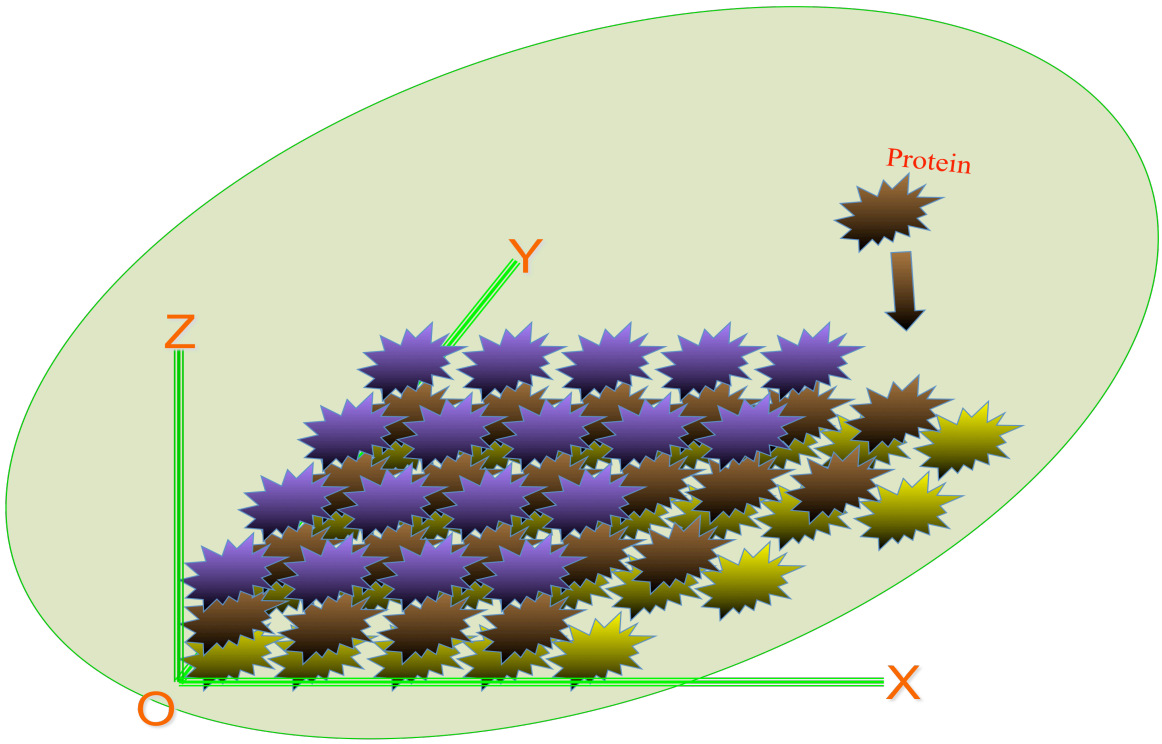

Figure 2.3 Three-dimensional lattice of protein crystal.

Crystallisation is a phase transition phenomenon, and there are two principal regions in a crystallisation phase diagram (Figure 2.4): supersaturated and undersaturated regions. The supersaturated region includes a precipitation zone, a nucleation zone (labile zone) and a metastable zone. Crystals grow in the supersaturated region, and dissolve in the undersaturated region (Asherie, 2004). There are three stages, nucleation, crystal growth and cessation, in the crystallisation of all molecules. Both nucleation and growth of crystals occur in the supersaturated region, but require different concentrations of protein. Nucleation and growth compete at higher protein concentration (labile zone), and only growth occurs in the lower concentration of the metastable zone (Weber, 1997). The strategy for crystallisation is to drive the system from the undersaturated to the saturated zone. Therefore, proteins are crystallised by changing factors that affect their solubility (Table 2.4).

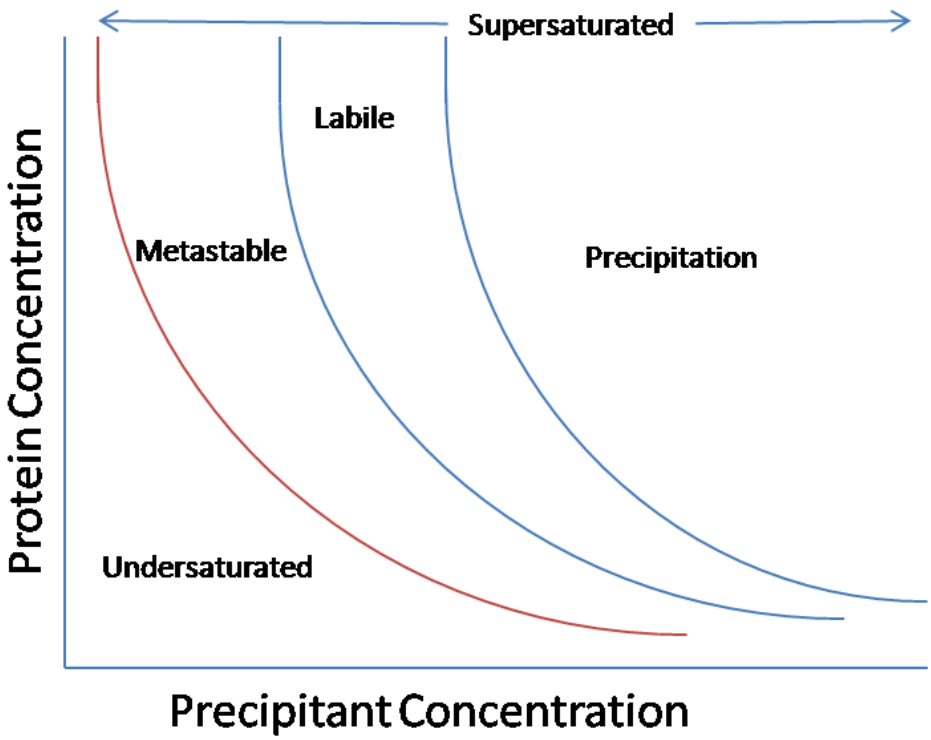

Figure 2.4 A schematic drawing of a protein crystallisation phase diagram based on protein and precipitant concentrations. (Figure is adapted from Weber, 1997).

For the macromolecule	Purity, stability, biochemical or genetic modification, etc
Chemical factors	pH, precipitant, ionic strength, specific ions, etc
Physical factors	Temperature, crystallisation method, time, etc

Table 2.4 Factors affecting crystallisation.

Many different approaches for crystallisation have been developed. Vapour diffusion is the most commonly used method for protein crystallography, altering the precipitant concentration. Mixed protein and precipitant solutions are either suspended over (hanging drop) or sitting in a well next to (sitting drop) a large reservoir of precipitant or other dehydrating agents, with which the drop of protein solution equilibrates (Figure 2.5).

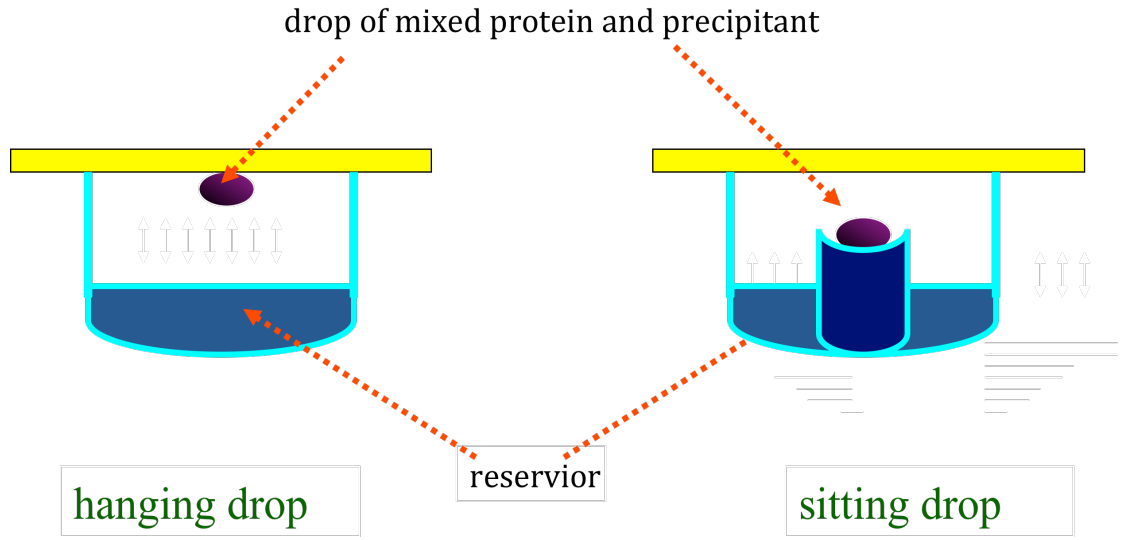

Figure 2.5 Hanging drop and sitting drop vapour diffusion methods.

However, macromolecular crystal growth is still unpredictable, and some proteins apparently cannot be crystallised. There are two steps for obtaining crystals: crystal screening and crystal optimization.

2.10.2 Crystal screening

Crystal screening uses a range of kits of prepared precipitant and additive compounds to obtain initial crystals. Concentrated protein (5-40 mg/ml) was used for setting up nanolitre crystallisation experiments using the sitting-drop vapour diffusion method. Typically, 70 μl of reservoir was transferred into subwell 1 of MRC-LMB plates from the crystallisation screening kits, and 100 nl of protein solution was mixed with 100 nl of reservoir using a Mosquito Liquid Handing robot (TTP Labtech). Then the plates were put into an 18°C incubator, and imaged every 3 days for 8 weeks using CrystalLIMS™ (TriTek), a laboratory informatics management system.

2.10.3 Optimization of crystallisation conditions

Crystals are usually not good enough to be used for X-ray data collection after crystal screening, and need to be optimized to obtain diffraction-quality crystals for structure solution. Both size and the order of a protein crystal are important. In the previous section, many factors that affect protein crystal growth were described. Crystal optimization involves systematically changing these conditions, such as chemical additives, pH, precipitant or ionic strength.

2.10.4 Seeding

Crystallisation conditions are often not optimal for both nucleation and growth of crystals. Nucleation is more likely to occur in higher levels of protein concentration, whereas growth of crystals is favored by lower protein levels (see section 2.8.1, Figure 2.4). Seeding is an important method to optimize crystallisation conditions by separating nucleation and growth of crystals (Bergfors, 2003). Macroseeding and microseeding are two methods classified by the size of the seeds. Macroseeding is a powerful technique to enlarge the size of crystal but requires much more labour for washing crystals repeatedly and carefully. Thus, microseeding is often tried first before macroseeding for crystal optimization. It can induce rapid crystal formation and improve the size of the crystal during the crystallisation process of certain proteins.

There are several methods of microseeding in terms of handling of micro-seeds. In this thesis, commercial seed beads from Hampton Research and cat whiskers were used for seeding. Normal crystallisation trials were set up and a cat-whisker was used to transfer seed crystals to new drops by streaking the whisker through the drop.

2.10.5 Soaking and co-crystallisation

After crystallisation of a protein, soaking may be used to obtain protein-ligand complexes or heavy-atom derivatives (Beck *et al*., 2009; Hassell *et al*., 2007; Kim and Haren, 1995). Co-crystallisation is an alternative method, and may also optimize crystallisation conditions and produce larger and/or more ordered crystals.

Soaking crystals is convenient and reproducible, but several factors need to be considered, such as the soaking time, ligand solubility and concentration. (Hassell *et al*., 2007). The soaking times may range from several minutes to several months for different protein-ligand complexes. A gradient soak with stepwise increase in ligand concentration or different solvent can be a valuable option. The disadvantages are that crystal packing may inhibit a ligand's access to binding sites, or the ligand may cause structural changes that destroy the crystal.

Co-crystallisation is a method to mix the ligand and the protein to form a complex that is subsequently used for crystallisation. During crystal growth, the ligand is incorporated into the crystal lattice. However, the presence of the ligand in the crystallisation drop may cause unpredicted influences on the crystallisation process.

Soaking and co-crystallisation methods were used to obtain calcium-bound derCD23 and calcium-bound derCD23/Fcε3-4 structures, respectively.

2.10.6 Cryoprotectant

X-ray data collection of cryo-cooled crystals is an essential technique for structure determination of macromolecules (Garman, 1999; Garman and Schneider, 1997; Hope,

1990). The crystals need to be in a solution that contains cryo-protectant to suppress ice formation in the ultra-low temperature. Glycerol, MPD and low molecular weight PEGs are often used as cryo-protectants. Salts, sugars, paratone, alcohols and other agents are also good cryo-protectants for some proteins (Rubinson *et al*., 2000). Although 15-25% glycerol is suitable for most crystals, it does not mean that glycerol is the best cryo-protectant. Testing with different cryo-protectants is necessary for data collection. Several methods to transfer crystals into cryo-protectant have been developed: dialysis, co-crystallisation, rapid transfer etc. (Fernandez *et al*., 2000; Sousa, 1995). Cryo-protectant was added to calcium-bound derCD23 crystals by co-crystallisation, whereas all other crystals were cryo-protected by the rapid transfer method.

2.10.7 Dehydration

One of the major differences between protein and salt crystals is the high solvent content of protein crystals. 25-85% by volume of the protein crystal consists of channels, which are mostly occupied by water molecules. These water molecules play an important role in maintaining the structure of protein molecules in the crystal (Frey, 1994). However, high solvent content may be associated with loose packing of protein molecules, and reduction of the solvent content of crystals may produce more ordered crystals, extending the resolution of crystal diffraction (Salunke *et al*., 1985). Dehydration is a post-crystallisation method to improve diffraction of protein crystals by reducing solvent content.

Several dehydration protocols have been developed (Heras and Martin, 2005). One method is to allow crystals in a capillary tube to lose water to the atmosphere or to different saturated salt solutions. Crystal dehydration can also be achieved by transferring the crystals to a dehydrating solution with a higher concentration of precipitant. A gentle dehydrating method is to change the reservoir into a more dehydrating solution. Dehydrating methods were used to attempt to improve the diffraction resolution of derCD23/Fcε3-4 crystals, although no improvement was observed.

2.10.8 Annealing

Cryo-cooled crystals are used for data collection since it reduces radiation damage and increases lifetime. Flash-cooling of crystals is essential in order to produce an amorphous form of water that avoids ice formation and damage to the crystal (Heras and Martin, 2005; Kriminski *et al*., 2002). Nevertheless, flash-cooling of crystals may cause lattice disorder, increased mosaicity and reduced diffraction resolution (Heras and Martin, 2005). Mosaicity is a measure of the long-range disorder of a crystal. Lower mosaicity indicates more ordered crystals.

Annealing is a method to reduce mosaic spread by warming the crystal to room temperature and flash-cooling it again. There are three different protocols: macromolecular crystal annealing (MCA), flash-annealing (FA) and annealing on the loop (AL) (Heras and Martin, 2005). MCA consists of moving the crystal from the cold gas stream to cryoprotectant for about 3 minutes and flash-cooling again (Harp *et al*., 1998). FA and AL are annealing methods that involve blocking the cold gas stream (Yeh and Hol, 1998). Annealing methods were used to attempt to improve the diffraction resolution of derCD23/Fcε3-4 crystals, but no improvement was observed.

2.11 Data collection and processing

2.11.1 Data collection

X-ray data collection involves many choices, which influence the quality of the final data. The X-ray source should match the properties of crystal (Nave, 1999). Bigger, single crystals with low mosaicity and high order are preferred to collect high diffraction quality data (Evans, 1999). Strategies of data collection are important to obtain data with high redundancy and completeness by choosing the optimal exposure time, resolution range, overall rotation range and angular range per frame (Dauter, 1999; Evans, 1999).

Cryo-crystallography was routinely used for data collection for all crystals studied and reported in this thesis. Crystals were mounted with a nylon loop and frozen in liquid nitrogen before taking to the Diamond Light Source (Synchrotron) for data collection (Pflugrath, 2004). A temperature of 100 K was maintained under a nitrogen stream to minimise radiation damage to the crystals (Garman, 2010).

All datasets were collected from single crystals at the Diamond Synchrotron. Initial diffraction images were inspected with MOSFLM (Battye *et al*., 2011) to determine space group and unit cell parameters by the autoindexing function. Space group and unit cell parameters were identified according to the penalty and symmetry of space group from the list provided by MOSFLM. If all observed reflections overlay with MOSFLM placing boxes for predicted spots according to the selected space group and cell dimensions, then these unit cell parameters are correct. Then the Strategy program was used to calculate the starting angle and minimum oscillation (ϕ) range for collecting a complete dataset.

2.11.2 Data processing

Initially, HKL2000 was used for data processing after data collection. The HKL2000 program package contains three parts: XdisplayF for visualization, Denzo for data reduction and integration and Scalepack for merging and scaling (Otwinowski and Minor, 1997). Some datasets were processed by a combination of MOSFLM and SCALA (Evans, 2006), if they failed with HKL2000.

Several statistical parameters were used to assess the quality of the collected data:
$I/\sigma\ (I)$, Redundancy, R_{merge} (or R_{pim}) and Completeness.

$I/\sigma(I)$: ratio between the average intensity of the reflections and their corresponding standard deviation.
Redundancy: ratio between the number of measured and independent reflections.
$R_{merge} = \Sigma_{refl}\Sigma_i|I_i - I_{aver}|/\Sigma_{refl}\Sigma_i I_i$, where I_i is the intensity of a i^{th} measurement of a reflection I_{aver} the average intensity for that reflection, calculated on all the

measurements acquired for that reflection. Σ_{refl} indicates the sum calculated over all the independent reflections measured.

$R_{pim} = \Sigma_{refl}(1/(n_{refl} -1))\Sigma_i|I_i - I_{aver}|/\Sigma_{refl}\Sigma_i I_i$, where n_{refl} is the number of observations of a reflection. R_{merge} is not a good measure of data quality, as it tends to increase with increasing redundancy. Redundancy-independent R_{pim} is better to assess data quality when redundancy is high (Evans, 2006).

Completeness: ratio between the number of crystallographic reflections measured in a dataset and the total number of reflections present at the specified resolution.

2.12 Matthews coefficient calculation

Matthews coefficient (Vm) is calculated using the formula: Vm = V/(n×M) (Matthews, 1968). Vm is usually found to have values between 1.6 and 3.5 $Å^3Da^{-1}$depending on the solvent content of the crystals. Thus, this is a way to estimate the number of molecules in the asymmetric unit.

V = volume of the unit cell

n = the number of asymmetric units in the unit cell

M = molecular weight of the contents of the asymmetric unit

Asymmetric unit: the smallest unit that can be rotated and translated by the symmetry operators of the crystallographic space group. It can contain part of a molecule or several molecules.

2.13 Structure solution, model building and refinement

2.13.1 Molecular replacement

In order to calculate the electron density map from the X-ray diffraction pattern, both the structure factor amplitudes and the phase are required. The structure factor amplitudes are obtained from the intensities of the reflections, whereas the phase information is lost during data collection. The lost phase information can be obtained by several different approaches. Molecular replacement is now the most used method according to the record in the Protein Data Bank (PDB) (Evans and McCoy, 2008).

Molecular replacement derives phase information from a known structural model, which is partially the same as the target structure. Molecular replacement is a six-dimensional movement:

$$x' = Rx + T$$

The coordinates of the structure to be solved (x') are a transformation of the input model (x). Three parameters define a rotation matrix (R), and three parameters define the translation vector (T). In this thesis, all structures were solved by molecular replacement, performed by PHASER, which is developed using maximum likelihood method (McCoy *et al*., 2007). An input model can be rotated and translated to create numerous hypotheses of orientation and position of the model in the unit cell. All hypotheses are tested by measuring the consistency of the model with the data. A high probability that the data could be observed indicates a better solution.

2.13.2 Model building and refinement

If the calculated phases are good, then a model can be built into the resulting electron density. Model building of all structures was performed by COOT (Emsley *et al*., 2010), a program that is particularly suitable for protein modeling using X-ray data. 2Fo-Fc (typically 1σ level) and Fo-Fc (typically 3σ level) electron density maps were calculated and used for manual building. Loop 4 and loop 1 of derCD23 were deleted at the beginning, and built gradually into the structure according to the positive difference map.

After manual model building, the coordinates and temperature factors were refined against the observed X-ray data in REFMAC (Murshudov *et al*., 2011) or PHENIX (Adams *et al*., 2011) to minimize the differences between the experimental structure factor amplitudes and those from the model calculation. In this thesis, rigid body refinement in REFMAC was used after molecular replacement to move the overall molecules as a unit at lower resolution (10-4 Å). Then TLS and restrained refinement

was carried out using REFMAC or PHENIX. These two programs also contain restraints to maintain correct stereochemistry, such as NCS, bond lengths and angles. The weighting between the observed X-ray data and the stereochemistry of the model was adjusted to obtain the lowest R_{work}, R_{free} and best stereochemistry. R.m.s. deviations in bond lengths and angles, R_{work} and R_{free} were used to monitor the progress of the refinement. Fitting of structure to the electron density maps and temperature factor values were also considered to assess the progress of refinement.

For the refinement of low resolution structure, local NCS restraints, "jelly-body" restraints and map sharpening were used in REFMAC (Murshudov *et al*., 2011).

Definitions:

2Fo-Fc map: represents the density corresponding to the structure.

Fo-Fc map: represents differences between the real structure and the current model.

Temperature factor (B-factor): also known as atomic displacement parameter (ADP), a measure of how much an atom vibrates around its mean position.

TLS refinement: a method to include anisotropic displacement refinement of a set of selected atoms as a rigid body requiring only 20 parameters at medium to low resolution. TLS represents translation (6 parameters), libration (6 parameters) and screw-motion (8 parameters).

NCS restraints: Non-crystallographic symmetry (NCS) restraints can be used when there are two or more copies of a protein molecular in the asymmetric unit. Atoms are restrained to their NCS related equivalents during refinement.

Local NCS used in REFMAC: if interatomic distances less than a set number in atom pairs, and the distances are similar in NCS related equivalents, then these atom pairs are included in NCS restraints (Murshudov *et al*., 2011).

"Jelly-body": a method to control interatomic distances for pairs of atoms from the same chain during refinement.

Map sharpening: a method attempt to increase signal while reducing amplification of noise.

$R_{work} = \Sigma||F_{obs}| - |F_{calc}||/\Sigma|F_{obs}|$, where F_{obs} and F_{calc} are the observed and calculated structure factor amplitudes.

R_{free} = $\Sigma_t||F_{obs}|$ - $|F_{calc}||/\Sigma_t|F_{obs}|$, where F_{obs} and F_{calc} are the observed and calculated structure factor amplitudes, and $_t$ is the test set of data omitted from refinement (5% in this case).

R.m.s. deviations (root-mean-square deviations) in bond lengths and angles: a measure of how well the structure model conforms to the ideal values of bond lengths and bond angles in crystallography.

2.14 Structure validation

The final model was analyzed with the software Molprobity to check its quality, such as protein geometry and all-atom contacts (Chen *et al*., 2010). The bond torsion angles of the polypeptide backbone of proteins adopt preferred combinations (Ramakrishnan and Ramachandran, 1965). Molprobity analyses the model by comparing the model with these preferred conformations. A Ramachandran plot can be obtained to show the deviations (Ramachandran *et al*., 1963).

2.15 Figure preparation

Images of all structures and electron density maps were produced using PyMOL (http://www.pymol.org).

2.16 Structural analysis

The interaction between derCD23 and Fcε3-4, and the buried surface area are calculated using PDBePISA, which is a structural analysis tool of European Bioinformatics Institute (EBI).

Chapter 3:
The crystal structure of Ca^{2+}-bound derCD23

3.1 Introduction

C-type lectins are a large group of Ca^{2+}-dependent (C-type) carbohydrate-binding (lectin) proteins. However, some proteins in the C-type lectin-like domain (CTLD) superfamily fold like a lectin, but require neither calcium nor carbohydrate for their function (Drickamer, 1999; Zelensky and Gready, 2005). A large number of structures of CTLDs in the Protein Data Bank (PDB) provide a detailed understanding of the topology and Ca^{2+}-binding sites of this family of proteins. Four Ca^{2+}-binding sites have been identified in CTLDs depending on the CTLD sequences and the crystallisation conditions (Figure 3.1) (Zelensky and Gready, 2005). In the rat mannose binding protein-A, Ca^{2+}-binding site 3 is considered as a crystallographic artefact according to biochemical data (Loeb and Drickamer, 1988; Weis *et al*., 1992). In most CTLDs, Ca^{2+}-binding site 2 is involved in carbohydrate binding.

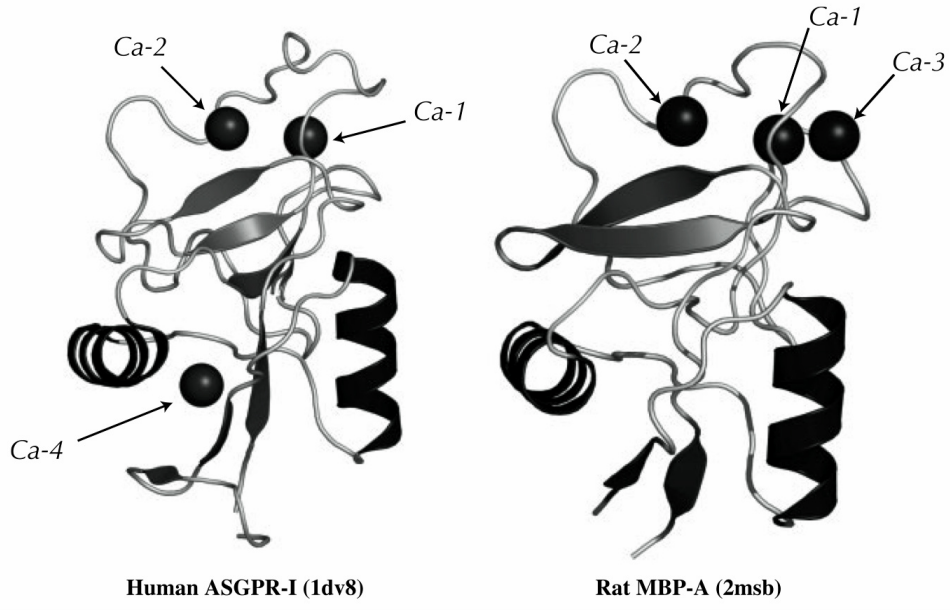

Figure 3.1 Ca^{2+}-binding sites in CTLDs.
Shown are ribbon diagrams of two representative CTLD structures, human asialoglycoprotin receptor-I (ASGPR-I) and rat mannose binding protein-A (MBP-A), demonstrating the four typical locations of calcium ions in the CTLDs (Figure taken from Zelensky *et al*., 2005).

According to the sequence alignment of Ca^{2+} site ligands in various species of CD23 and other C-type lectins, there are two putative Ca^{2+}-binding sites in human CD23 (Figure 3.2). E257 belongs to both calcium binding "site 1" and "site 2". "Site 1" is not well conserved, as N225 and K229 are not classical Ca^{2+}-binding residues. The NMR structure of derCD23 was determined, and NMR titration experiments indicated Ca^{2+} binding to "site 1" (Hibbert *et al*., 2005). Then the crystal structure of the CTLD of CD23 double mutant (H213R and G256S) was reported and Ca^{2+} was observed in "site 2" (Figure 3.3A) (Wurzburg *et al*., 2006). This CD23 construct contained two mutations that were not apparently included for any functional reason. No explanation was provided in the paper. The two methods therefore gave conflicting results concerning the location of Ca^{2+} (Figure 3.4). In addition, loop 4 (residues 253-257) is disordered in the Ca^{2+}-bound structure of CD23 double mutant (Figure 3.3B). This is inconsistent with the suggested role of Ca^{2+} in stabilizing the carbohydrate binding conformation of the loop in MBP (Ng *et al*., 1998; Sun, 2006).

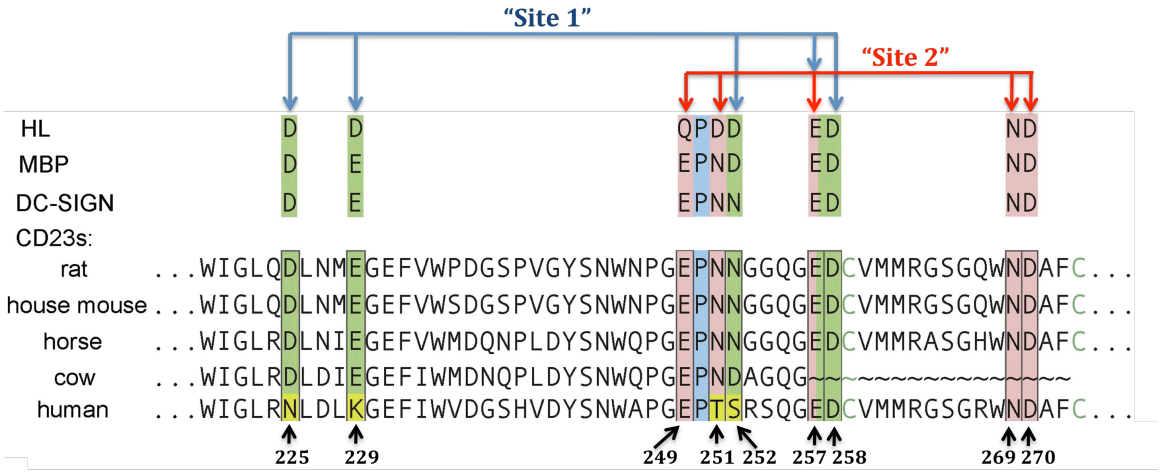

Figure 3.2 Calcium site ligands of CD23 in various species.
An alignment of CD23 sequences from rat, house mouse, horse, cow (partial), and human sources showing the calcium-ligating residues. For comparison, the corresponding residues from the human asialoglycoprotein receptor (HL), rat MBP-A, and human DC-SIGN are shown above the CD23 sequences. Ca^{2+} "site 1" ligands are highlighted in green, the conserved proline is highlighted in blue, Ca^{2+} "site 2" ligands are highlighted in pink. Non-conservative substitutions in the human sequence are highlighted in yellow. The E257 acts as both a "site 1" (side chain O3) and "site 2" (main chain O) ligand. The human CD23 numbering is given below the sequences (Figure adapted from Wurzburg *et al*., 2006).

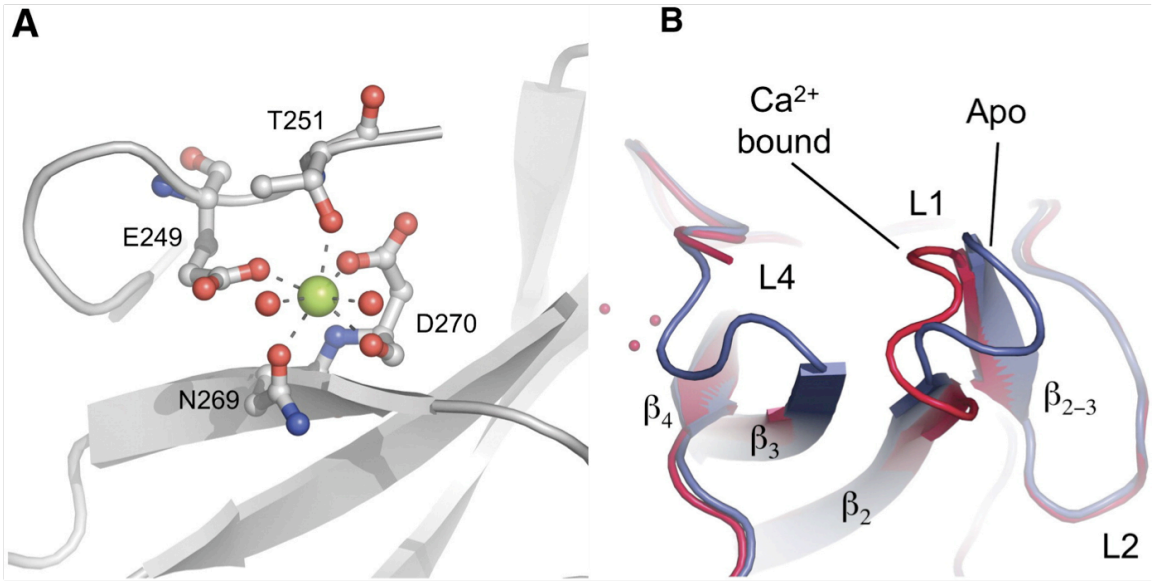

Figure 3.3 Structure of the calcium-bound CD23 double mutant.
A: The calcium binding site. The calcium is shown as a green sphere, and its ligands come from four residues E249, T251, N269, D270 and two waters. B: Superimposition of calcium-bound and calcium-free CD23 double mutant structures (PDB code 2H2T and 2H2R). The calcium-bound form is shown in red, and the calcium-free form is shown in blue. Loop 4 is disordered in the calcium-bound form (Figure taken from Wurzburg *et al*., 2006).

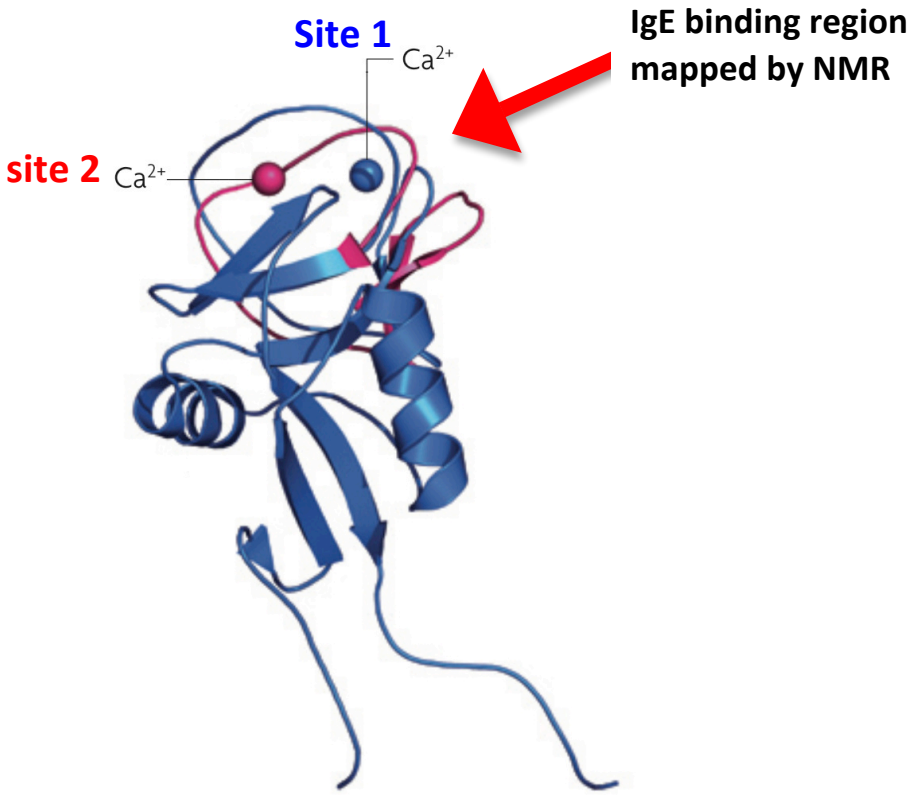

Figure 3.4 Structures of CD23 head domain.
NMR structure (PDB code 1T8D) and the Ca^{2+} ion ("site 1") observed in the NMR titration experiment are indicated in blue (Hibbert *et al*., 2005). Crystal structure of CD23 double mutant (PDB code 2H2T) and the Ca^{2+} ion ("site 2") observed are indicated in red (Wurzburg *et al*., 2006). The IgE binding site mapped by NMR (Hibbert *et al*., 2005) is close to the calcium binding sites on CD23. (Figure adapted from Gould and Sutton, 2008)

Thus, the crystal structure of Ca^{2+}-bound derCD23 was determined in order to resolve previous controversy concerning the calcium binding site(s). Comparison of derCD23 structures will provide details of Ca^{2+}-dependent structural changes in human CD23.

3.2 Cloning, refolding, expression and purification of derCD23 and derCD23 mutants

3.2.1 Cloning and expression of derCD23

The *E.coli* strain BL21(DE3) containing pET5a-derCD23 vector was obtained from Prof. James McDonnell. The pET5a vectors containing derCD23 mutants (E249A, S252A, D258A, D270A) were provided by Dr. Balvinder Dhaliwal. Site directed

mutagenesis of derCD23 to produce the mutants N269A and N269D was carried out using QuickChange kit (Stratagene, CA, USA) (Section 2.2.2).

DerCD23 and derCD23 mutants were expressed as insoluble inclusion bodies (Figure 3.5). If the concentration of cell culture was too high (OD_{600}>0.8) or the induction time was too long (more than 8 hours), yields of proteins were found to be reduced.

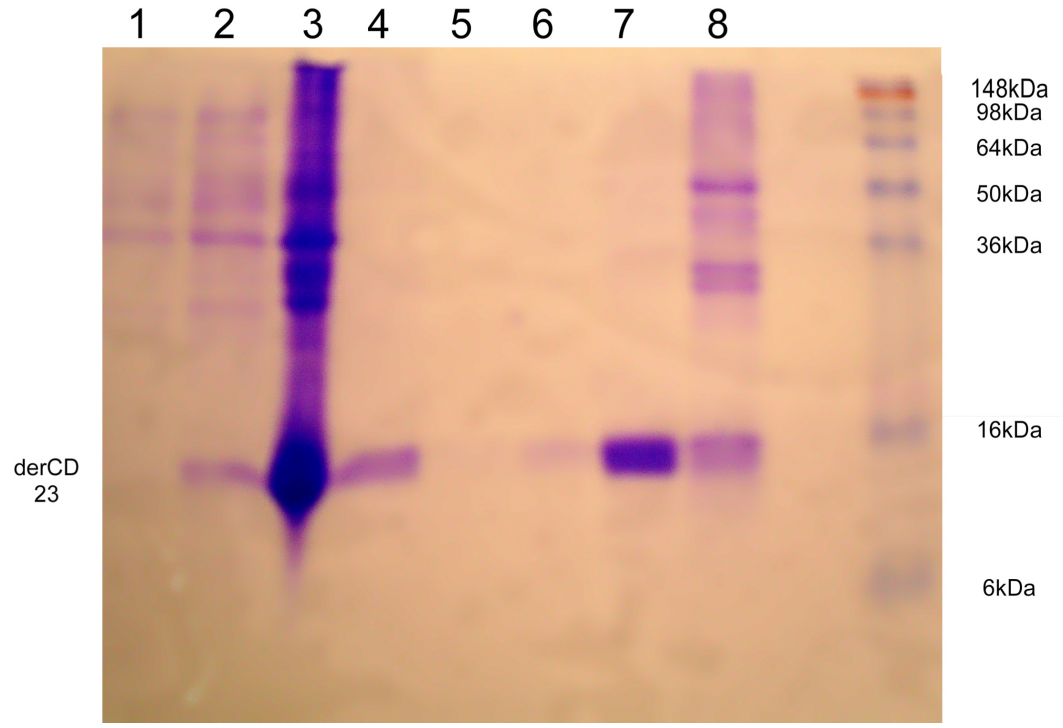

Figure 3.5 15% reducing SDS-PAGE of derCD23.
Lane 1: before induction; Lane 2: after induction; Lane 3: inclusion body; Lane 4: fractions of the peak in heparin column profile (Figure 3.6); Lane 5: heparin column flowthrough; Lane 6-7: fractions of first and second peak in gel filtration profile (Figure 3.7); Lane 8: precipitation in refolding.

3.2.2 Refolding

The protocol from Professor McDonnell's lab was previously optimized (Hibbert *et al*., 2005). However, small changes were made in order to make well-refolded proteins every time (Section 2.4). Washing of inclusion bodies with 20 mM Tris pH 7.5 was prolonged to 16 hours, and protein samples were diluted into refolding buffer as slowly

as possible, normally 4 hours for 150 ml protein samples. Protein samples may form heavy precipitation if they are diluted quickly for refolding.

3.2.3 Purification

The heparin column and size-exclusion column were mainly used to separate folded and unfolded proteins. The purification profile of derCD23 by heparin column showed a large peak, which indicates that there are derCD23 proteins binding to the column (Figure 3.6). Then, fractions of the peak were collected and loaded onto the size-exclusion column. At the beginning, NMR buffer (10 mM Tris pH 6.8, 125 mM NaCl, 4 mM calcium chloride) was used for running the size-exclusion column, but there was a lot of precipitation and this caused the column to become jammed. Then 20 mM Tris pH 7.5 was used for the gel filtration buffer. This modification produced two peaks (Figure 3.7). The first peak contained aggregated protein, and the second peak contained well-folded monomeric protein. 10 mg protein was typically obtained from 1 litre of cell culture.

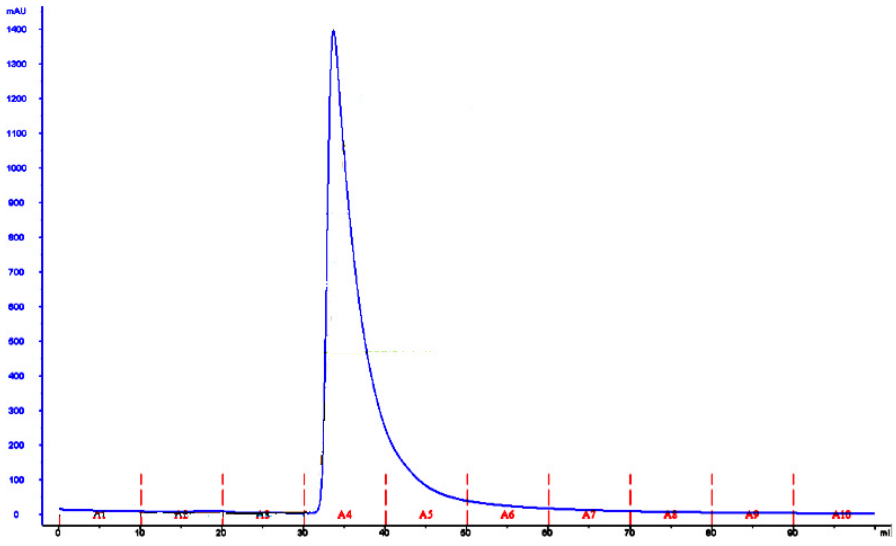

Figure 3.6 Purification profile of derCD23 by heparin column.
Blue curve: UV profile.

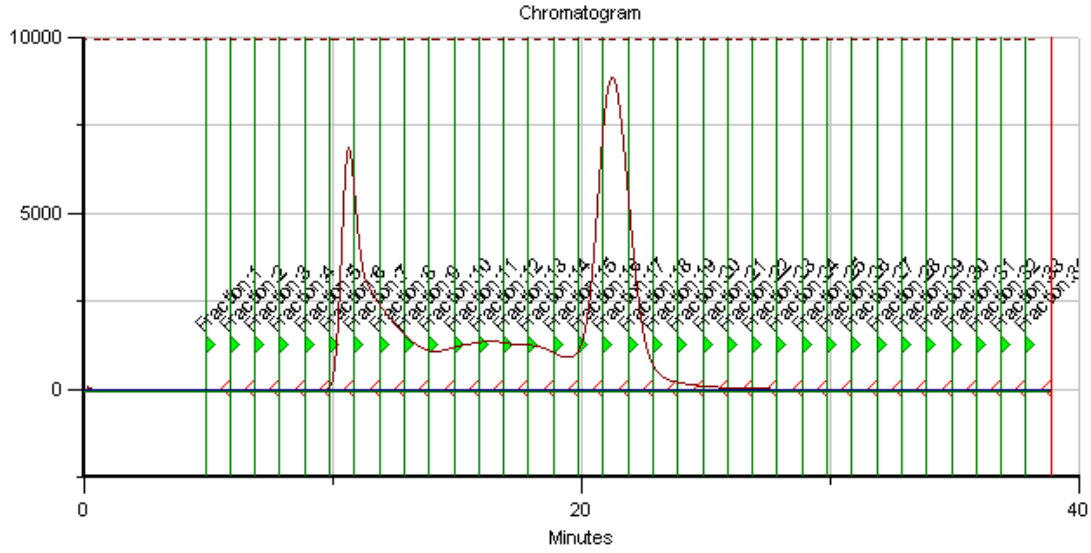

Figure 3.7 Purification profile of derCD23 on a Superdex 200 column.
The first peak contains unfolded, aggregated protein, and the second peak consists of well-folded monomeric protein.

3.2.4 1D NMR spectroscopy

After purification using the size-exclusion column, the second peak was collected and used for 1D-^{1}H NMR. Protein samples were dialyzed into 10 mM Tris pH 6.8, 125 mM NaCl, 4 mM calcium chloride and 5% D_2O. The concentration of derCD23 and mutants were adjusted to about 1mg/ml and the volume was about 0.5 ml. The large dispersion and strong signals of methyl groups between 1.0 and -1.0 ppm indicated that derCD23 and all four of the derCD23 mutants (E249A, D270A, S252A and D258A (not shown)) were well-folded (Figure 3.8).

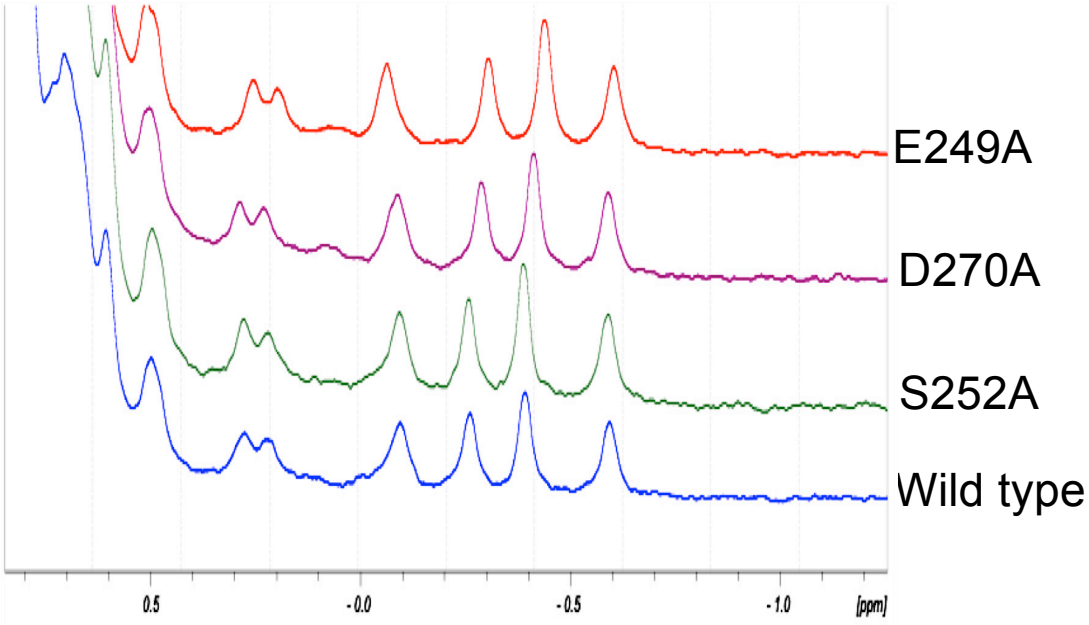

Figure 3.8 1D-^{1}H NMR spectra of derCD23 and derCD23 mutants.
The large dispersion and strong signals of methyl groups between 1.0 and -1.0 ppm indicated that the proteins were well-refolded. The 1D-^{1}H NMR spectrum of mutant D258A looked identical to those shown here.

3.3 Crystallisation of wild-type Ca^{2+}-bound derCD23

3.3.1 Crystallisation of wild-type derCD23

There were two crystallisation conditions previously identified for CD23 head domain. The experimental conditions used by Dr. Stella Fabiane (unpublished data) were as follows: protein (3.5 mg/ml in 25 mM Tris pH 7.5, 137 mM NaCl, 2 mM $CaCl_2$) was mixed 1:1 with precipitant (18.5% PEG 5000 MME or other PEG, 2% 1,6-hexanediol, 0.05 M ammonium sulphate, 0.1 M sodium acetate pH 4.7). The experimental conditions given in Wurzburg *et al* (2006) were: protein (10 mg/ml in 30 mM Tris pH 8.0, 10 mM $CaCl_2$) was mixed 1:1 with precipitant (17% w/v polyethylene glycol 4000, 100 mM MES buffer pH 6.0). Crystals of wild-type derCD23 were only obtained in the optimised first condition (18.5% PEG 6000, 2% 1,6-hexanediol, 0.05 M ammonium sulphate, 0.1 M sodium acetate pH 4.7) and used for calcium soaking (Figure 3.9).

3.3.2 Calcium soaking into wild-type derCD23 crystals

In initial experiments, the derCD23 crystals were soaked with 10 mM $CaCl_2$. However, no calcium was found to be bound to derCD23 after determining the structure (data not shown). Consideration of the crystallisation conditions suggests two possible reasons why there was no calcium binding. The first possible reason is the low pH value (4.7) of the crystallisation conditions that may prevent certain residues of derCD23 binding to calcium, such as E249 and D270. The second possible reason is that ammonium sulphate and $CaCl_2$ can form poorly soluble calcium sulphate, which leads to precipitation in the crystallisation condition and loss of calcium. Thus, crystals of wild-type derCD23 were soaked after increasing the pH to 7.1, removing the ammonium sulphate, adding 10 mM $CaCl_2$ and increasing the concentration of precipitant in the original crystallisation condition (25% PEG 6000, 2% 1,6-hexanediol, 0.1M MES pH 7.1, 10 mM $CaCl_2$, 15% glycerol).

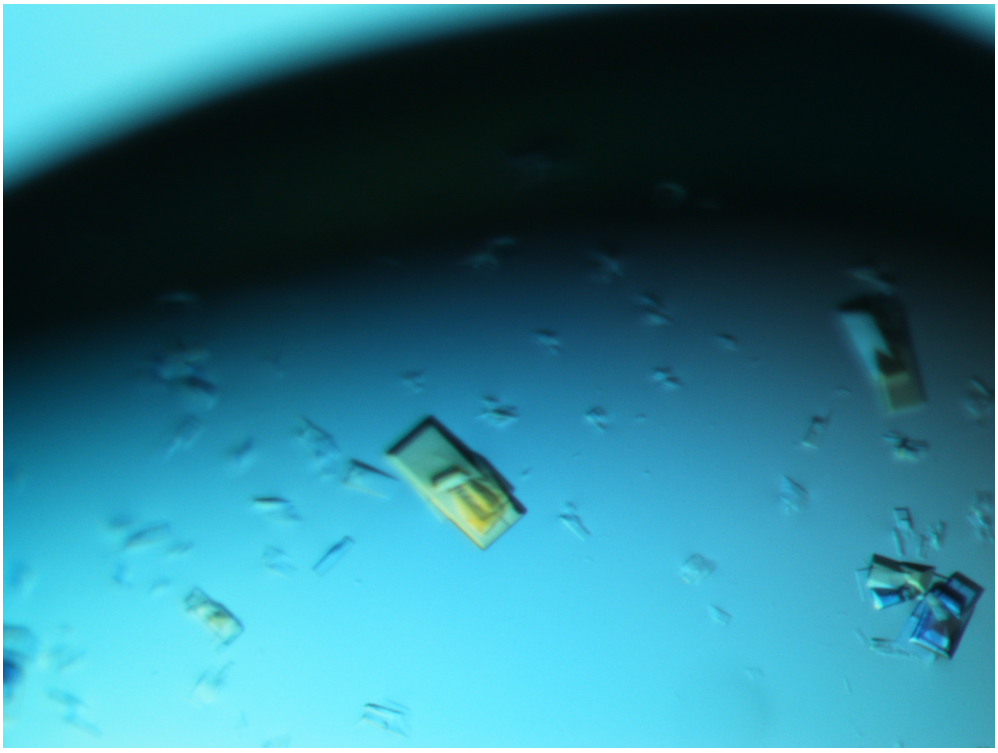

Figure 3.9 Crystals of wild-type derCD23.
Crystals grown in 18.5% PEG 6000, 2% 1,6-hexanediol, 0.05 M ammonium sulphate, 0.1 M sodium acetate pH 4.7. The longest dimension of the biggest crystal is 100 µm.

3.4 Data collection and processing

3.4.1 Data collection and processing

All datasets were collected from single wild-type derCD23 crystals, separated from clusters of crystals, at the Diamond Synchrotron using a q315 CCD detector and radiation of wavelength λ= 0.9763 Å. The dataset of calcium-bound derCD23 giving the highest resolution diffraction was used, and a summary of collection and processing of the derCD23 data is shown in Table 3.1.

Space group	*P*1
Unit-cell parameters (Å, degrees)	a = 54.24 α = 112.92 b = 53.71 β = 88.53 c = 56.64 γ = 114.96
Wavelength (Å)	0.9763
Resolution range (highest shell) (Å)	50.0-2.00 (2.07-2.00)
Number of unique reflections	34591
Redundancy	4.0
Completeness (%)	97.9 (96.9)
$I/\sigma\ (I)$	20.5 (4.6)
R_{merge} (%)	9.6 (40.6)

Table 3.1 Data collection and refinement statistics of wild-type derCD23 (Ca^{2+}soak). Values in parentheses are for the highest resolution shell.
$R_{merge} = \Sigma_{refl}\Sigma_i|I_i - I_{aver}|/\Sigma_{refl}\Sigma_i I_i$, where I_i is the intensity of a i^{th} measurement of a reflection I_{aver} the average intensity for that reflection, calculated on all the measurements acquired for that reflection. Σ_{refl} indicates the sum calculated over all the independent reflections measured.

3.4.2 Determination of space group and number of molecules in the asymmetric unit

The space group (*P*1) is the same, but cell parameters (a = 54.24 Å, b = 53.71 Å, c = 56.64 Å, α = 112.92°, β = 88.53°, γ = 114.96°) are different from the previously solved

calcium-free derCD23 structure (Dr. Stella Fabiane, unpublished data). The Matthews coefficient calculation indicated the presence of four derCD23 molecules per asymmetric unit (Matthews coefficient 2.11 $Å^3Da^{-1}$, 41.6% solvent).

3.5 Structure solution and refinement

3.5.1 Molecular replacement solution

The structure of calcium-bound derCD23 was solved by molecular replacement using PHASER with the structure of human CD23 double mutant (PDB code 2H2R, Wurzburg *et al*, 2006) as the search model. As described above, this CD23 construct contained two mutations that were not apparently included for any functional reason. In order not to bias the electron density map calculations, water molecules were removed from the search model.

3.5.2 Model building and refinement

Manual model building was carried out with COOT, coupled with refinement using REFMAC5 and PHENIX. The progression of the refinement was monitored using R factors (R_{work} and R_{free}), and TLS refinement (Painter and Merritt, 2006) was implemented by finding TLS groups (four groups for chains B and C, twelve groups for chains A and D) in PHENIX. NCS restraints were used to all chains (residues 160-224, 232-252, 258-288), and individual B-factor refinement was applied. Protein atoms of the backbone were modeled first. Disulphide bonds C163-C174 in all four chains, and C259-C273 in chains A and B were partially broken. The explanation for this may be radiation damage during data collection. They were refined for both intact and broken conformations with 0.5 occupancy for each. Water and glycerol molecules were modeled according to electron density at a later stage using the R_{free} as a guide. The length of potential hydrogen bonds and the B-factor were considered when water and glycerol molecules were checked. 404 water molecules and 3 glycerol molecules were accepted.

In the final stage, four calcium atoms were modeled, one into each molecule in the asymmetric unit. Because water and calcium have similar electron density, both were tested in refinement. A comparison of their Fo-Fc maps and B-factor was used to determine whether calcium should be built into the structure. When a calcium ion was built into each chain, the 2Fo-Fc map fitted well with calcium, and there was no obvious difference density around it. B-factor for the four calcium ions in chains A, B, C and D are 32, 22, 35 and 53 respectively. When water was built into the density for calcium, it showed an unusually low B-factor and was surrounded with positive Fo-Fc density (Figure 3.10). It was concluded that calcium was present in each of the four molecules.

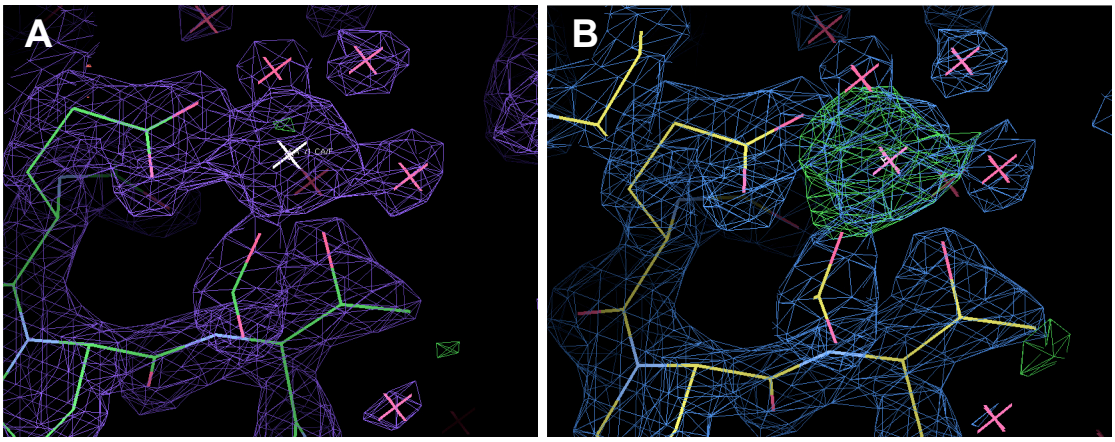

Figure 3.10 Electron density maps in the region of the calcium binding site in Chain B.
A: Calcium was modeled into calcium "site 2", and the B-factor for this calcium is 22. 2Fo-Fc map (purple) fitted well with calcium while no obvious difference density surround it. The green map is positive difference density, and there is no visible red negative difference density. B: Water was modeled into calcium "site 2", and the B-factor for this water is zero. The water is surrounded by positive difference density (green).
2Fo-Fc (1σ level) electron density maps are shown in purple or blue, and Fo-Fc (3σ level) electron density maps are shown in red (negative but not visible) and green (positive). The location of calcium and water are shown as white and pink crosses respectively, and the strong Fo-Fc positive density in B surrounding the placed water molecule is clearly seen.

The derCD23 (residues 156-298) head domain was well modeled, while N- and C-terminal regions were missing in the structure. The structure contains residues 159-290 for chain A, 157-291 for chain B, 160-289 for chain C and 160-288 for chain D. The calcium binding ligands (residues E249, T251, D270 and three waters) are clearly

observed in three chains (A, B and C), but electron density for the three waters and T251 is poor in chain D. The final refinement statistics are presented in Table 3.2.

Number of:	
Protein atoms	4271
Water molecules	404
Calcium ions	4
Glycerol molecules	3
Average B factors (Å^2):	
Protein	25.7
Water molecules	35.0
Calcium ions	35.8
Glycerol molecules	46.0
Protein (chain A)	25.9
Protein (chain B)	23.7
Protein (chain C)	26.1
Protein (chain D)	27.2
R_{work}/R_{free}(%)	15.2/20.5
r.m.s. deviations	bond lengths = 0.006 Å bond angles = 0.963°

Table 3.2 Statistics of the refinement process for the calcium-bound derCD23 structure.
$R_{work} = \Sigma||F_{obs}| - |F_{calc}||/\Sigma|F_{obs}|$, where F_{obs} and F_{calc} are the observed and calculated structure factor amplitudes.
$R_{free} = \Sigma_t||F_{obs}| - |F_{calc}||/\Sigma_t|F_{obs}|$, where F_{obs} and F_{calc} are the observed and calculated structure factor amplitudes, and $_t$ is the test set of data omitted from refinement (5% in this case).

3.5.3 Validation

The refined structure was analysed with Molprobity as indicated in section 2.9.5. An analysis of the corresponding Ramachandran plot (Figure 3.11) showed that all the residues are in allowed regions.

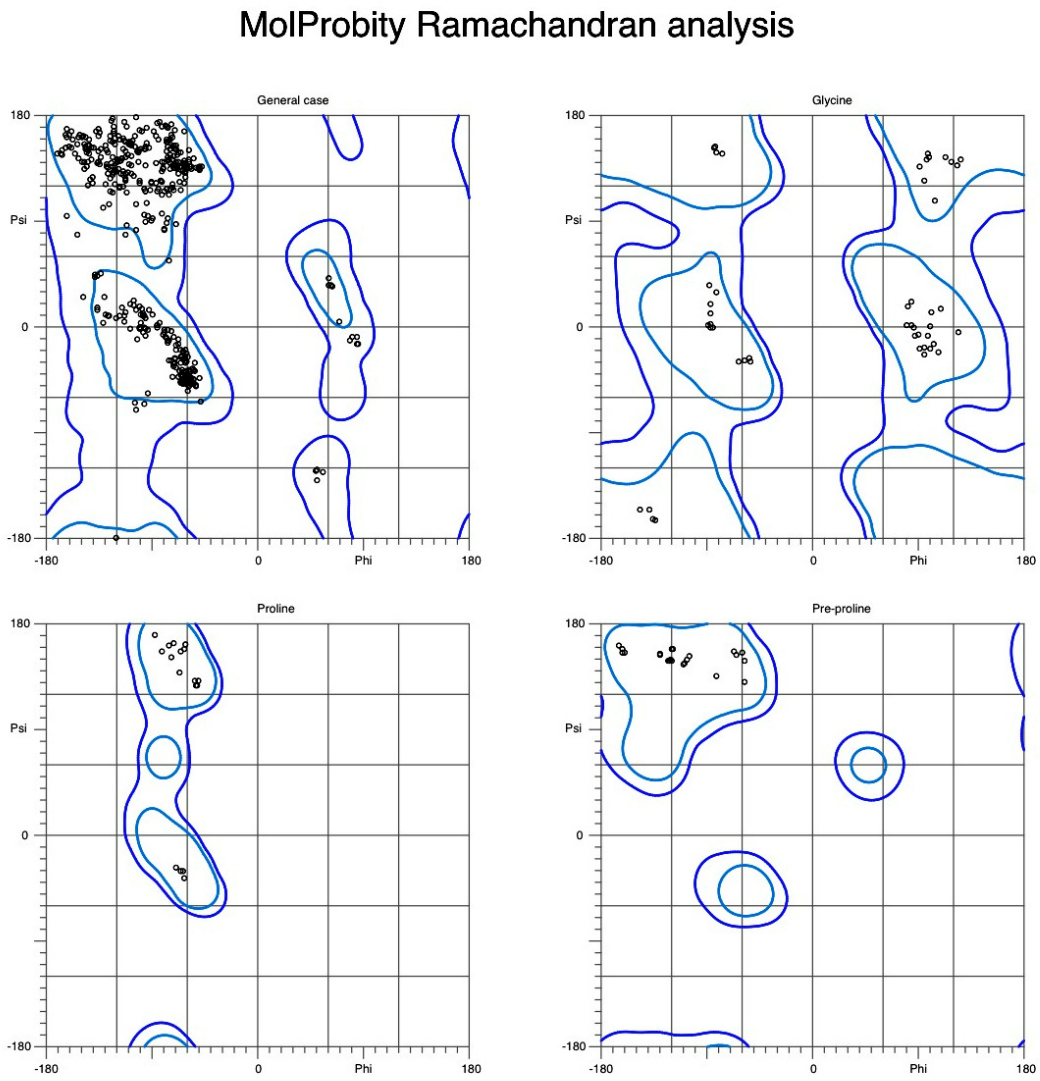

Figure 3.11 Ramachandran plots for the calcium-bound derCD23 structure, calculated with the Molprobity server.
From the top left: plot of φ and ψ angles for the general case, glycine, proline and pre-proline residues. All the residues, indicated by small black circles, were in allowed (dark blue) regions. 96.2% of residues were in the favoured (light blue) regions.

3.6 Overall structure of CD23

There are four molecules in the asymmetric unit of this derCD23 crystal form. Superimposition of all 4 copies reveals similar arrangement of the head domain and only slight variations in loop 1, but more differences in loop 4. Calcium is bound to each of the derCD23 molecules (Figure 3.12). The 2.0 Å Ca^{2+}-bound derCD23 structure has the topology of a C-type lectin domain. The structure consists of two α helices and

two β sheets formed by eight β strands. Four disulphide bonds (C160-C288, C163-C174, C191-C282 and C259-C273) contribute to the tertiary structure. The partial cleavage of some disulphide bonds is probably the result of radiation damage during data collection (Section 3.5.2). Unlike previously solved CD23 crystal structures (PDB code 2H2R and 2H2T, Wurzburg *et al*, 2006), electron density of all the head domain is well observed, including loop 1 (226-231) and loop 4 (253-257) that contribute to IgE binding.

Figure 3.12 Cartoon representation of the derCD23 structure showing all four molecules. Loop 1 and loop 4 are shown as red and magenta respectively. Four disulphide bonds (C160-C288, C163-C174, C191-C282 and C259-C273), indicated in yellow, contribute to the tertiary structure. The four calcium ions are shown as grey spheres.

3.7 Calcium binding site in derCD23

In the asymmetric unit, there are four derCD23 molecules with one calcium bound to each of them. Unlike MBP and DC-SIGN, human CD23 contains only calcium bound at "site 2". Electron density for the calcium binding ligands (residues E249, T251, D270 and three waters) and the Ca^{2+} ion is clearly observed in three derCD23 molecules (Section 3.5.2). The electron density of the fourth calcium in chain D is poor. This is not apparently the result of crystal packing differences.

The coordination of calcium is different from that seen in the previously solved structure of the CD23 double mutant (Figure 3.3A, Wurzburg *et al*, 2006). This difference with the derCD23 double mutant structure will be described later (Section 3.9). There are only 3 residues (E249, T251 and D270) providing 4 oxygen atoms and 3 water molecules providing 3 oxygen atoms involved in the binding to Ca^{2+} in 3 of 4 molecules in the asymmetric unit (Figure 3.13). The distances between calcium and the ligands in these three chains (A, B and C) are shown in table 3.3. The geometry of the calcium coordination in site 2 is pentagonal bipyramidal formed by these seven ligands. This is different from the pentagonal bipyramidal with one bisected apex, formed by eight ligands, in site 2 of MBP, DC-SIGN and human asialoglycoprotin receptor-I (ASGPR-I) (Meier *et al*., 2000; Snyder *et al*., 2005; Weis *et al*., 1992; Wurzburg *et al*., 2006). The bisected apex consists of two water molecules in these three carbohydrate-free C-type lectins, while two carbohydrate oxygen atoms occupied this bisected apex in these carbohydrate-bound lectins. In the fourth derCD23 molecule (chain D), site ligand T251 is far from Ca^{2+}, and electron density for the water molecules is not clear.

According to the alignment of CD23 sequences from various species (Figure 3.2), N269 is expected to be a calcium ligand as it binds calcium in MBP, DC-SIGN and human asialoglycoprotin receptor-I structures, and is seen as such in the CD23 double mutant structure (Wurzburg *et al*., 2006). Surprisingly, N269 is not involved in the binding to Ca^{2+} in this derCD23 structure. In addition, E257, a residue expected to belong to both "site 1" and "site 2" on the basis of function as a calcium ligand in other CTLDs, is not a calcium ligand.

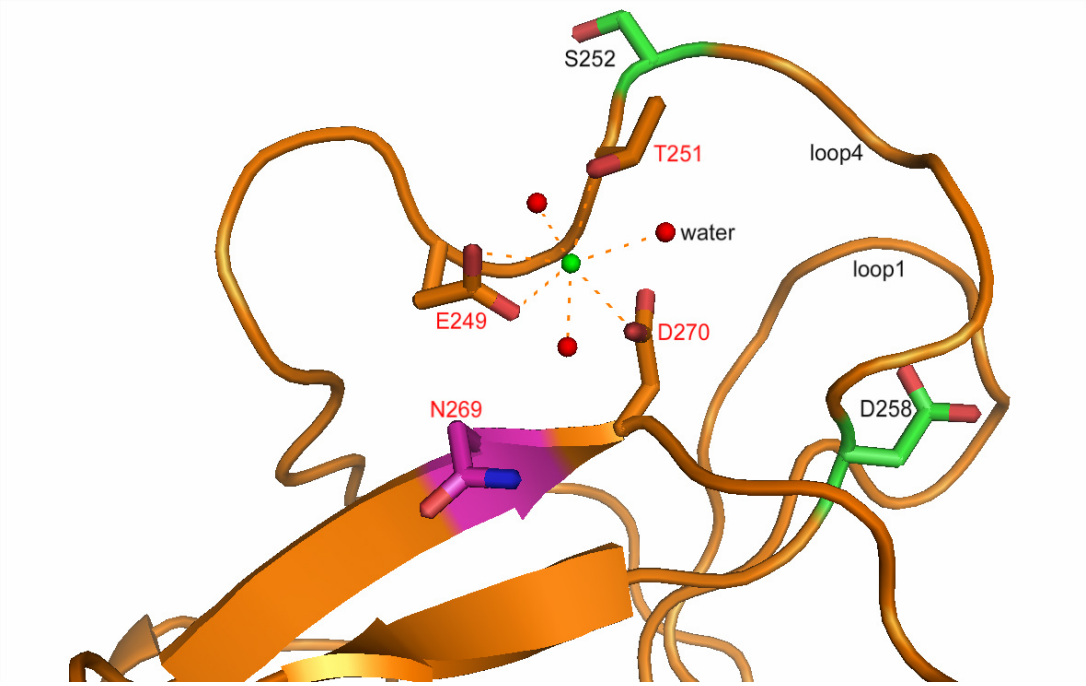

Figure 3.13 Calcium binding to derCD23 as seen in 3 of 4 molecules in the asymmetric unit (chains A, B and C).
Calcium binds to "site 2", with 3 residues (E249, T251 and D270) providing 4 oxygen atoms and 3 water molecules providing 3 oxygen atoms involved in the binding of Ca^{2+}. N269 is not involved. Potential "site 1" residues (S252 and D258) are distant from each other.

	Chain A	Chain B	Chain C
E249 OE1	2.68	2.65	2.75
E249 OE2	2.54	2.58	2.66
T251 OG1	2.62	2.44	2.71
D270 OD1	2.61	2.44	2.59
Water 1	2.59	2.56	2.93
Water 2	2.70	2.62	2.66
Water 3	2.42	2.43	2.89

Table 3.3 Comparison of the distances (Å) of calcium with ligands in chains A, B, C and water molecules.

3.8 Comparison with Ca^{2+}-free derCD23 structure

3.8.1 Difference between Ca^{2+}-bound and Ca^{2+}-free derCD23 structures

Comparison of the calcium-bound derCD23 structure with the Ca^{2+}-free derCD23 structure solved by Dr. Stella Fabiane (unpublished, Table 3.4) reveals residues undergoing a conformational change upon calcium binding (Figure 3.14). Overall, the structures of derCD23 with and without calcium show little differences in secondary structure or packing of the core. However, there are large changes in loop 4 and small variations in loop 1. The four copies of loop 4 in the Ca^{2+}-bound derCD23 structures adopt similar conformations. The four copies of loop 4 in Ca^{2+}-free derCD23 have two different conformations, neither of which is the same as the Ca^{2+}-bound conformation. This indicates that calcium functions to stabilize loop 4.

Space group	*P*1
Unit-cell parameters (Å, degrees)	a = 52.40 α = 68.49 b = 56.73 β = 88.16 c = 62.10 γ = 73.40
Resolution range (highest shell) (Å)	57.2-2.25 (2.37-2.25)
R_{work}/R_{free}(%)	17.3/23.6
R.m.s. deviations	bond lengths = 0.017 Å bond angles = 1.944°
Protein (chain A)	residues 157-291
Protein (chain B)	residues 157-291
Protein (chain C)	residues 159-290
Protein (chain D)	residues 159-289

Table 3.4 Summary of Ca^{2+}-free derCD23 structure solved by Dr. Stella Fabiane (unpublished).

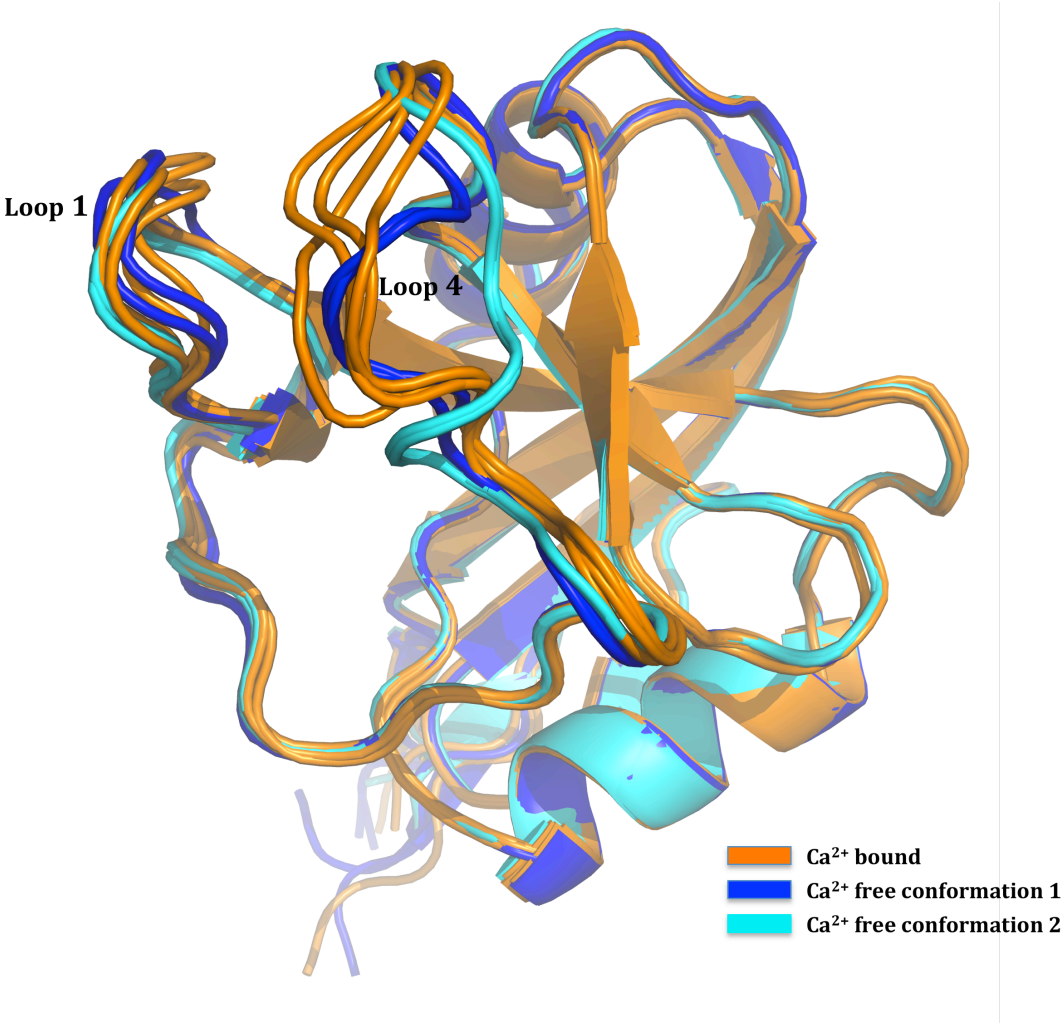

Figure 3.14 Comparison of Ca^{2+}-bound and Ca^{2+}-free derCD23 structures.
Orange: Ca^{2+}-bound derCD23 structures. Blue and cyan: Ca^{2+}-free derCD23 structures (Dr. Stella Fabiane unpublished data). Most of the residues undergoing a conformational change upon calcium binding are also involved in the interaction with IgE (Chapter 5).

3.8.2 Insight into Ca^{2+}-dependent structural changes in derCD23

Comparison of the Ca^{2+}-bound structure and these two different conformations of loop 4 in the Ca^{2+}-free structure reveal structural changes upon calcium binding. The two different conformations of Ca^{2+}-free derCD23 represent independent views of derCD23 in similar packing environments, and are not the result of different crystal packing interactions. In the Ca^{2+}-free structure conformation 1, two calcium binding residues (E249 and D270) remain in a similar position as in the Ca^{2+}-bound structure, whereas structural changes of the T251 side chain are observed. Only E249 remains in a similar

position in the Ca^{2+}-bound structure as in the Ca^{2+}-free structure conformation 2, while both T251 and D270 show structural differences. Residues 249-251 (EPT) show distinct differences between the Ca^{2+}-bound and -free derCD23 structures due to the movement of P250 and T251. In the Ca^{2+}-bound structure, the EPT motif is more bent and P250 adopts a *cis*-conformation in all four copies in the asymmetric unit (Figure. 3.15). The distance between T251 (Oγ1) and E249 (Oε1) is 3.7 Å. In the Ca^{2+}-free structure, the distance between T251 (Oγ1) and E249 (Oε1) is 6.1 Å in conformation 1 and 8.3 Å in conformation 2. In addition, P250 adopts a *cis*-conformation in conformation 1 and a *trans*-conformation in conformation 2. Thus, calcium binding causes movement of calcium site ligands and the *trans* to *cis* isomerization of P250.

Unlike the Ca^{2+}-bound structure, side chains of residues 253-254 in the Ca^{2+}-free structure conformation 1 are disordered. Furthermore, the side chain of R253 in the Ca^{2+}-free structure conformation 2 points into a cavity between loop 1 and loop 4 (Figure 3.16).

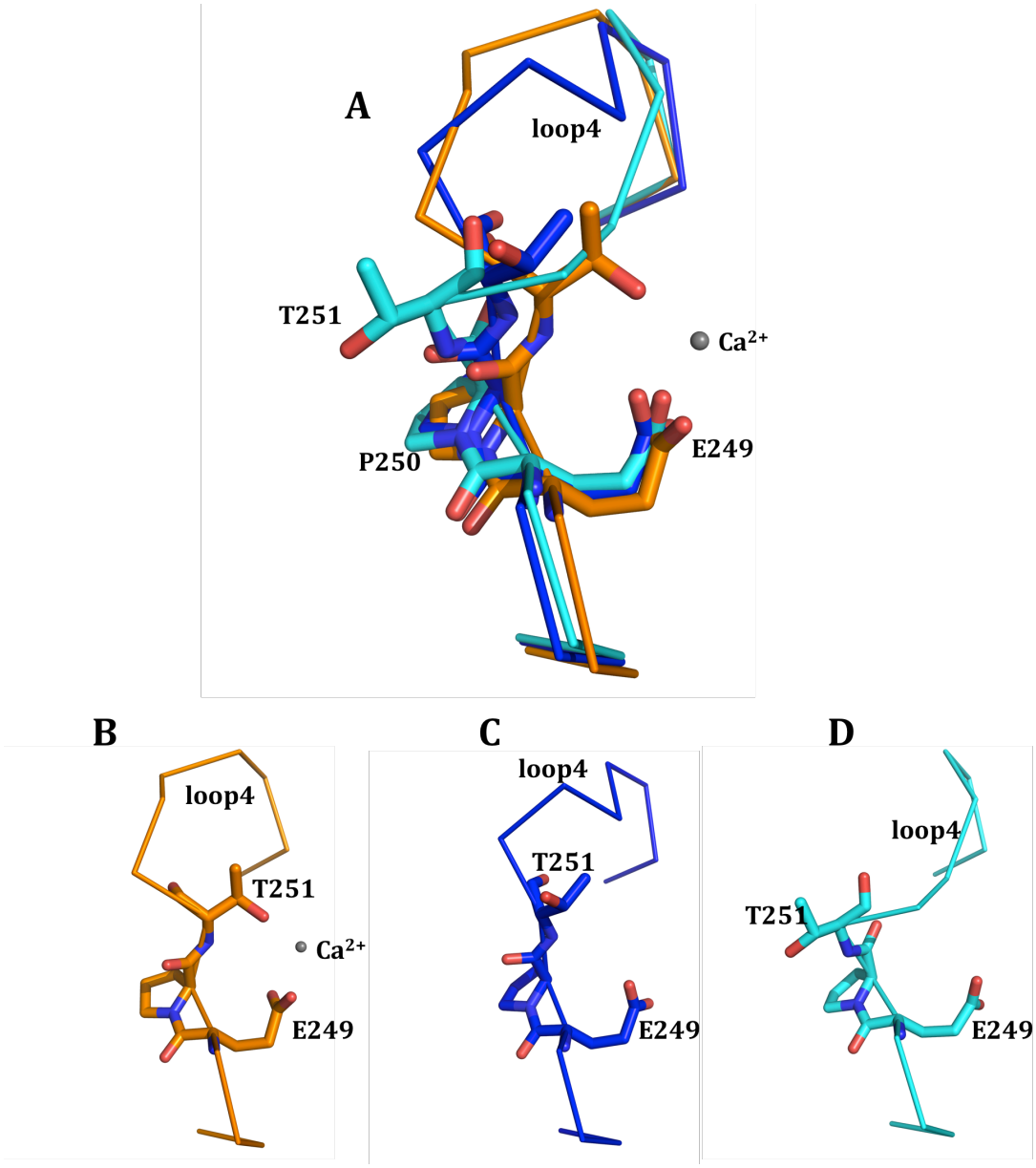

Figure 3.15 Comparison of the E249-P250-T251 conformations in derCD23 structures.
A: Superimposition of EPT motif in Ca^{2+}-bound derCD23 (orange) and two forms of Ca^{2+}-free derCD23 structures (dark and light blue). P250 adopts a *cis*-conformation in the Ca^{2+}-bound structure. P250 adopts a *cis*-conformation in conformation 1 and a *trans*-conformation in conformation 2 of the Ca^{2+}-free derCD23 structure. B: EPT in the Ca^{2+}-bound derCD23 structure. C: EPT in the Ca^{2+}-free derCD23 structure conformation 1. D: EPT in the Ca^{2+}-free derCD23 structure conformation 2.

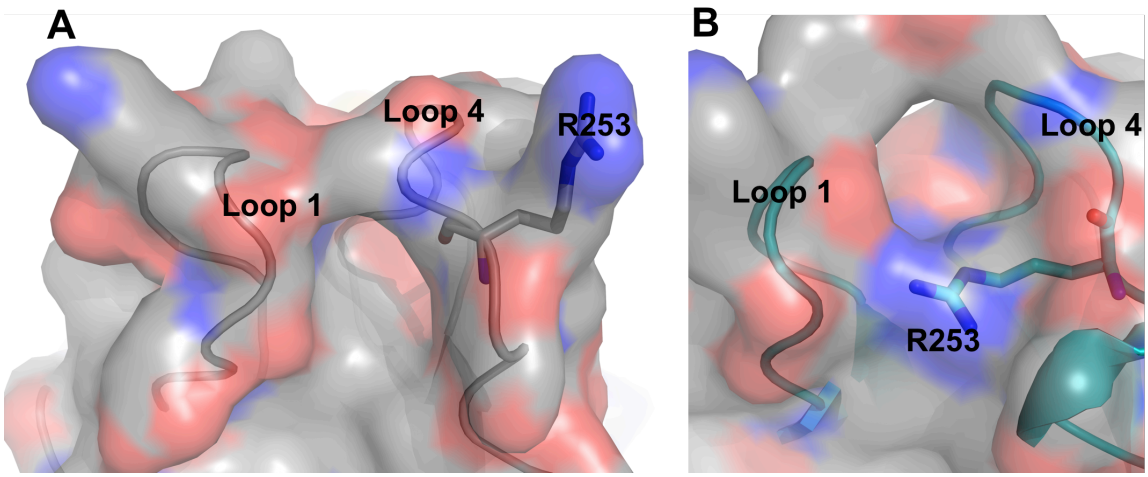

Figure 3.16 The conformation of R253 in derCD23 structures.
A: Ca^{2+}-bound derCD23 structure shows that R253 points away from the head domain. B: Ca^{2+}-free derCD23 structure in the conformation 2 has the R253 occupying the cavity between loop 1 and loop 4.

3.9 Comparison with previously solved CD23 structures

The Ca^{2+}-bound derCD23 structure showed a different Ca^{2+}-binding site to the NMR structure, and different calcium coordination residues to the previous crystal structure of the CD23 double mutant. In addition, loop 4 is well ordered in the Ca^{2+}-bound structures reported in this thesis, compared with the previous Ca^{2+}-bound crystal structure of the CD23 double mutant, in which it is disordered.

In the NMR titration experiment with calcium, observed chemical shifts of residues around Ca^{2+} "site 1", not "site 2", suggested the occupancy of Ca^{2+} in "site 1" (Hibbert *et al.*, 2005). The comparison of Ca^{2+}-bound and Ca^{2+}-free derCD23 structures does indeed show differences in "site 1" residues, and little or no changes in most of the Ca^{2+} "site 2" residues. This may explain why the Ca^{2+} site was inferred to be "site 1" by the NMR titration experiment, although it is surprising that no shifts were observed at "site 2", caused by the presence of Ca^{2+} if not by structural changes in the ligands. In the previous crystal structure of Ca^{2+}-bound CD23 double mutant, N269 is involved in Ca^{2+}-binding, and loop 4 is disordered. A possible reason for the difference is that one of the mutations, G256S, is close to the Ca^{2+}-binding site, and as part of loop 4, this mutation may cause the observed disorder of loop 4 and the changes in Ca^{2+} coordination.

3.10 Isothermal Titration Calorimetry

ITC experiments with derCD23 and the four mutants (see chapter 4 for structural details and section 2.7 for experimental details) showed that wild-type derCD23 and mutant S252A indicate calcium binding, whereas mutants E249A, D258A and D270A showed no measurable calcium binding (Figure 3.17 and Table 3.5).

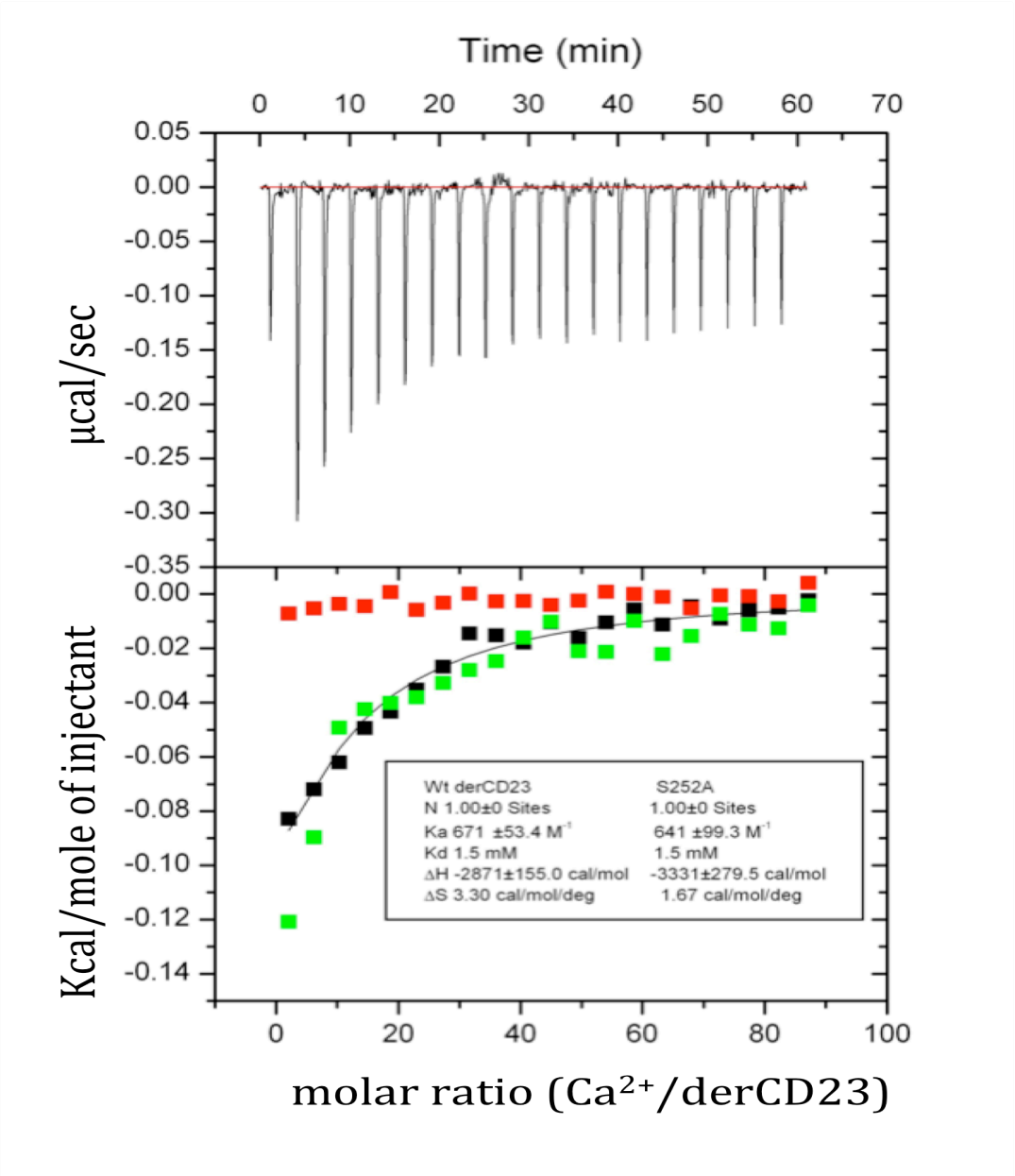

Figure 3.17 Interactions between derCD23 (wild-type and mutants) and calcium studied with ITC.
Black curve and squares: wild-type derCD23. Red squares: E249A. Green squares: S252A. Mutants D270A and D258A showed the same results as E249A. This experiment was performed by Dr. Anthony Keeble.

Calcium binding site*		"Site 2"	"Site 2"	"Site 1"	"Site 1"
Construct	derCD23	Mutant D270A	Mutant E249A	Mutant D258A	Mutant S252A
Binding affinity (K_D)	1.5mM	Not measurable	Not measurable	Not measurable	1.5mM

* For definition of sites refer Figure 3.2.

Table 3.5 Binding affinities of wild-type derCD23 and mutants for calcium studied by Isothermal Titration Calorimetry (ITC).

Wild-type derCD23 and mutant S252A indicate calcium binding with a resulting $K_D = 1.5$ mM, whereas mutants E249A, D258A and D270A showed no measurable calcium binding.

After solving the calcium-bound derCD23 structure, N269 was found not to be involved in calcium binding, even though it belongs to "site 2" according to sequence alignment. Thus, two mutants N269A and N269D were made for ITC experiments to measure their binding affinity with calcium (see section 2.7 for experimental details). N269A and N269D were found to have binding affinities with a $K_D = 0.73$ and 1.5 mM, respectively (Figure 3.18), consistent with N269 not being involved in calcium binding.

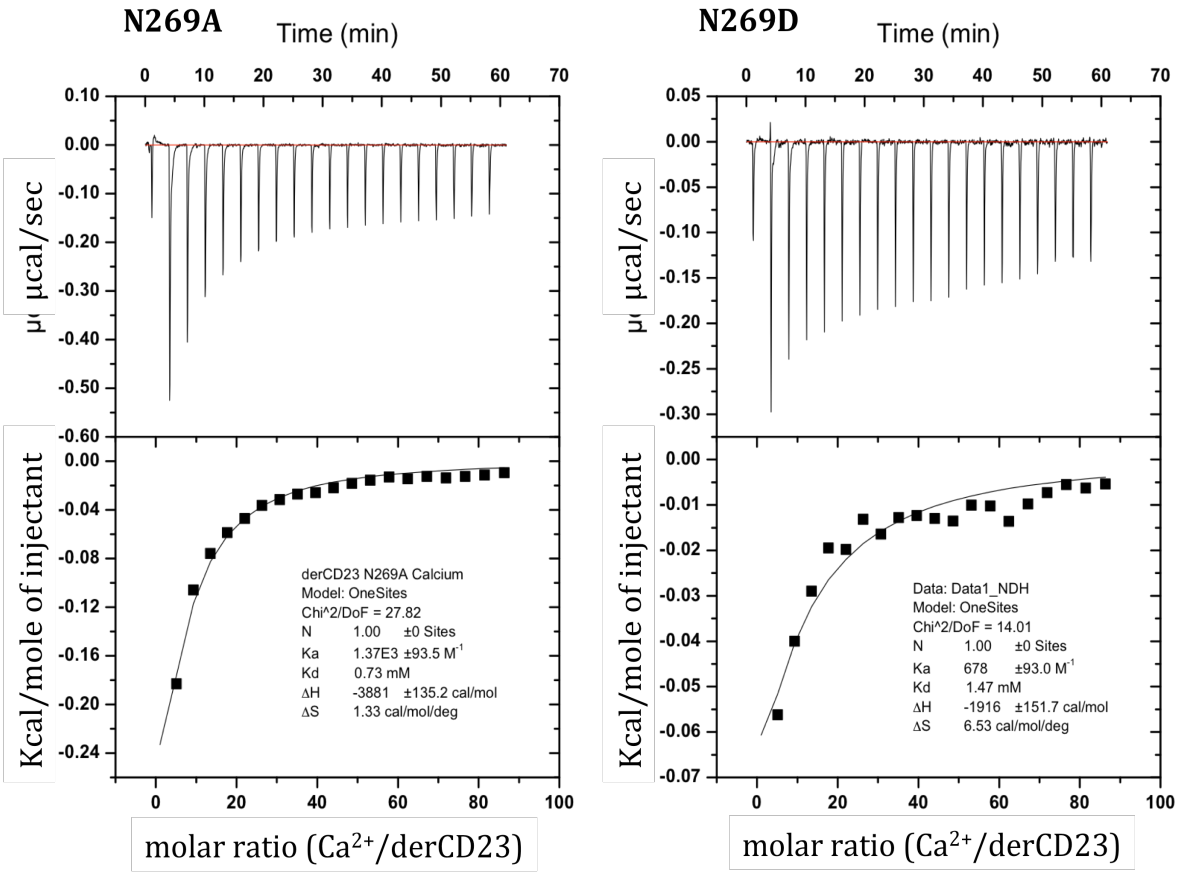

Figure 3.18 Interactions between derCD23 mutants (N269A, N269D) and calcium studied with ITC.
This experiment was performed by Dr. Anthony Keeble.

3.11 Summary and discussion

The low-affinity IgE receptor, CD23, plays a central role in the regulation of IgE synthesis and is involved in other IgE-dependent activities such as allergen presentation and transport. This membrane protein is different from other Ig receptors and belongs to the C-type lectin superfamily. According to the sequence alignment of Ca^{2+} site ligands in various species of CD23 and other C-type lectins, there are two putative Ca^{2+}-binding sites in human CD23 (Figure 3.2). Monomeric derCD23, S156-E298 of the full-length CD23, is a recombinant protein corresponding to the fragment released by *Der p* I, which contains the lectin domain and part of the C-terminal tail. The NMR structure of

derCD23 had previously been determined, and NMR titration experiments indicated Ca^{2+}-binding to "site 1" (Hibbert *et al*., 2005). Then the crystal structure of the CTLD of CD23 double mutant (H213R and G256S) was reported with and without Ca^{2+}, and Ca^{2+} was observed to bind in "site 2" (Wurzburg *et al*., 2006).

This chapter describes the purification, crystallisation and structure determination by X-ray crystallography of the monomeric derCD23 CTLD. ITC experiments are also used to determine the calcium binding affinity and the binding site. Structural comparison of Ca^{2+}-bound and -free structures reveals the effect of calcium on the structure of CD23 head domain.

The crystal structure of Ca^{2+}-bound derCD23 was determined at 2.0 Å resolution, and resolves previous controversy concerning the Ca^{2+} binding site. The structure of derCD23 displays the typical tertiary structural arrangement of other CTLDs. There are four Ca^{2+}-bound derCD23 molecules in the asymmetric unit of this crystal form. Superimposition of all 4 copies reveals similar arrangement of the head domain and only slight variations in loop 1, but more differences in loop 4. CD23 contains two potential calcium binding sites according to sequence alignment, but "site 1" is not well conserved in human CD23. This explains no calcium binding to site 1 in human CD23. The structure reported here shows that calcium binds to "site 2", and has a different coordination compared with a previously solved CD23 (double mutant) structure. Three residues (E249, T251 and D270) provide 4 oxygen atoms and 3 water molecules provide 3 oxygen atoms involved in the binding to Ca^{2+}. The geometry of the calcium coordination is pentagonal bipyramidal formed by seven ligands. The coordination is different from the pentagonal bipyramidal with one bisected apex, formed by eight ligands, in site 2 of MBP, DC-SIGN and human asialoglycoprotin receptor-I (ASGPR-I) (Meier *et al*., 2000; Snyder *et al*., 2005; Weis *et al*., 1992; Wurzburg *et al*., 2006). This is probably the result of the fact that there is no carbohydrate binding to derCD23 (Section 3.7).

ITC experiments with derCD23 and the initial four mutants (see chapter 4 for structural details and section 2.7 for experimental details) were also used to determine calcium-

binding site. Wild-type derCD23 and calcium-binding "site 1" mutant S252A indicate calcium binding with a K_D = 1.5 mM, whereas "site 2" mutants E249A and D270A showed no measurable calcium binding (Figure 3.17 and Table 3.5). These results confirm that calcium binds to "site 2". The structure of "site 1" mutant D258A explains the result of no measurable calcium binding of this mutant and will be described in chapter 4. The concentration of calcium in human serum is about 2 mM, which is around the binding affinity of derCD23 with calcium. This indicates that calcium-bound and -free derCD23 may be in a equilibrium that may have an important physiological role (see chapter 7).

According to the alignment of CD23 sequences from various species, N269 is expected to be a calcium ligand and is seen as such in the derCD23 double mutant structure. Surprisingly, N269 is not involved in the binding to Ca^{2+} in the derCD23 structure reported in this thesis. Therefore, N269 was mutated for biophysical study and the mutants N269A and N269D were produced. Mutation of N269 in derCD23 does not weaken Ca^{2+} binding in ITC experiments, indicating that the crystal structure is correct. There is a mutation (G256S) close to the calcium binding site in the previous CD23 double mutant structure, and this may be the reason for the N269 involvement in calcium binding in that structure.

Comparison of the Ca^{2+}-bound derCD23 structure with Ca^{2+}-free derCD23 shows residues undergoing a conformational change upon Ca^{2+} binding. Calcium binding to derCD23 causes movement of T251, which drives P250 from the *trans*-conformation to the *cis*-conformation. Isomerisation of this conserved proline residue was also observed in mannose-binding protein (Ng *et al*., 1998). In addition, loop 4 was locked in a particular conformation that may be preferred for IgE binding. The role calcium plays in increasing IgE binding affinity will be described in chapter 5 and the final discussion (chapter 7).

Chapter 4:
Crystal structures of derCD23 Ca^{2+} site mutants

4.1 Introduction

Putative Ca^{2+} "site 1" mutants (S252A, D258A) and "site 2" mutants (E249A, D270A) were studied by ITC, measuring their binding affinities for Ca^{2+} (see chapter 3). However, it is a common phenomenon to have unexpected secondary effects in such a mutagenesis study. Mutation of one residue may have an effect on other residues nearby, or even influence residues far from them. Thus, to complement the ITC experiments, it is informative to solve crystal structure of these mutants to see whether there are structural changes in addition to the mutated residues.

Site directed mutagenesis was used to produce derCD23 mutant constructs, which were expressed and purified subsequently as described in chapter 2. 10 mg protein was typically obtained from 1 litre of cell culture for all mutants except S252A, which had a yield of 20 mg/litre.

4.2 Crystallisation

4.2.1 Initial crystallisation attempts

Initially, all four mutants were set up for crystallisation in the similar conditions as wild-type derCD23 with no added calcium. However, only diffraction quality crystals of derCD23 mutant S252A were obtained. The other mutants did not give diffraction quality crystals. Then the structure and crystal packing of wild-type derCD23 was analyzed in COOT. This showed that only residue S252 of the four mutated residues has no interactions with residues in the same derCD23 molecule or other molecules around it in the crystal (Figure 4.1). The other three residues have no inter-molecular packing interactions either, but are all partially buried and involved in intra-molecular

interactions (Figure 4.1). It is therefore possible that derCD23 mutants E249A, D258A and D270A cannot pack in the same way as wild-type derCD23.

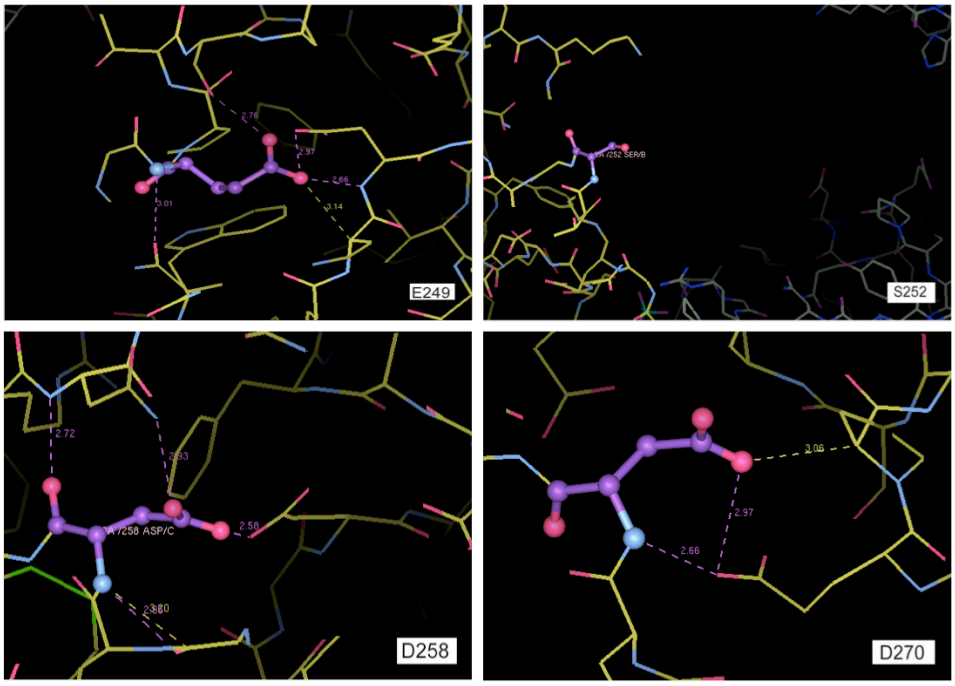

Figure 4.1 Putative Ca^{2+} site ligands E249, S252, D258 and D270 in the structure of wild-type derCD23.
The four residues are highlight in ball and stick. Only S252 makes no contacts with other protein residues.

4.2.2 Crystal screening

The other three derCD23 mutants (E249A, D258A, D270A) at 5 mg/ml in 20 mM Tris pH 7.5, 125mM NaCl, were set up for crystal screening. Crystals of these three derCD23 mutants were obtained by the hanging drop vapour diffusion method from crystal screening at 18°C after two weeks. Crystals of mutant E249A were grown in 0.2 M potassium thiocyanate, 0.1 M bis-tris-propane pH 8.5, 20% (w/v) PEG 3350, and 20% glycerol was used as cryoprotectant prior to flash-cooling. Crystals of mutant D258A were produced in 18% ethanol, 4% PEG 400, 0.1 M sodium acetate pH 5.0, and 25% glycerol was used as cryoprotectant. Crystals of mutant D270A were obtained in

30% PEG 4000, 0.3 M ammonium sulphate, and flash-frozen in liquid nitrogen using 20% glycerol as croprotectant.

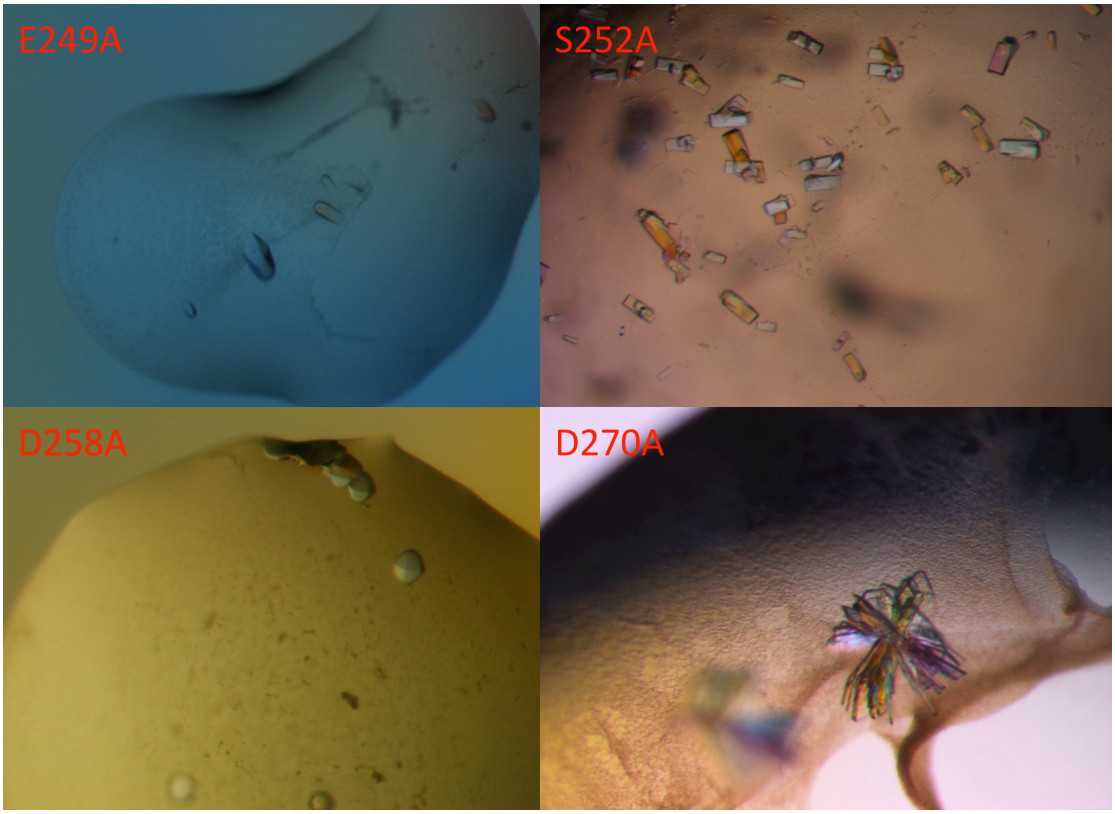

Figure 4.2 Crystals of derCD23 mutants.
Crystals of derCD23 mutants E249A (typically100×50×30 µm), S252A (60×30×20 µm), D258A (50×50×20 µm) and D270A (separated single crystal 160×60×20 µm).
E249A in 0.2 M potassium thiocyanate, 0.1 M bis-tris-propane pH 8.5, 20% (w/v) PEG 3350. S252A in 18.5% PEG 6000, 2% 1,6-hexanediol, 0.05M ammonium sulphate, 0.1M sodium acetate pH 4.7. D258A in 18% ethanol, 4% PEG 400, 0.1 M sodium acetate pH 5.0. D270A in 30% PEG 4000, 0.3M ammonium sulphate.

4.3 Data collection and processing

4.3.1 Data collection and processing

Data from all crystals were collected at the Diamond Synchrotron using a q315 CCD detector, and processed using HKL2000 or MOSFLM.

	E249A	S252A	D258A	D270A
Space group	$P4_122$	$P1$	$P6_5$	$P2_12_12_1$
Unit-cell parameters (Å)	a = 63.32 b = 63.32 c = 261.42 α = 90.00 β = 90.00 γ = 90.00	a = 52.50 b = 56.87 c = 62.68 α = 68.06 β = 88.23 γ = 73.53	a = 90.97 b = 90.97 c = 351.68 α = 90.00 β = 90.00 γ = 120.00	a = 73.78 b = 109.11 c = 139.00 α = 90.00 β = 90.00 γ = 90.00
Wavelength (Å)	0.9763	0.9795	0.9763	0.9795
Resolution range (highest shell) (Å)	65.4-2.27 (2.40-2.27)	50.0-1.95 (2.02-1.95)	58.67-2.80 (2.95-2.80)	50.0-2.25 (2.33-2.25)
Number of unique reflections	25713	45157	36967	54601
Redundancy	12.6 (13.0)	2.2 (2.1)	3.6 (3.5)	7.0 (6.7)
Completeness (%)	100 (100)	97.1 (93.7)	91.6 (94.3)	99.7 (99.5)
I/σ (I)	12.9 (2.3)	20.0 (2.0)	7.0 (1.9)	34.0 (4.0)
$R_{merge/pim}$ (%)	*2.0 (35.9)	^4.9 (36.9)	*8.1 (40.0)	^7.8 (46.3)

Table 4.1 Data collection and refinement statistics of derCD23 mutants. Values in parentheses are for the highest resolution shell.

$^{R_{merge}} = \Sigma_{refl}\Sigma_i|I_i - I_{aver}|/\Sigma_{refl}\Sigma_i I_i$, where I_i is the intensity of a i^{th} measurement of a reflection I_{aver} the average intensity for that reflection, calculated on all the measurements acquired for that reflection. Σ_{refl} indicates the sum calculated over all the independent reflections measured.

$*R_{pim} = \Sigma_{refl}(1/(n_{refl}-1))\Sigma_i|I_i - I_{aver}|/\Sigma_{refl}\Sigma_i I_i$, where n_{refl} is the number of observations of reflection.

4.3.2 Determination of space group and number of molecules in the asymmetric unit

The space group and Matthews coefficient calculation of the four derCD23 mutants are shown in table 4.2.

	E249A	S252A	D258A	D270A
Space group	$P4_122$	$P1$	$P6_5$	$P2_12_12_1$
Molecules per asymmetric unit	3	4	8	7
Matthews coefficient	2.65Å^{3}Da^{-1}, 53.6% solvent	2.51Å^{3}Da^{-1}, 51.1% solvent	3.18Å^{3}Da^{-1}, 61.3% solvent	2.42Å^{3}Da^{-1}, 49.2% solvent

Table 4.2 The space group and Matthews coefficient calculation for the four derCD23 mutants.

4.4 Structure solution, refinement and validation

The structures of all mutants were solved by molecular replacement using PHASER with PDB 2H2T or 2H2R as the search model. In order not to bias the electron density map calculations, water molecules were removed from the search model.

Manual model building was carried out with COOT, coupled with refinement using REFMAC5 and PHENIX. The progression of the refinement was monitored using R factors (R_{work} and R_{free}), and TLS refinement (Painter and Merritt, 2006) was implemented by finding TLS groups in PHENIX. NCS restraints were used to all chains and B-factor refinement was applied. Strategies and parameters used in the final stage of refinement are listed in Table 4.3. Protein atoms of the backbone were modeled first. SO_4^{2-}, water and glycerol molecules were modeled according to electron density at a later stage using the R_{free} as a guide. Only two disulphide bonds were found to be broken due to the radiation damage, and no calcium was modeled into any of the mutant structures (note that no calcium was present in the crystallisation buffer). Electron density was observed in calcium-binding site 2 of the S252A structure (chains A and B), and one water molecular was modeled into this site. Calcium ion was also tried, but it gave an unusually high B-factor value (100 Å^2) compared with surrounding protein residues (40 Å^2) and water molecules (35 Å^2). Statistics of the refinement results of these four mutant structures are listed in Table 4.4.

	E249A	S252A	D258A	D270A
Refinement program	REFMAC	PHENIX	REFMAC	PHENIX
B-factor refinement	isotropic	isotropic	isotropic	isotropic
TLS groups	one group for each chain	chain A: 9 chain B: 10 chain C: 7 chain D: 10	one group for each chain	chain A: 11 chain B: 12 chain C: 9 chain D: 7 chain E: 9 chain F: 5 chain G: 8
NCS restraints	local NCS	-	medium restraints with residues: 160-224, 232-250, 259-288 for each chain	-

Table 4.3 Strategies and parameters used in the final stage of refinement of derCD23 mutant structures.
Definitions of parameters in the above table are in chapter 2.

	E249A	S252A	D258A	D270A
Protein residues in each chain	A: 157-292 B: 160-288 C: 158-292	A: 157-291 B: 158-291 C: 159-290 D: 159-288	A: 158-292 B: 158-292 C: 158-291 D: 158-292 E: 158-292 F: 158-292 G: 158-292 H: 158-291	A: 156-289 B: 156-288 C: 156-290 D: 159-290 E: 156-289 F: 159-291 G: 160-288
Broken disulphide bonds	-	chain D C160-C288 (broken)	-	chain G C163-C174 (half-broken)
Water molecules	125	409	163	471
Calcium ions	-	-	-	-
SO_4^{2-}	-	4	-	25
Glycerol	1	4	2	12
Average B ($Å^2$):				
Protein	31.6	40.4	51.0	43.5
Water molecules	46.3	45.8	30.4	45.7
Calcium ions	-	-	-	-
Glycerol	42.1	61.7	60.9	67.8
SO_4^{2-}	-	82.5	-	74.7
R_{work}/R_{free}(%)	20.5/25.1	16.6/21.2	20.8/25.1	18.1/22.6
r.m.s. deviations	bond lengths = 0.010 Å bond angles = 1.375°	bond lengths = 0.007 Å bond angles 1.031°	bond lengths = 0.006Å bond angles 0.987°	bond lengths = 0.006 Å bond angles 0.937°

Table 4.4 Statistics of the refinement results of the final derCD23 mutant structures.
$R_{work} = \Sigma||F_{obs}| - |F_{calc}||/\Sigma|F_{obs}|$, where F_{obs} and F_{calc} are the observed and calculated structure factor amplitudes.
$R_{free} = \Sigma_t||F_{obs}| - |F_{calc}||/\Sigma_t|F_{obs}|$, where F_{obs} and F_{calc} are the observed and calculated structure factor amplitudes, and $_t$ is the test set of data omitted from refinement (5% in this case).

4.5 Structure analysis

4.5.1 Overview of the derCD23 mutants structures

Although the crystals of the four mutants have different space groups and numbers of molecules in the asymmetric unit (Figure 4.3), the structures are all very similar except for two loops (loop 1 and loop 4). There are no substantial effects of the mutations on other parts of the structure. Superimposition of wild-type derCD23 and all four mutant structures reveals large differences in loop 4 and small differences in loop 1. Calcium binding to derCD23 causes movement of calcium binding residues in "site 2", isomerisation of P250 and changes in loop 4, as described in chapter 3. These structural changes can be used to compare the mutant structures with calcium-bound and -free structures. The structure of the S252A mutant displays two conformations of loop 4, which are similar to those seen in the calcium-free derCD23 structure. The structure of the E249A mutant shows a similar conformation for loop 4 as calcium-bound derCD23, while the D258A and D270A loop 4 structures are similar to the calcium-free conformation 2 (Figure 4.4).

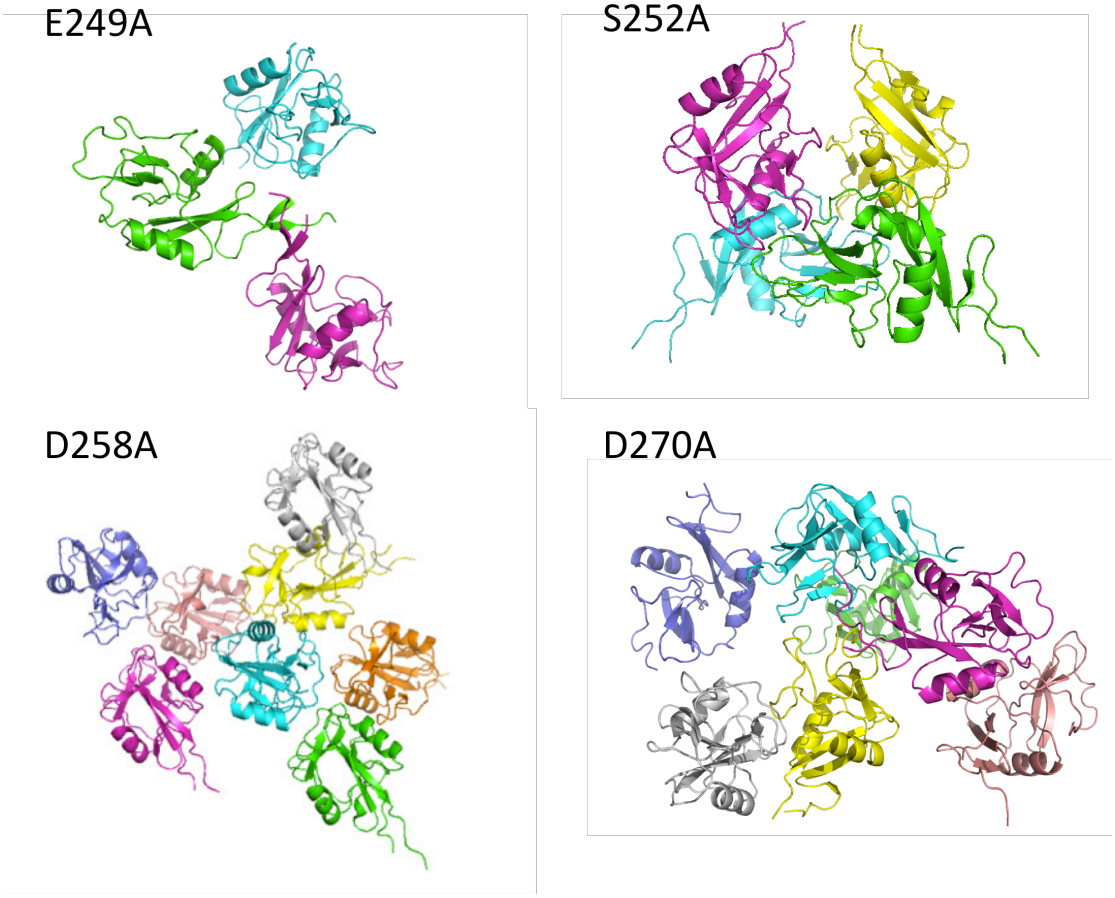

Figure 4.3 Crystal structures of the four derCD23 mutant structures showing the contents of the asymmetric unit in each case.
They have different numbers of molecules (3, 4, 8 and 7 respectively) in the asymmetric unit.

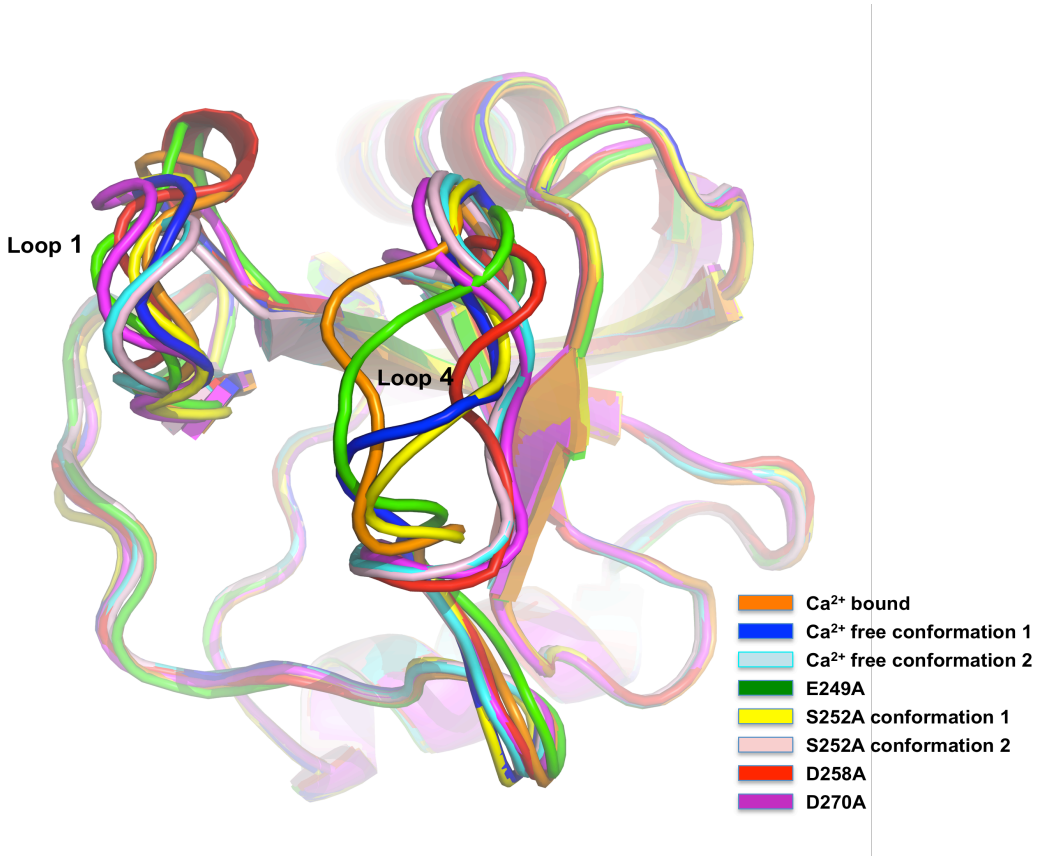

Figure 4.4 Superimposition of wild-type derCD23 structures with and without calcium, and all four mutant structures.

4.5.2 Ca^{2+}-binding site

In chapter 3, ITC was used to measure the binding affinities of derCD23 mutants for calcium in order to determine the calcium binding site(s) and ligands. The crystal structures of these mutants were solved to see whether there are structural changes in addition to the mutated residues. Comparison of wild-type derCD23 and the four calcium site mutant structures indicate no substantial structural changes in the calcium binding site except for the mutations themselves (Figure 4.5). Calcium binding residues in these four mutant structures are in essentially the same positions as either the calcium-bound or calcium-free derCD23 structures. P250 is *cis* in conformation 1 and *trans* in conformation 2 in the structure of S252A, *cis* in E249A, and *trans* in the D258A and D270A structures (Table 4.5).

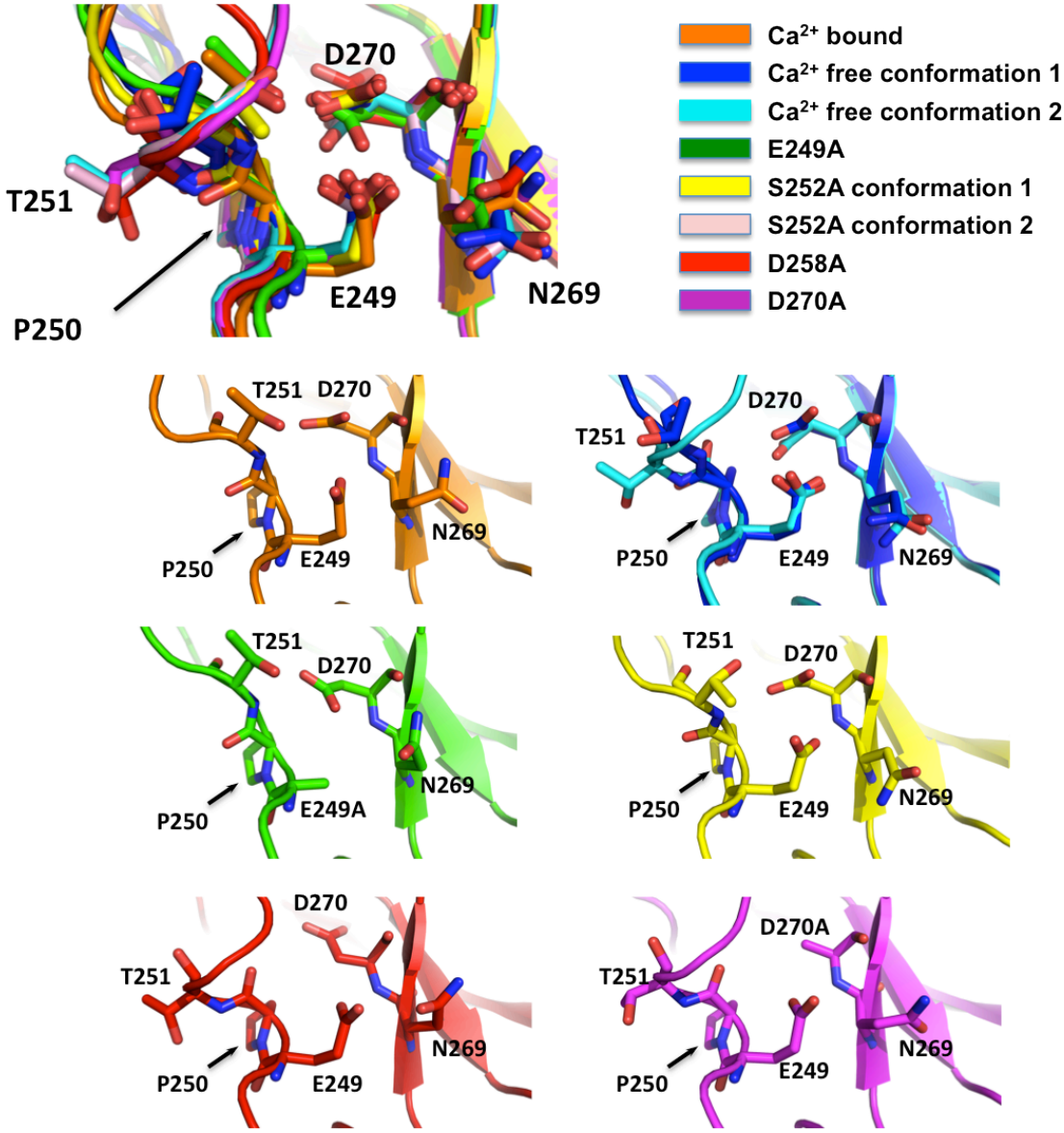

Figure 4.5 Wild-type derCD23 with and without calcium and all four mutant structures, showing the calcium binding "site 2".
The top panel shows all the structures superimposed; the individual structures are shown below.

	Number of molecules in the asymmetric unit	P250 conformation
Ca^{2+}-bound	4	*Cis*
Ca^{2+}-free conformation1	2	*Cis*
Ca^{2+}-free conformation2	2	*Trans*
E249A	3	*Cis*
S252A conformation1	2	*Cis*
S252A conformation2	2	*Trans*
D258A	8	*Trans*
D270A	7	*Trans*

Table 4.5 Comparison of wild-type derCD23 with and without calcium, and all four mutant structures to show their P250 conformation.

In the calcium-binding site of the D258A structure, R253 occupies the position for calcium binding in all eight molecules (Figure 4.6). This is a unique feature among all derCD23 and mutants structures. In the Ca^{2+}-free CD23 double mutant structure, R253 also points towards the calcium binding site but has different interactions with surrounding residues. In addition, in the D258A mutant, P250 adopts the *trans* conformation that is observed in the Ca^{2+}-free derCD23 structure conformation 2. These two features, the location of R253 and the *trans* conformation of P250, may be the reason for the observed lack of binding affinity of this mutant to calcium in the ITC experiment, despite the fact that D258 is not a calcium-binding ligand in the calcium-bound derCD23 structure.

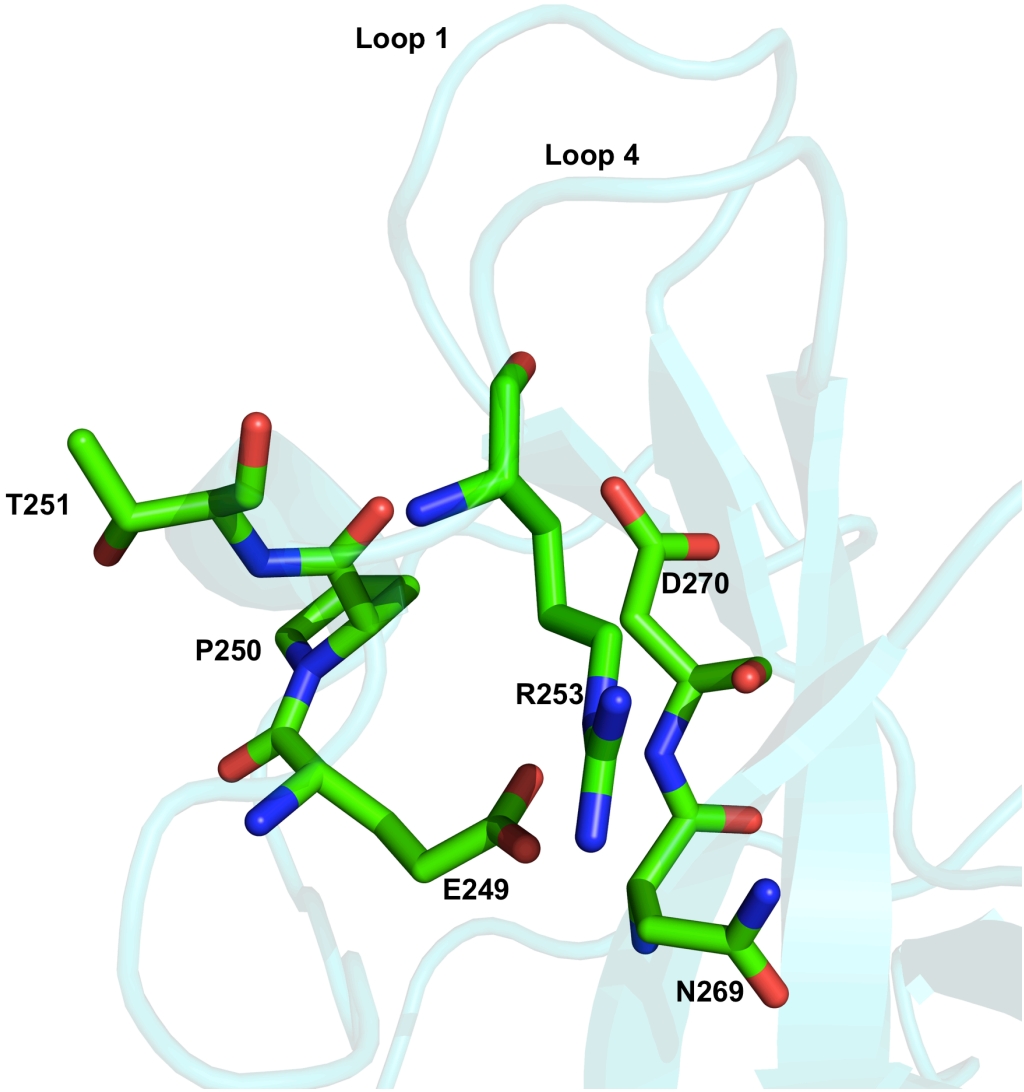

Figure 4.6 Ca^{2+}-binding site in the structure of D258A.
P250 adopts the *trans* conformation, and R253 occupies the position for calcium binding. This R253 interacts with the side chain of E249 and main chain of D270, which is probably another reason for the loss of binding ability to calcium in the ITC experiments (Section 3.10).

4.6 SPR studies of wild-type derCD23 and mutants binding to IgE-Fc

To investigate the role calcium plays in the binding of CD23 with IgE, surface plasmon resonance was used to characterize the interaction between wild-type derCD23 and the mutants with IgE-Fc. IgE-Fc was passed over immobilized wild-type derCD23 or the mutants (see chapter 2 for experimental details). The results are shown in Table 4.6 and Figure 4.7. In these SPR experiments, calcium increases CD23's binding affinity to IgE

7-fold, which is consistent with previously published SPR data (Hibbert *et al*., 2005). In addition, calcium also increases S252A's binding affinity to IgE 7-fold. S252A, N269A and N269D can bind calcium (as determined by ITC), therefore they are expected to behave in the same way as the binding of wild-type derCD23 to IgE-Fc. This is confirmed by the SPR data, although they present 2-fold higher or lower affinity compared with wild-type derCD23. Because E249A, D258A and D270A have lost the ability to bind calcium, they are expected to have the same binding affinity to IgE-Fc as calcium-free derCD23. In fact, E249A and D270A show binding affinities that are more similar to wild-type derCD23 in the presence of calcium than in the absence of calcium. A further surprising result is that the binding affinity between D258A and IgE-Fc is not measurable. However, we know that mutation of calcium binding site residues causes variation of the conformation of loop 4 (Figure 4.4), which is involved in binding to IgE (Chapter 5), and this may influence the binding of the calcium site mutants to IgE-Fc.

	$Ca^{2+}(K_D)$	No $Ca^{2+}(K_D)$
WT	$4.8\pm0.6\times10^{-6}$ M	$37.6\pm1.00\times10^{-6}$ M
S252A	$2.5\pm0.4\times10^{-6}$ M	$16.8\pm0.60\times10^{-6}$ M
E249A	$5.0\pm0.5\times10^{-6}$ M	No experiment
D270A	$11.1\pm2.2\times10^{-6}$ M	No experiment
D258A	Not measurable	No experiment
N269A	$7.5\pm0.9\times10^{-6}$ M	No experiment
N269D	$10.8\pm1.2\times10^{-6}$ M	No experiment

Table 4.6 SPR studies of the binding affinity of IgE-Fc to immobilised wild-type derCD23 or mutants.

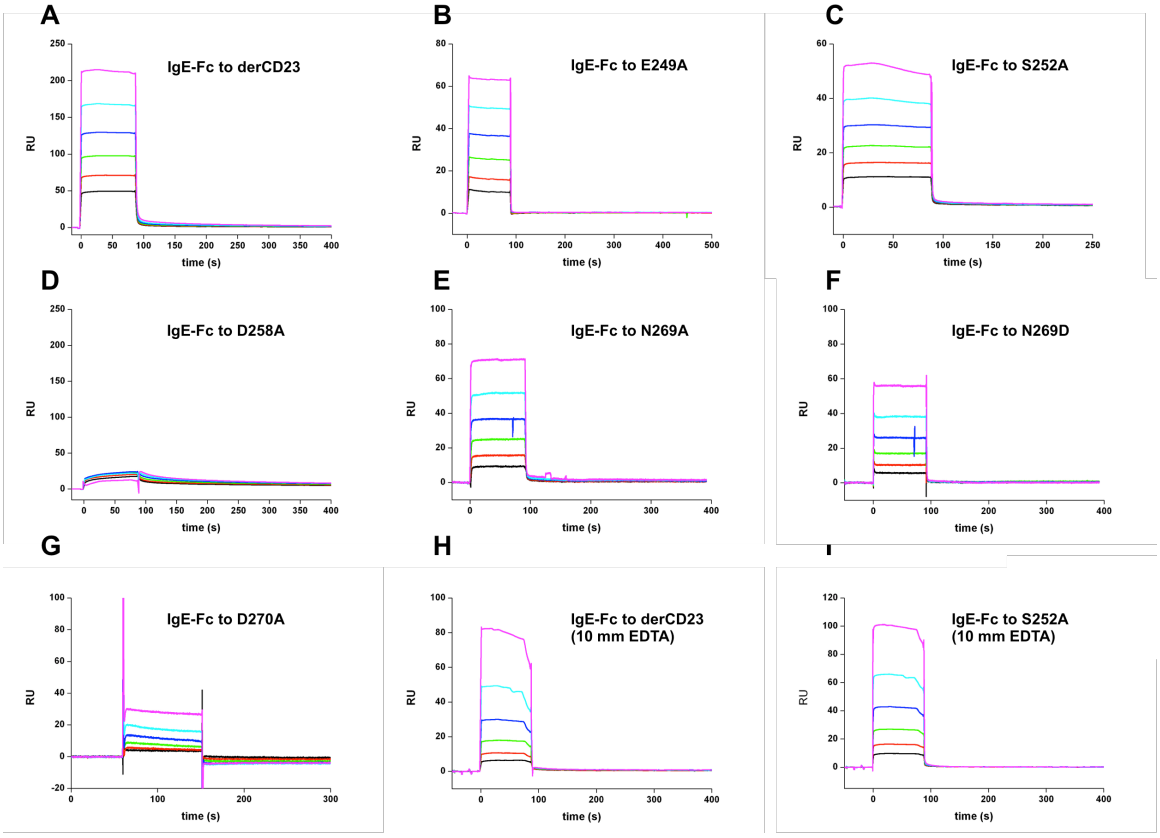

Figure 4.7 Surface plasmon resonance analysis of IgE-Fc binding to immobilized wild-type derCD23 and mutants.
The binding was determined over a range of ligand concentrations: 62.5 (black), 125 (red), 250 (green), 500 (blue), 1000 (cyan) and 2000 nM (pink). Representative sensorgrams are shown here.

4.7 Summary and discussion

This chapter describes the crystallisation and structure determination by X-ray crystallography of four derCD23 mutants. Surface plasmon resonance was used to characterize the interaction between wild-type derCD23 and the mutants with IgE-Fc.

S252A was crystallised in similar conditions as wild-type derCD23. The three other derCD23 calcium binding site mutants (D258A, E249A, D270A) were crystallised in different conditions. They gave different space groups and numbers of molecules in the asymmetric unit. The overall structures of the four mutants are similar to the wild-type derCD23 structure, while loop 1 and loop 4 are observed in different conformations

(Figure 4.4). Calcium binding residues in these four mutant structures are in the same positions as either calcium-bound or calcium-free derCD23 structures (Figure 4.5). However, isomerisation of P250, shown in the calcium-free derCD23 structure, was also observed in the two conformations of the S252A structure. The other three mutants have only *cis* or *trans*-P250. It is possible that the mutations affect the isomerisation state of P250. Overall these structures indicate that mutation of calcium binding site residues has a substantial influence on loop 4, but little effect on other residues of the calcium binding site.

In chapter 3, ITC experiments were used to determine the residues involved in calcium binding by measuring the binding affinity of the mutants to calcium. D258A was found to show no binding affinity with calcium, even though D258 is not a calcium ligand. The crystal structure now shows that the likely reason for this is the *trans*-P250 in D258A, which is not permissive for calcium binding. Also in the crystal structure of D258A, R253 occupies the position for calcium binding, which may be another reason for the lack of calcium binding to D258A.

Surface plasmon resonance was used to characterize the interaction of wild-type derCD23 and the mutants with IgE-Fc. Calcium increases CD23's binding affinity to IgE 7-fold, which is consistent with previous published SPR data (Hibbert *et al*., 2005). Calcium also increases 7-fold the IgE-binding affinity of S252A, which binds calcium with similar values as wild-type derCD23 and shows very similar structural features as calcium-free derCD23. S252A, N269A and N269D can bind calcium (as determined by ITC), therefore they behave as the binding of wild-type derCD23 to IgE-Fc. However, some of the mutants show unexpected results in their binding affinities to IgE-Fc (Section 4.6). Although E249A and D270A have lost the ability to bind calcium, they show binding affinities that are more similar to wild-type derCD23 in the presence of calcium than in the absence of calcium. Furthermore, it is surprising that the binding affinity between D258A and IgE-Fc is not measurable. The reason may be the structural changes that occur in loop 4, which is involved in IgE binding (see chapter 5).

Chapter 5:
Crystal structure of the Ca^{2+}-bound derCD23/Fcε3-4

5.1 Introduction

IgE plays a central role in allergic diseases. CD23, the low-affinity IgE receptor, regulates IgE synthesis through interaction with membrane bound IgE and CD21, and is also involved in allergen presentation and transport (see chapter 1). Structural studies of the IgE/CD23 complex may reveal details of the molecular mechanism of allergic diseases and lead to CD23-targeted drug design.

The first indication of the IgE binding site on CD23 came in 1989, with mutagenesis and monoclonal antibody binding studies which suggested residues 165-190 and 224-256 were involved (Bettler *et al*., 1989; Bettler *et al*., 1992). In addition, the CD23 binding site in IgE-Fc was located in the Cε3 domain (Nissim *et al*., 1991; Vercelli *et al*., 1989). NMR titration experiments by adding Cε3 to isotopically labelled derCD23 showed residues W184, R188, Y189, A190, L198, H202, I221, G222, R224, N225, L226, W234, V235, A271, C273, D274, K276, and A279 in derCD23 were involved in binding to IgE (Figure 5.1) (Hibbert *et al*., 2005), and recently the site in Cε3 has been mapped by NMR with isotopically labelled Cε3 domain (Borthakur *et al*., 2012).

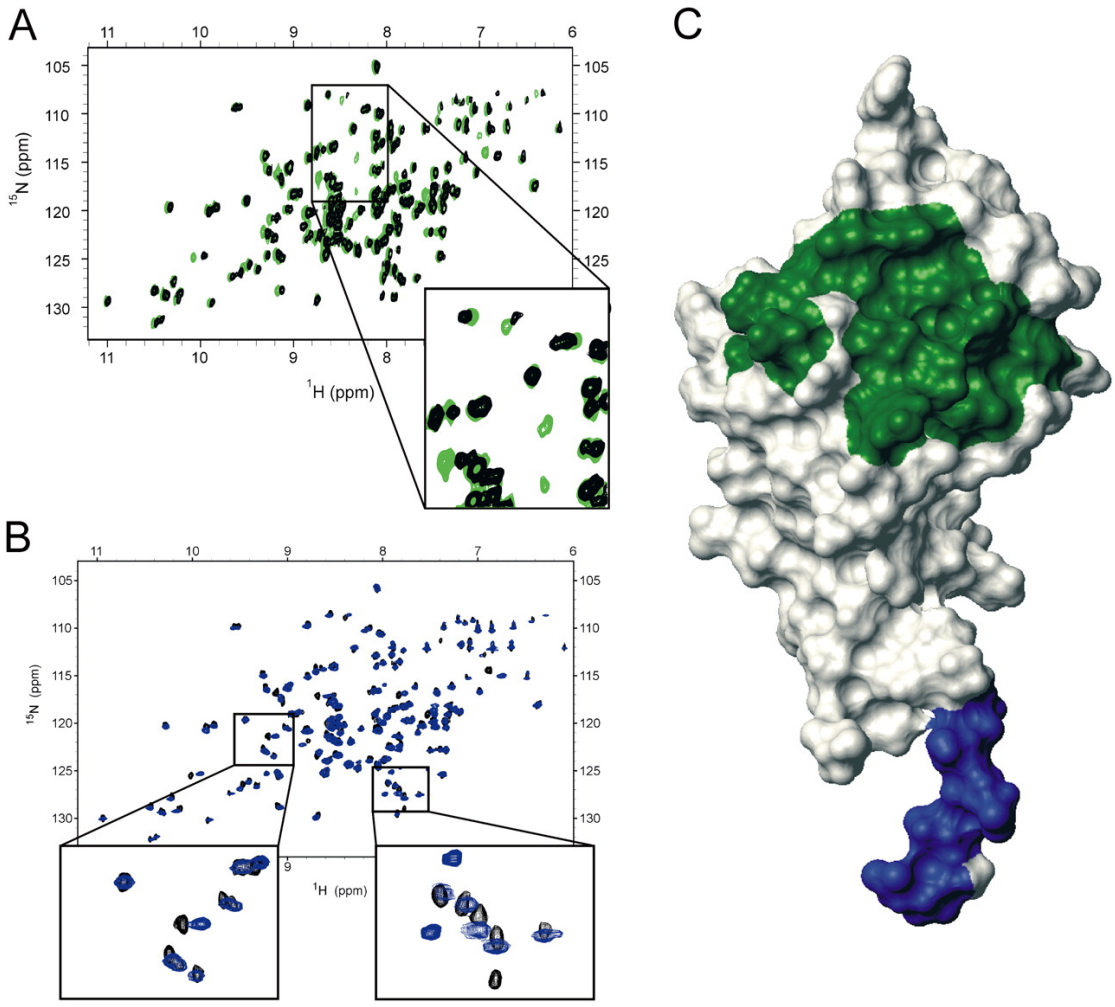

Figure 5.1 ^{1}H-^{15}N chemical shift perturbation experiments define binding surfaces on derCD23 for Cε3 and CD21(D1-2).
A and B: Example spectra of residues that show chemical shift perturbation on addition of Cε3 or CD21(D1-D2). C: The binding site for Cε3 is coloured green and the binding site for CD21 (D1-2) is coloured blue. (Figure taken from Hibbert *et al*., 2005)

Six years ago, the group of Jardetzky tried to crystallise the complex of CD23 with Fcε3-4, but they only obtained crystals of CD23 (Wurzburg *et al*., 2006). However, the CD23 that they used is a double mutant. One of these mutations is G256S, which is on the IgE binding loop according to the previous mutagenesis study. Thus, this experiment was repeated using wild-type proteins (Fcε3-4 and derCD23), a different buffer, and mixing them in different ratios.

After crystallisation of the complex of Fcε3-4 and derCD23, the structure was solved at 3.1 Å resolution, but surprisingly it was found to have no calcium bound to it despite

the presence of 2 mM calcium in the crystallisation buffer (Dhaliwal *et al*., 2012). Then soaking and co-crystallisation with calcium were used to obtain the calcium-bound derCD23/Fcε3-4 structure. The co-crystallisation method gave higher resolution diffraction. This chapter presents the structure of this calcium-bound complex at a resolution of 3.3 Å. Comparison with the calcium-free derCD23/Fcε3-4 structure reveals the role calcium plays in IgE binding.

5.2 Crystallisation

5.2.1 Crystallisation of "calcium-free" derCD23/Fcε3-4 complex

Protein solution (0.22 mM Fcε3-4 and 0.44 mM derCD23 in 20 mM NaCl, 25 mM Tris 7.5, 0.05% sodium azide, 4 mM $CaCl_2$) was mixed 1:1 with precipitant for initial screening at 18°C using the hanging drop method. Crystals were obtained in about 10 days in two conditions: MembFac F10 (0.2 M Sodium acetate trihydrate, 0.1 M Tris pH 8.5, 15% PEG 4000) and Procomplex E5 (0.1 M Tris pH 8.0, 8% PEG8000). Crystals obtained from these two crystallisation conditions have different morphology (Figure 5.2), but both of them diffract to about 3 Å resolution after optimization. Data were collected at the Diamond Synchrotron, and the structure of the complex was solved by Dr Balvinder Dhaliwal (Dhaliwal *et al*., 2012). No calcium was found to be present in the structure, which will be referred as the calcium-free complex.

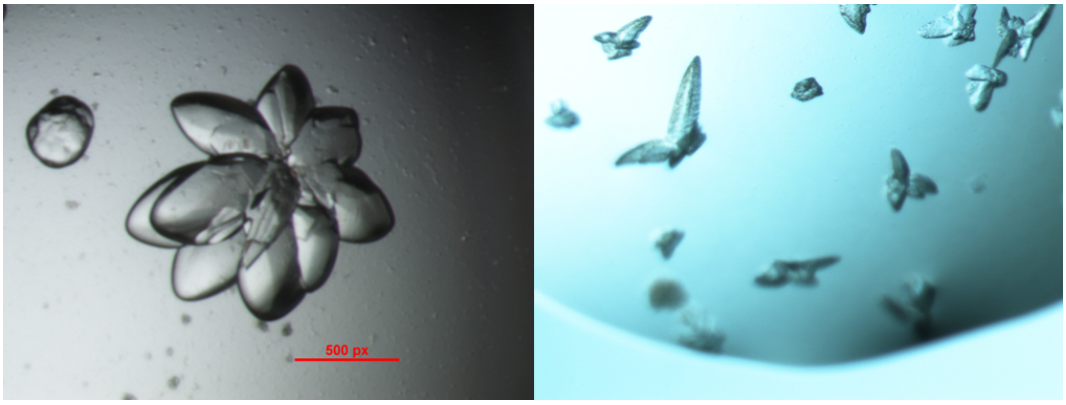

Figure 5.2 Crystals of the calcium-free derCD23/Fcε3-4 complex.
Left: crystals grown in 0.2 M sodium acetate trihydrate, 0.1 M Tris pH 8.5, 15% PEG 4000; the longest dimension of a separated single crystal is 400 μm . Right: crystals grown in 0.1 M Tris pH 8.0, 8% PEG 8000; the longest dimension of a separated single crystal is 300 μm.

5.2.2 Crystallisation of calcium-bound derCD23/Fcε3-4 complex

Initially, crystals obtained in the first condition (see section 5.2.1) were used for soaking with 10 mM $CaCl_2$. However, the best crystal diffracted only to about 4 Å resolution. Therefore co-crystallisation with a high concentration of calcium was also performed to obtain the calcium-bound complex. The complex of derCD23 with Fcε3-4 (0.44 mM and 0.22 mM in 10 mM Tris pH 7.5, 20 mM NaCl, 0.05% sodium azide, 4 mM $CaCl_2$) was mixed 1:1 with 0.2 M sodium acetate trihydrate, 0.1 M Tris pH 8.5, 16% PEG 4000 and 10 mM $CaCl_2$ with micro-seeding at 18°C. Crystals appeared after 8 days (Figure 5.3), and were flash-frozen in liquid nitrogen using 25% glycerol, 0.1 mM Tris pH 7.5, 16% PEG 4000, 0.2 M sodium acetate trihydrate and 15 mM $CaCl_2$ as cryoprotectant.

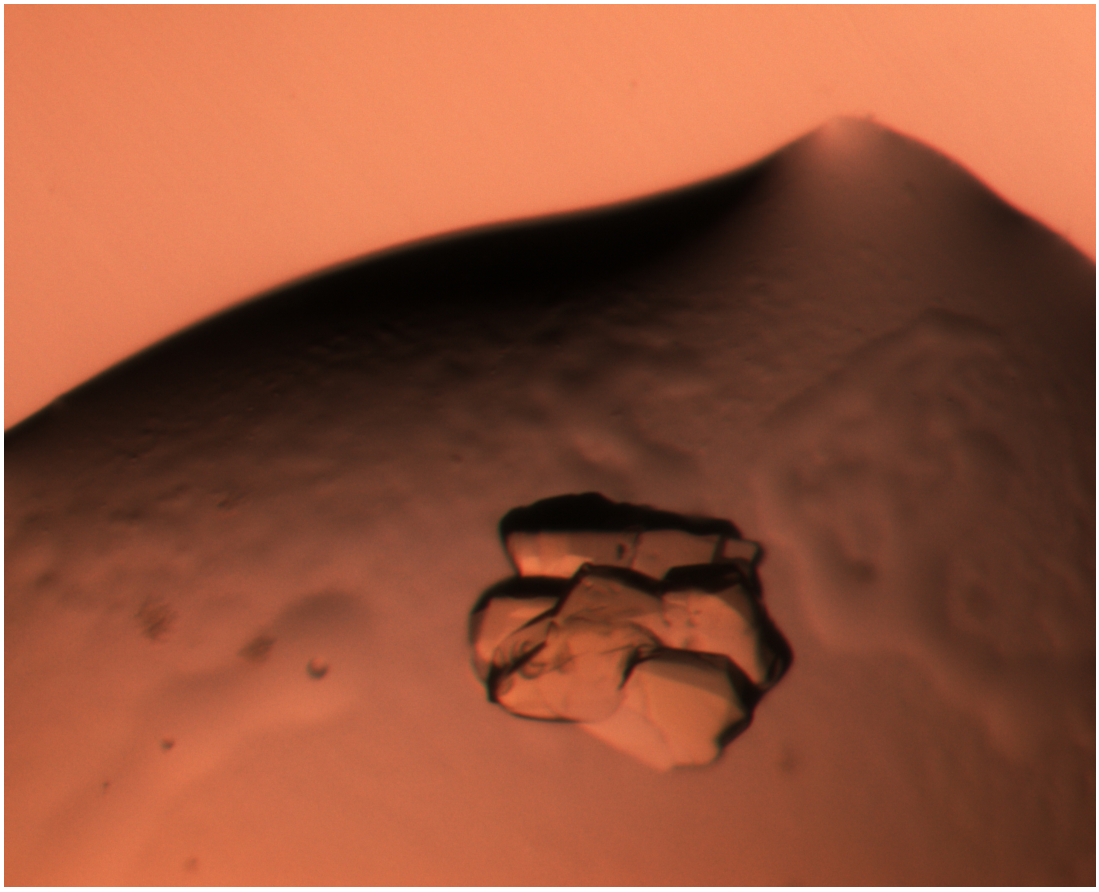

Figure 5.3 Crystals of the calcium-bound derCD23/Fcε3-4 complex.
The longest dimension of a separated single crystal is 300 μm.

5.3 Data collection and processing

5.3.1 Data collection and processing

Data from all crystals were collected at the Diamond Synchrotron using a Pilatus 2M detector and radiation of wavelength λ= 0.9173 Å. The dataset for calcium-bound derCD23/Fcε3-4 with the highest resolution diffraction was used, and a summary of collection and processing of the derCD23/Fcε3-4 complex data is shown in Table 5.1.

Space group	$P2_12_12_1$
Unit-cell parameters (Å,degrees)	a = 62.83 α = 90 b = 110.13 β = 90 c = 367.41 γ = 90
Wavelength (Å)	0.9173
Resolution range (highest shell) (Å)	73.5-3.30 (3.48-3.30)
Number of unique reflections	33757
Redundancy	4.9
Completeness (%)	86.3 (84.0)
I/σ (I)	5.1 (1.4)
R_{pim} (%)	8.9 (50.1)

Table 5.1 Data collection and processing statistics of derCD23/Fcε3-4 (Ca^{2+}-bound). Values in parentheses are for the highest resolution shell.
$R_{pim} = \Sigma_{refl}(1/(n_{refl}-1))\Sigma_i|I_i - I_{aver}|/\Sigma_{refl}\Sigma_i I_i$, where n_{refl} is the number of observations of reflection

5.3.2 Determination of space group and number of molecules in the asymmetric unit

The space group ($P2_12_12_1$) is the same, and cell parameters (a = 62.83Å, b = 110.13Å, c = 367.41Å, α = β = γ = 90°) are similar to the previously solved calcium-free derCD23/Fcε3-4 structure (Dhaliwal *et al.*, 2012). The Matthews coefficient calculation

indicated the presence of three complexes (six derCD23 molecules and three Fcε3-4 molecules) per asymmetric unit (Matthews coefficient 2.55$Å^3Da^{-1}$, 51.8% solvent).

5.4 Structure solution and refinement

5.4.1 Molecular replacement solution

The structure of calcium-bound derCD23/Fcε3-4 was solved by molecular replacement using PHASER with the previously solved structure of calcium-free derCD23/Fcε3-4 (PDB code 4EZM) as the search model.

5.4.2 Model building and refinement

Manual model building was carried out with COOT, coupled with refinement using REFMAC5 and PHENIX. The progression of the refinement was monitored using R factors (R_{work} and R_{free}), and TLS refinement was implemented using each of 12 chains as a group. The 12 chains are defined by letters as follows: chains A-F within the three Fcε3-4 molecules, and chains G-L for the six derCD23 molecules. The three complexes thus consist of A, B, G and H; C, D, I and J; and E, F, K and L chains. Local NCS restraints and isotropic B-factor refinement were used. Protein atoms and carbohydrate were modeled first. In the last stage, six calcium atoms were modeled, and no waters were added into the structure. Positive difference density in "site 2" of derCD23 disappeared when calcium was modeled (shown for chain G in Figure 5.4). B-factor and the final refinement statistics are presented in Table 5.2.

Some parts of the structure are poorly defined due to the low resolution. Electron density was observed for protein residues 335-386, and 389-545 of chain A; residues 336-361, and 365-545 of chain B; residues 336-366, 372-420, and 429-545 of chain C; residues 335-364, 368-386, 390-453, 459-461, 464-480, 484-524, 527-541 of chain D; residues 335-366, 371-418, 423-428, 431-445, 450-478, 481-509, 520-540 of chain E; 336-362, 365-445, 451-539 of chain F; residues 158-292 of chain G; residues 158-290 of chain H; residues 158-291 of chain I; residues 158-292 of chain J; residues 157-

291of chain K; residues 158-293 of chain L. N-linked carbohydrate chains with five sugar units ($(NAG)_2$-$(MAN)_3$) at N394 are present on five heavy chains, and seven sugar units ($(NAG)_2$-)$MAN)_5$) are visible on chain C. Details of the protein residues, calcium ions and carbohydrate units are shown in Table 5.3.

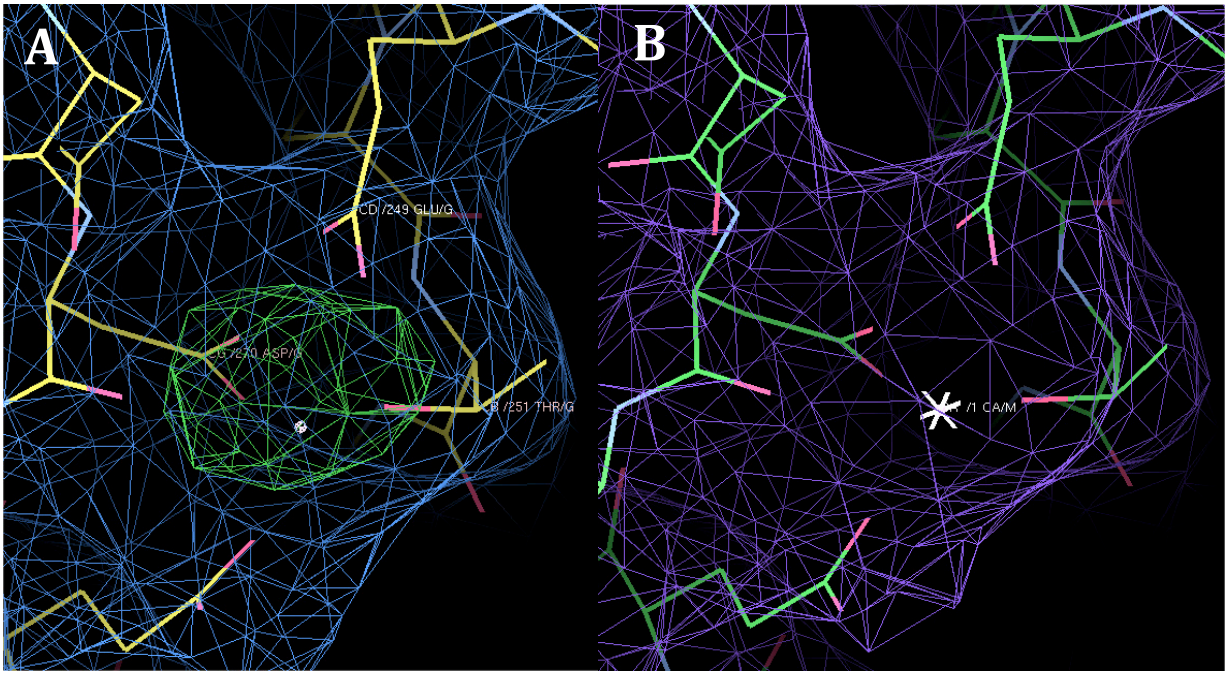

Figure 5.4 Electron density maps in the region of the calcium binding "site 2".
The positive difference map (green in Figure A) disappeared when calcium (white cross in Figure B) was modeled in the calcium binding "site 2".
A: No calcium was modeled to calcium "site 2" of chain G. 2Fo-Fc (1σ level) electron density maps are shown in blue, Fo-Fc (3σ level) electron density maps are shown in red (negative but not visible) and green (positive).
B: Calcium was modeled to calcium "site 2" of chain G. 2Fo-Fc (1σ level) electron density maps are shown in purple, and Fo-Fc (3σ level) electron density maps are shown in red (negative but not visible) and green (positive but not visible).

Number of:	
Protein atoms	15823
Carbohydrate atoms	388
Calcium ions	6
Average B factors ($Å^2$):	
Protein	150.0
Carbohydrate	142.6
Protein (chain A)	124.4
Protein (chain B)	141.5
Protein (chain C)	133.0
Protein (chain D)	151.9
Protein (chain E)	175.2
Protein (chain F)	165.4
Protein (chain G)	161.6
Protein (chain H)	134.2
Protein (chain I)	143.4
Protein (chain J)	128.8
Protein (chain K)	218.0
Protein (chain L)	131.0
R_{work}/R_{free}(%)	27.8/30.7
r.m.s. deviations	bond lengths = 0.015 Å bond angles = 1.775°

Table 5.2 Statistics of the refinement process for calcium-bound derCD23/Fcε3-4 structure.

$R_{work} = \Sigma||F_{obs}| - |F_{calc}||/\Sigma|F_{obs}|$, where F_{obs} and F_{calc} are the observed and calculated structure factor amplitudes.

$R_{free} = \Sigma_t||F_{obs}| - |F_{calc}||/\Sigma_t|F_{obs}|$, where F_{obs} and F_{calc} are the observed and calculated structure factor amplitudes, and $_t$ is the test set of data omitted from refinement (5% in this case).

Chain name	Content
Chain A:	Fcε3-4 heavy chain: residues 335-386, 389-545; carbohydrate: $((NAG)_2$-$(MAN)_3)$
Chain B	Fcε3-4 heavy chain: residues 336-361, 365-545; carbohydrate: $((NAG)_2$-$(MAN)_3)$
Chain C	Fcε3-4 heavy chain: residues 336-366, 372-420, 429-545; carbohydrate: $((NAG)_2$-$(MAN)_5)$
Chain D	Fcε3-4 heavy chain: residues 335-364, 368-386, 390-453, 459-461, 464-480, 484-524, 527-541; carbohydrate: $((NAG)_2$-$(MAN)_3)$
Chain E	Fcε3-4 heavy chain: residues 335-366, 371-418, 423-428, 431-445, 450-478, 481-509, 520-540; carbohydrate: $((NAG)_2$-$(MAN)_3)$
Chain F	Fcε3-4 heavy chain: 336-362, 365-445, 451-539; carbohydrate: $((NAG)_2$-$(MAN)_3)$
Chain G	derCD23: residues 158-292; one calcium
Chain H	derCD23: residues 158-290; one calcium
Chain I	derCD23: residues 158-291; one calcium
Chain J	derCD23: residues 158-292; one calcium
Chain K	derCD23: residues 157-291; one calcium
Chain L	derCD23: residues 158-293; one calcium

Table 5.3 Protein residues of derCD23 and Fcε3-4, carbohydrate and calcium ions modelled into the structure.
Six derCD23 molecules and six heavy chains of three Fcε3-4 molecules (AB, CD, EF) formed six complex pairs (AG, BH, CI, DJ, EK, FL).

5.4.3 Validation

The refined structure was analysed with Molprobity as indicated in section 2.14. An analysis of the corresponding Ramachandran plot (Figure 5.5) showed that 99.4% of residues are in allowed regions of the plot.

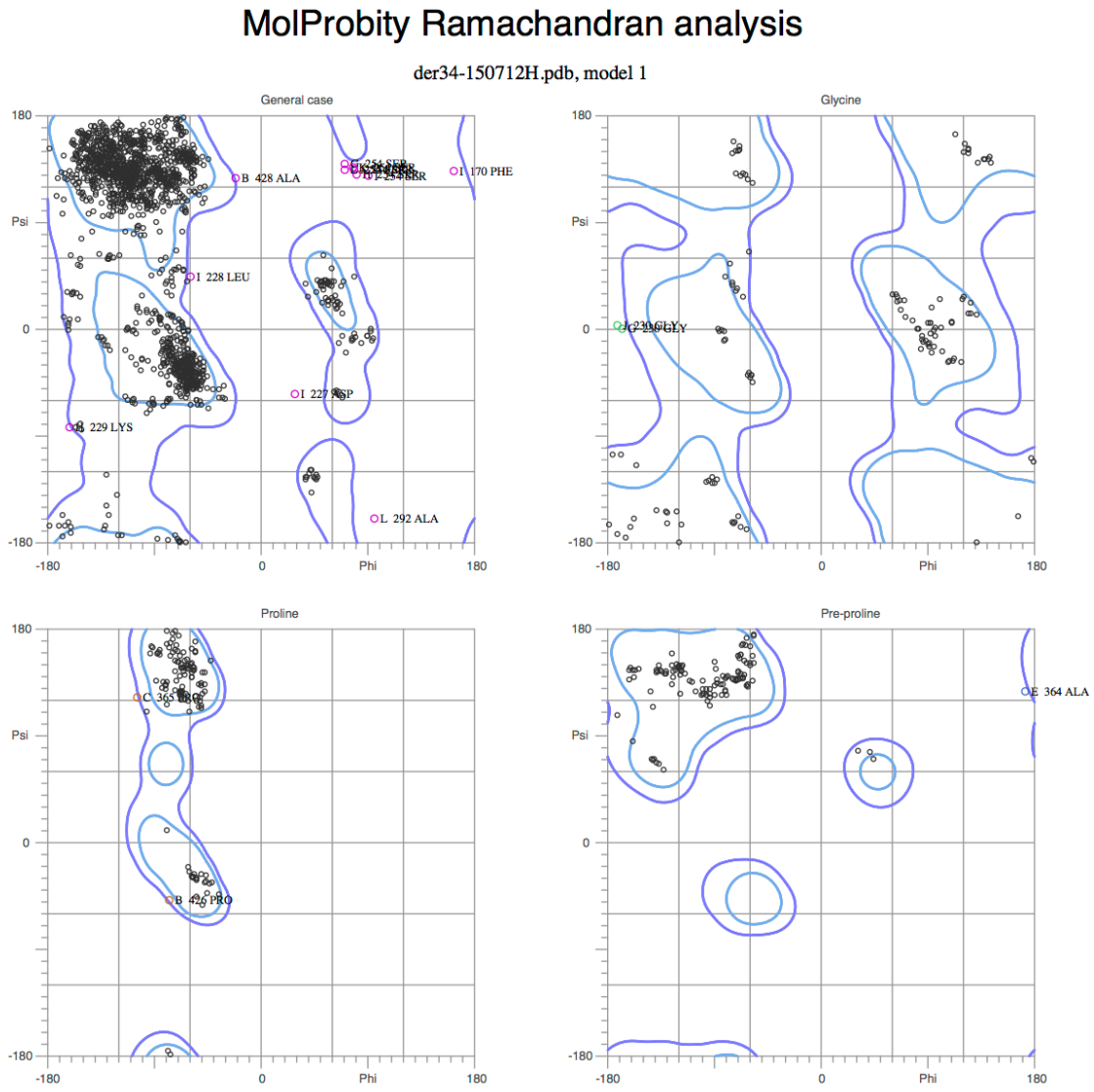

Figure 5.5 Ramachandran plots for the calcium-bound derCD23/Fcε3-4 structure, calculated with the Molprobity server.
From the top left: plot of φ and ψ angles for the general case, glycine, proline and pre-proline residues. 99.1% of residues, indicated by small black circles, are in allowed (dark blue) regions. 90.9% of residues are in the favoured (light blue) regions.

5.5 Overall structure of calcium-bound derCD23/Fcε3-4

As for the previously solved calcium-free derCD23/Fcε3-4 structure (Dhaliwal *et al*., 2012), three Fcε3-4 and six derCD23 molecules form 6 complex pairs in the asymmetric unit cell (Figure 5.6). All six derCD23 copies show calcium bound in "site 2", which affect interactions between derCD23 and Fcε3-4. However, the coordination of calcium is not shown clearly due to the limited resolution. Interpretable density is present for loop1 and loop 4 in all derCD23 molecules. The interface between chain D and chain J is the most clearly defined.

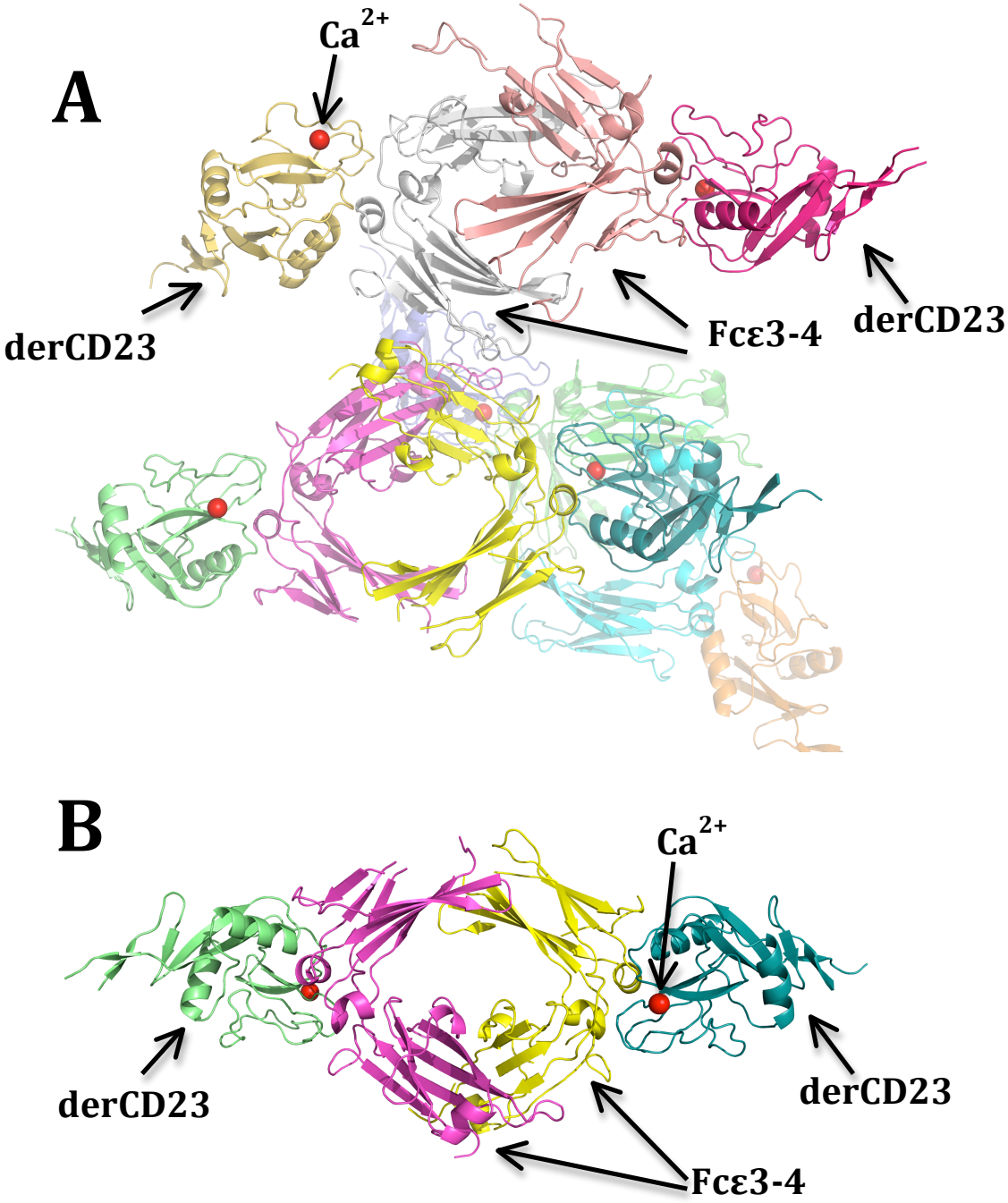

Figure 5.6 Cartoon representation of the Ca^{2+}-bound derCD23/Fcε3-4 structure.
A: showing all 12 chains of the 3 complexes, each with 2:1 derCD23: Fcε3-4. B: showing four chains of one complex with 2:1 derCD23: Fcε3-4.

The angle between the Cε3 and Cε4 domains remains the same in the six Fcε3-4 heavy chains of the Ca^{2+}-bound derCD23/Fcε3-4 structure (Figure 5.7 A), whereas slight

variations were observed in the Ca^{2+}-free derCD23/Fcε3-4 (Dhaliwal *et al.*, 2012). There are also no obvious differences between the six derCD23 head domains (Figure 5.7 B), which was also found in the Ca^{2+}-free derCD23/Fcε3-4.

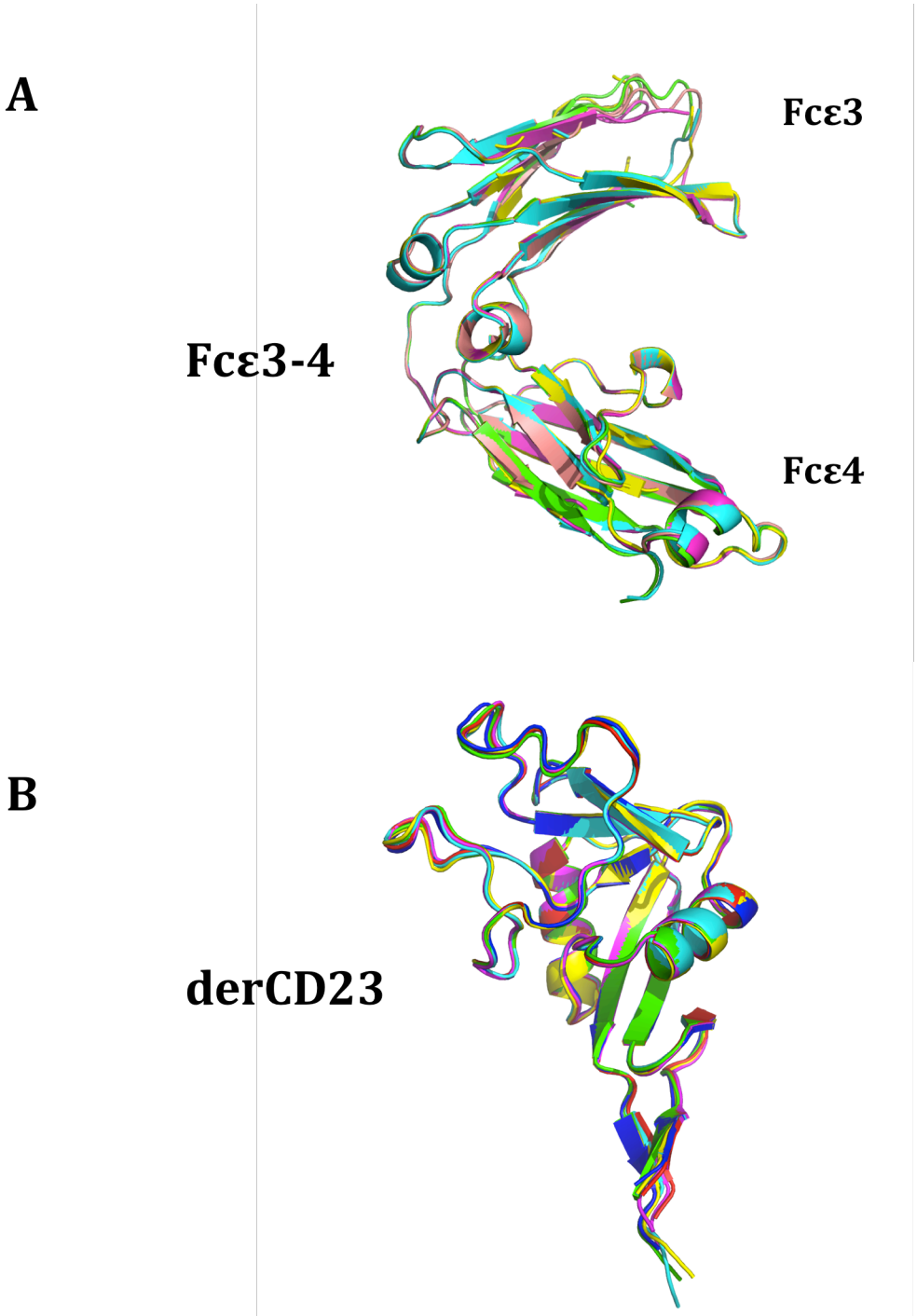

Figure 5.7 Comparison of derCD23 and Fcε3-4 in six complex pairs.
A: The six Fcε3-4 heavy chains were superposed on the Cε4 domains of Chain A, and show no variation in the relative positions of the Cε3 domains. B: The superposed six derCD23 molecules, showing virtually no structural variation.

5.6 Comparison of Ca^{2+}-bound and -free derCD23/Fcε3-4 structures

In the previously solved Ca^{2+}-free derCD23/Fcε3-4 structure (Dhaliwal *et al*., 2012), derCD23 contacts Fcε3-4 using three salt bridges (D409-R188, E412-R188 and E412-R224), a potential fourth salt bridge (E414-H186), four additional hydrogen bonds (R376-Y189, D409-Y189 and R440-S254 main chain and side chain interaction), and a few well-defined van der Waals interactions in all six interfaces. The buried surface area for each interaction between derCD23 and Fcε3-4 ranges from 860-920 $Å^2$ for the six heavy-chain/derCD23 interactions.

To investigate the role calcium plays in IgE binding, the Ca^{2+}-bound complex was compared with the Ca^{2+}-free derCD23/Fcε3-4 structure. The two derCD23/Fcε3-4 complexes differ in two main respects according to a comparison made by superimposing all Cα atoms. Firstly, electron density attributable to Ca^{2+} is present in all 6 molecules of derCD23 at "site 2" in the Ca^{2+}-bound derCD23/Fcε3-4 structure. They have similar arrangement of calcium site ligands in all derCD23 molecules. Secondly, large structural differences are observed in loop 4 of derCD23 that is involved in IgE binding. All 6 copies of loop 4 in the Ca^{2+}-bound complex can be seen clearly, whereas 5 out of 6 copies of loop 4 in the Ca^{2+}-free structure are disordered. The ordered loop 4 is seen only in the chain F/chain L interface of the Ca^{2+}-free complex. New interactions between derCD23 and Fcε3-4 are observed by comparison of these two complexes.

The most clearly defined interface between chain D and chain J in the Ca^{2+}-bound complex is compared with the interface between chain D and chain J in the Ca^{2+}-free complex, which has a disordered loop 4; it is also compared with the interface between chain F and chain L in the Ca^{2+}-free complex, which has an ordered loop 4 (Table 5.4, Figure 5.9). Two new salt bridges between derCD23 and Fcε3-4, D227-R440 and D258-R440, are observed after calcium binding. The positively charged R440 in IgE protrudes into a deep pocket (Figure 5.9 and 5.10) that is mainly formed by D258 and D227 in derCD23. Electron density for these three residues is clearly observed at 1σ level in this 3.3 Å resolution structure (Figure 5.11). Other interactions between

derCD23 and Fcε3-4 are very similar compared with the Ca^{2+}-free derCD23/Fcε3-4 complex. Salt bridges and hydrogen bonds at the interface of chain D and chain J in the Ca^{2+}-bound complex are shown in Figure 5.9. Most of the well-defined van der Waals interactions in the Ca^{2+}-free complex (Dhaliwal *et al*., 2012) are also present in this Ca^{2+}-bound complex.

The buried surface area for each interaction between derCD23 and Fcε3-4 ranges from 800-860 $Å^2$ for the six interfaces (see chapter 2 for the tool used for calculation). This is less than the range of 860-920 $Å^2$ in the calcium-free derCD23/Fcε3-4 structure (Dhaliwal *et al*., 2012). Because the interface between chain D and chain J is more clearly defined in the Ca^{2+}-bound complex, this pair was used to measure the contact area contributed by Cε3, Cε4 and the linker region (residues 437-440) separately. The Cε3 contributes 66% to the contact area, while Cε4 and linker region contribute 13% and 21% respectively. The calcium-free derCD23/Fcε3-4 structure shows similar contribution of Cε3 (63%), Cε4 (12%) and the linker region (25%) to the contact area.

Taken together, these results show that upon calcium binding loop 4 is stabilised and contributes new interactions between derCD23 and Fcε3-4. Comparison of uncomplexed derCD23 structures also reveals that loop 4 is locked in a particular position after calcium binding, as described chapter 3.

	Chain D and Chain J (Ca^{2+}) interface	Chain D and Chain J (No Ca^{2+}) interface	Chain F and Chain L (No Ca^{2+}) interface
Salt bridges	D409-R188	D409-R188	D409-R188
	E412-R188	E412-R188	E412-R188
	E412-R224	E412-R224	E412-R224
	E414-H186	E414-H186	E414-H186
	R440-D227	-	-
	R440-D258	-	-
Additional hydrogen bonds	R376-Y189	R376-Y189	R376-Y189
	D409-Y189	D409-Y189	D409-Y189
	S437-C273	-	S437-C273
	R440-Q255	-	R440-Q255
	-	R440-S254 (two)	R440-S254 (two)

Table 5.4 Interactions between derCD23 and Fcε3-4 in Ca^{2+}-bound and -free derCD23/Fcε3-4 structures.

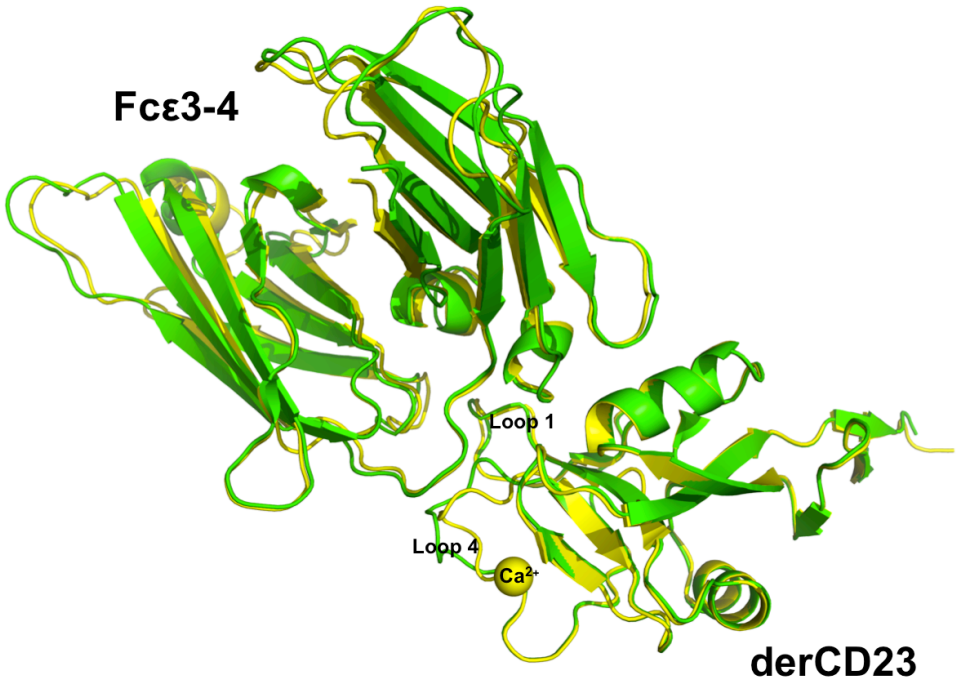

Figure 5.8 A cartoon diagram overlay of Ca^{2+}-free and Ca^{2+}-bound derCD23/Fcε3-4 complexes.
Ca^{2+}-bound structure (Chain D and Chain J) is shown in yellow, Ca^{2+}-free (Chain F and Chain L, Dhaliwal *et al*., 2012) is shown in green. Conformational changes can be seen in loop 4.

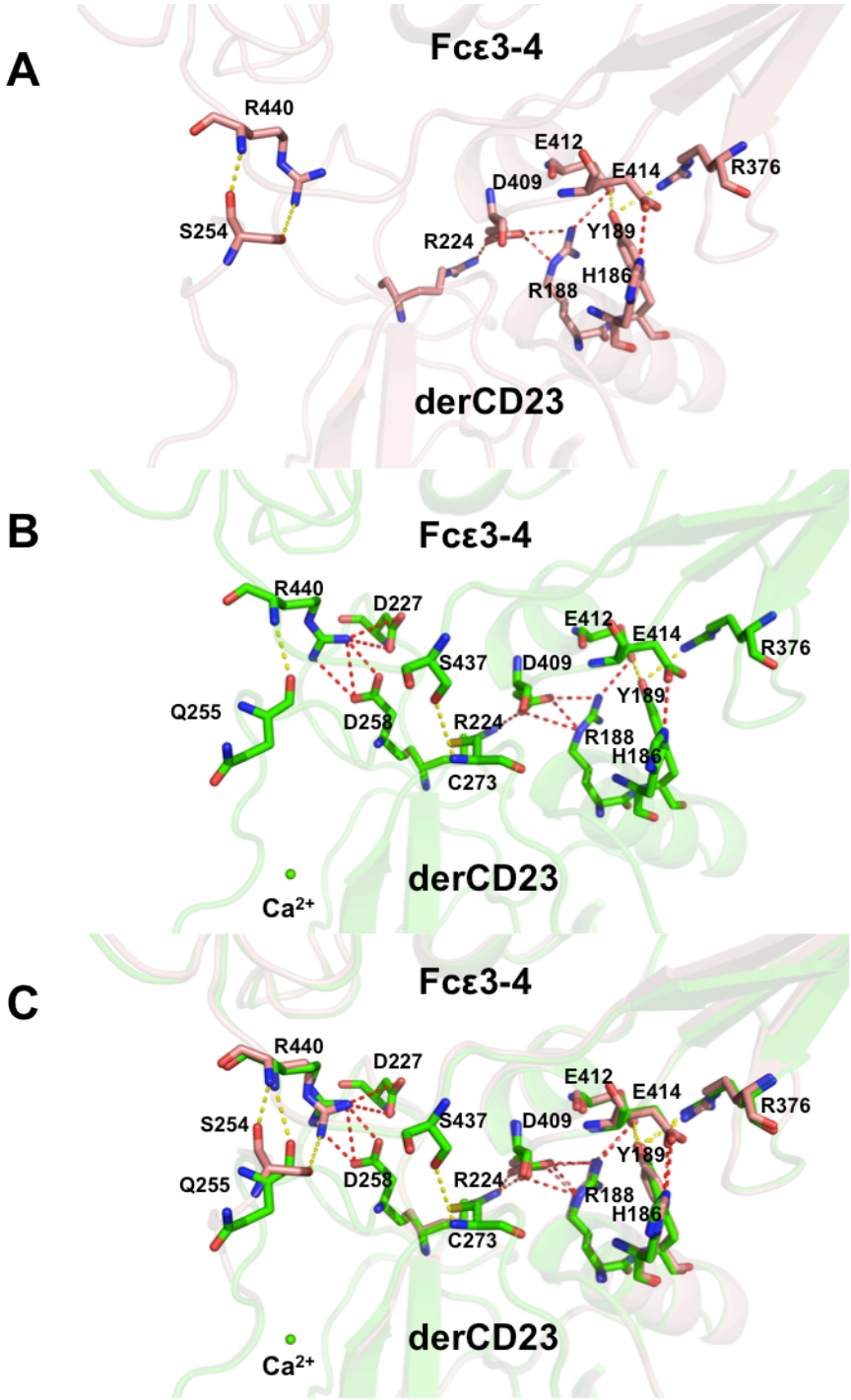

Figure 5.9 Interfaces of Ca^{2+}-free (pink) and Ca^{2+}-bound (green) derCD23/Fcε3-4 structures for chains D and J of the complexes.
A: Interface of Ca^{2+}-free derCD23/Fcε3-4 structure (pink). B: Interface of Ca^{2+}-bound (green sphere) derCD23/Fcε3-4 structure (green). C: Superimposition of Ca^{2+}-bound (green) and Ca^{2+}-free (pink) derCD23/Fcε3-4 structures. The side chains of residues in the interface are shown as sticks. The hydrogen bonds associated with salt bridges are shown as red dashes, additional hydrogen bonds are show as yellow dashes.

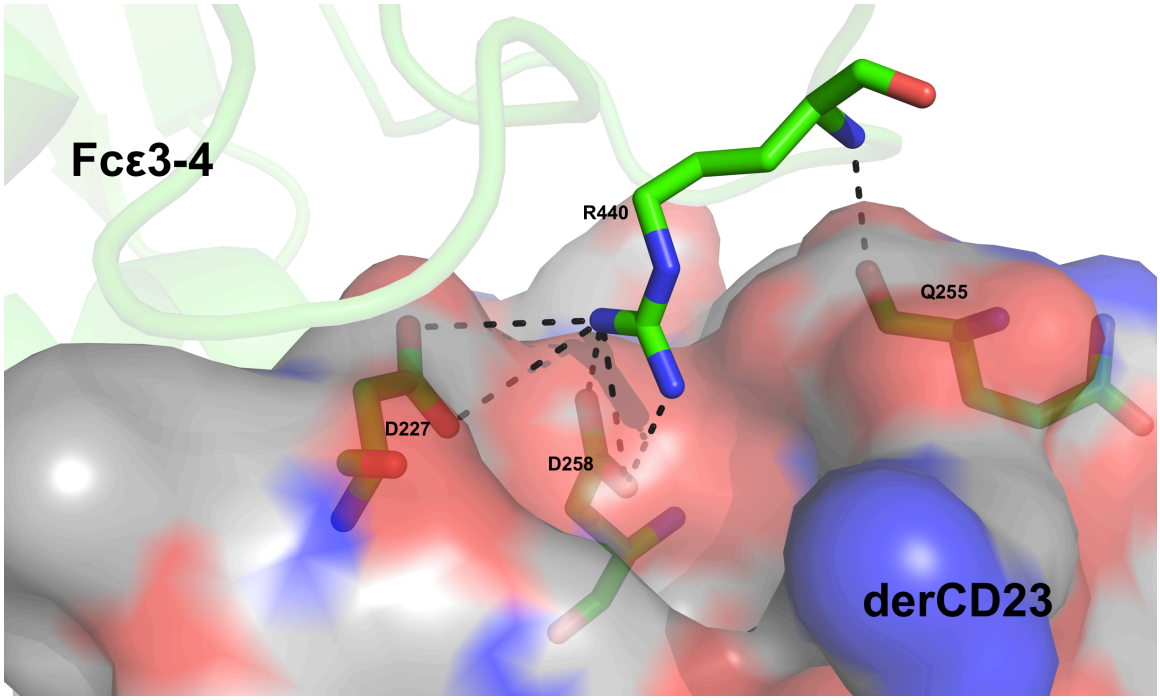

Figure 5.10 The positively charged R440 in IgE protrudes into a deep pocket that is mainly formed by D258 and D227 in derCD23.
The Ca^{2+} bound structure of derCD23 (surface, chain J) and Fcε3-4 (cartoon, chain D) complex shows R440 in IgE pointing into a negative cavity in derCD23 formed by D227 and D258. R440 interacts with 3 residues in derCD23 by forming two salt bridges and a hydrogen bond.

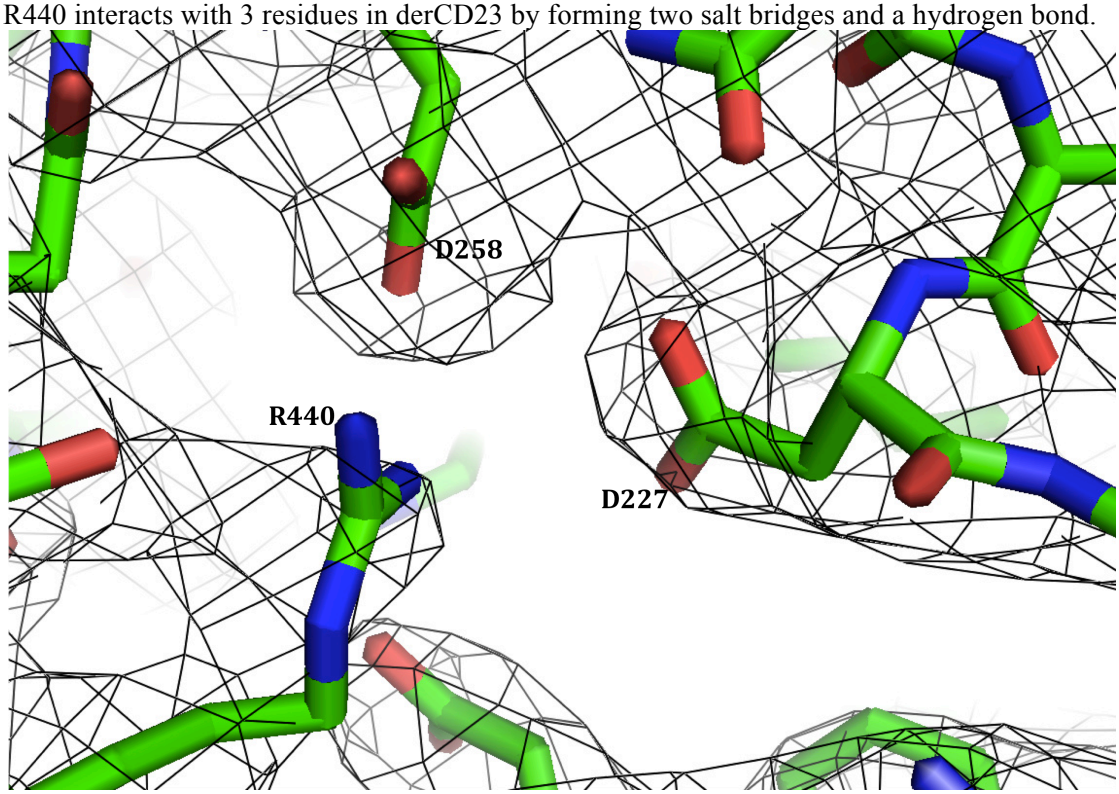

Figure 5.11 Electron density map showing R440 of IgE (chain D), D227 and D258 of derCD23 (chain J).
The 2Fo-Fc map is contoured at 1.0 σ. This is the new salt bridge formed as a result of ordering loop 4 in derCD23 by calcium binding.

5.7 Summary and discussion

IgE is the central player in allergic diseases (Gould and Sutton, 2008), and the interaction between CD23 and IgE may be a target for drug design. This chapter describes the crystallisation and structure determination by X-ray crystallography of the calcium-bound derCD23/Fcε3-4 complex to 3.3 Å resolution. The calcium-free derCD23/Fcε3-4 complex, previously solved at 3.1 Å resolution (Dhaliwal *et al*., 2012), is used for comparison with this calcium-bound complex. Structural comparison reveals the role calcium plays in CD23 binding to IgE.

As a member of the CTLD superfamily, there are two putative calcium binding sites in CD23 according to sequence alignment. In the 2 Å resolution calcium-bound derCD23 structure (described in chapter 3), three residues (E249, T251 and D270) in calcium binding "site 2" and three water molecules are involved in the binding to Ca^{2+} (Figure 3.13). No calcium is bound to "site 1". The calcium-bound derCD23/Fcε3-4 structure confirms that calcium is bound to "site 2" in derCD23, despite not showing the coordination clearly due to the limited resolution. There is no evidence for a difference between the calcium co-ordination in the free and the IgE-bound derCD23. Most members of the CTLD superfamily possess a carbohydrate-binding activity that depends strictly on the binding of calcium (Ng *et al*., 1998). CD23 may have lost the function to bind carbohydrate, but calcium increases CD23's binding affinity to IgE 7-fold as determined by SPR (Hibbert *et al*., 2005). However, this calcium-bound complex indicates that calcium is not involved in IgE binding directly. What then is the role calcium plays in CD23 binding to IgE?

In chapter 3, structural comparison of calcium-bound and -free derCD23 structures shows structural changes of loop 4 and loop 1 upon calcium binding to "site 2" in derCD23. In this chapter, this calcium-bound complex shows direct evidence of calcium-related structural changes in CD23 binding to IgE (Figure 5.8). Loop 4 of derCD23 is ordered in all six copies of derCD23 of the calcium-bound complex, whereas it is disordered in five out of six copies of the previously solved calcium-free complex (Dhaliwal *et al*., 2012). This indicates that the role calcium plays in IgE

binding is to stabilise loop 4. This is consistent with the comparison of calcium-bound and -free derCD23 structures. In addition, loop 4 of derCD23 in the calcium-bound complex with Fcε3-4 adopts a stabilised conformation, that although different to all the other observed conformations, is more like the conformation in the calcium-bound derCD23 structure alone than in the calcium-free structures. In contrast, the calcium-free complex has a disordered loop 4 in 5 out of 6 derCD23 molecules, and the calcium-free derCD23 structure has two conformations of loop 4 (Figure 5.12).

Superposition of the six heavy chains of Fcε3-4 in the calcium-bound derCD23/Fcε3-4 structure indicates that the angle between the Cε3 and Cε4 domains remains the same (Section 5.5), whereas slight variations are observed in the Ca^{2+}-free derCD23/Fcε3-4 (Dhaliwal *et al*., 2012). Thus, calcium bound to derCD23/Fcε3-4 may also stabilise the angle between the Cε3 and Cε4 domains.

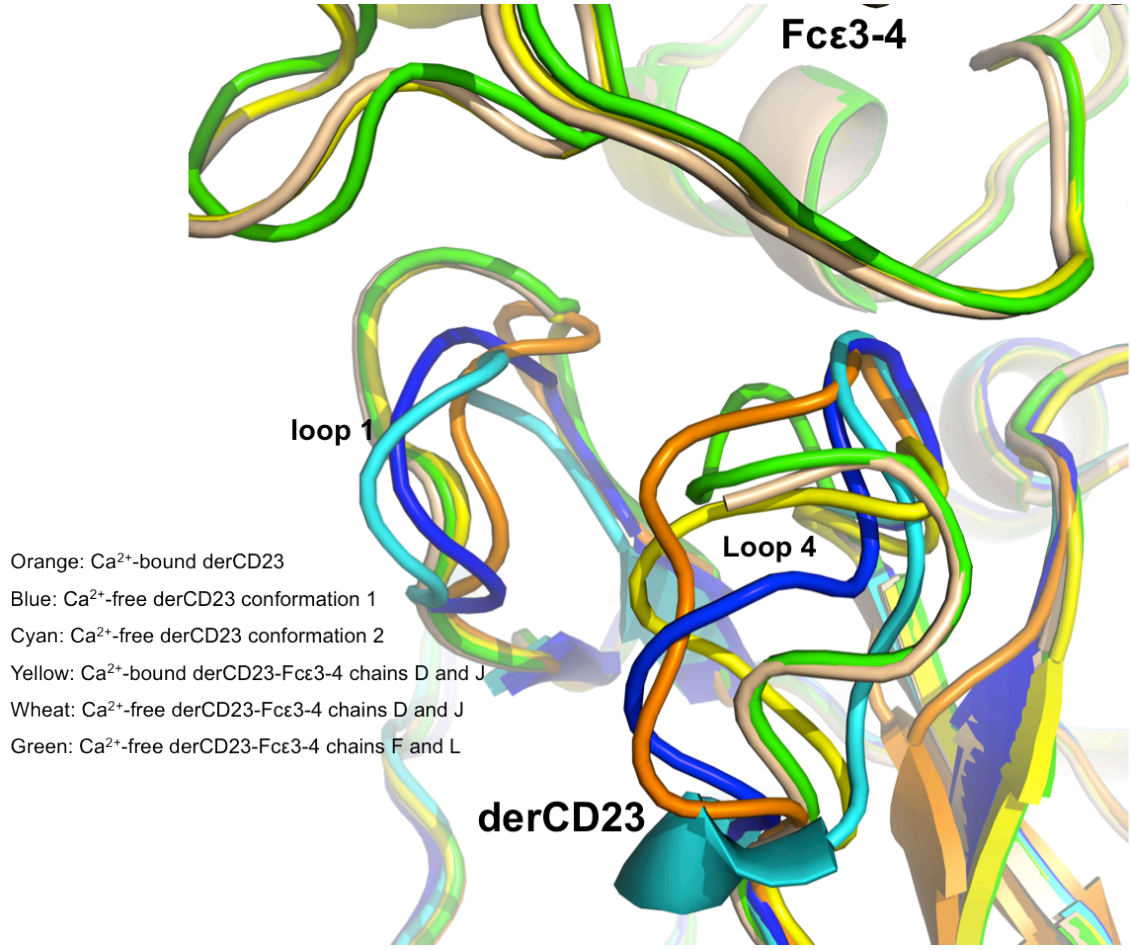

Figure 5.12 Comparison of Ca^{2+}-bound and -free derCD23 and derCD23/Fcε3-4 structures.
The stabilised loop 4 of derCD23 in the calcium-bound complex adopts a conformation that is more like the conformation in the calcium-bound derCD23 structure alone than the calcium-free structures. Both the calcium-free complex and calcium-free derCD23 structures have a more flexible loop 4, as the calcium-free complex has a disordered loop 4 in 5 out of 6 derCD23 molecules and the calcium-free derCD23 structure has two conformations of loop 4.

Importantly, the calcium-bound complex also shows new interactions between Fcε3-4 and derCD23. R440 of IgE interacts with D258 and D227 of CD23 by forming two new salt bridges. In addition, different hydrogen bonds are observed between R440 of Fcε3-4 and loop 4 of derCD23 (Table 5.4, Figure 5.9). Other interactions between Fcε3-4 and derCD23 remain the same in the two complexes. Surprisingly, calcium-bound derCD23/Fcε3-4 has a smaller buried surface area than the calcium-free complex (Section 5.6). D258, which is involved in the additional salt bridge in the calcium-bound complex, is the only conserved residue of "site 1" in human CD23 according to sequence alignment, as described in chapter 3. However, no calcium binds to "site 1" in CD23. Taken together, it appears that human CD23 lost the function to bind calcium in

"site 1", but evolved to bind protein (IgE) directly using "site 1" residue D258 when calcium is bound at "site 2".

In summary, the structure of the calcium-bound derCD23/Fcε3-4 complex reveals new protein-protein interactions, which explains the enhanced affinity in the presence of calcium. A comparison of the calcium-bound and -free derCD23, and the calcium-bound and -free derCD23/Fcε3-4 complex structures reveals the role calcium plays in CD23 binding to IgE. The implications of these structural data will be discussed in more detail in the general discussion (Chapter 7).

Chapter 6:
The complex of derCD23 and anti-CD23 Fab (IDEC152-Fab)

6.1 Introduction

CD23, the low-affinity receptor of IgE, mediates many IgE-related immune responses by regulating IgE synthesis and presenting allergen to the immune system. Thus, targeting CD23 is a promising candidate therapy for the treatment of allergic diseases. Anti-CD23 antibodies could be used, according to recent studies. IDEC152 (also known as Lumiliximab) is a primatized, IgG1, anti-CD23 monoclonal antibody. Results of a phase I clinical trial with IDEC152 indicates this antibody is well tolerated and causes sustained and dose-dependent decreases of serum IgE level (Rosenwasser *et al*., 2003). Subsequently, IDEC152 was reported to be possibly involved in modulating antigen presenting cells and decreasing T_H2-type immune responses (Poole *et al*., 2005). However, the mechanism of IDEC152 activity in allergic disease is not clear.

Structural study of the complex of derCD23 and IDEC152 may reveal the mechanism of action of this antibody. In addition, determination of the derCD23/IDEC152 structure may also be helpful for developing new small-molecule CD23 inhibitors. This chapter describes digestion of IDEC152 IgG antibody, purification of the Fab and crystallisation of the complex of derCD23 and IDEC152-Fab. IDEC152 was donated by IDEC Pharmaceuticals, San Diego, CA, and the purification protocol of IDEC152-Fab was provided by Dr. Rebecca Beavil and Dr. Stella Fabiane (Section 2.9.2).

6.2 Digestion of IDEC152

Although 10 mg/ml IgG1 was expected to be digested at 37°C by papain in 4 hours, it was found that IDEC152 was not digested completely even when incubated overnight (Figure 6.1). Overnight digestion of IDEC152 was therefore used to make IDEC152-Fab.

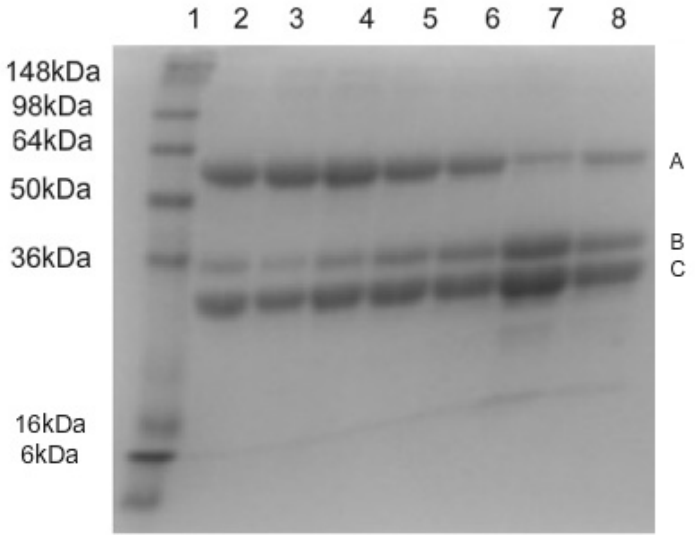

Figure 6.1 15% reducing SDS-PAGE of digested IDEC152 with time-scale.
Lane 1-8: marker; 30 minutes digestion; 1 hour digestion; 2 hours digestion; 4 hours digestion; 6 hours digestion; overnight digestion; 8 hours digestion. A: complete heavy chain; B: Fc heavy chain; C: Fab heavy chain and Fab light chain.

6.3 Purification of IDEC152-Fab

IDEC152-Fab was purified by ion exchange chromatography with the TSKgel SP-5PW glass column (Section 2.9.2). The purification profile of IDEC152-Fab is shown in Figure 6.2. Non-reducing SDS-PAGE indicates that the molecular weight of IDEC152-Fab is about 50 kDa as expected (Figure 6.3).

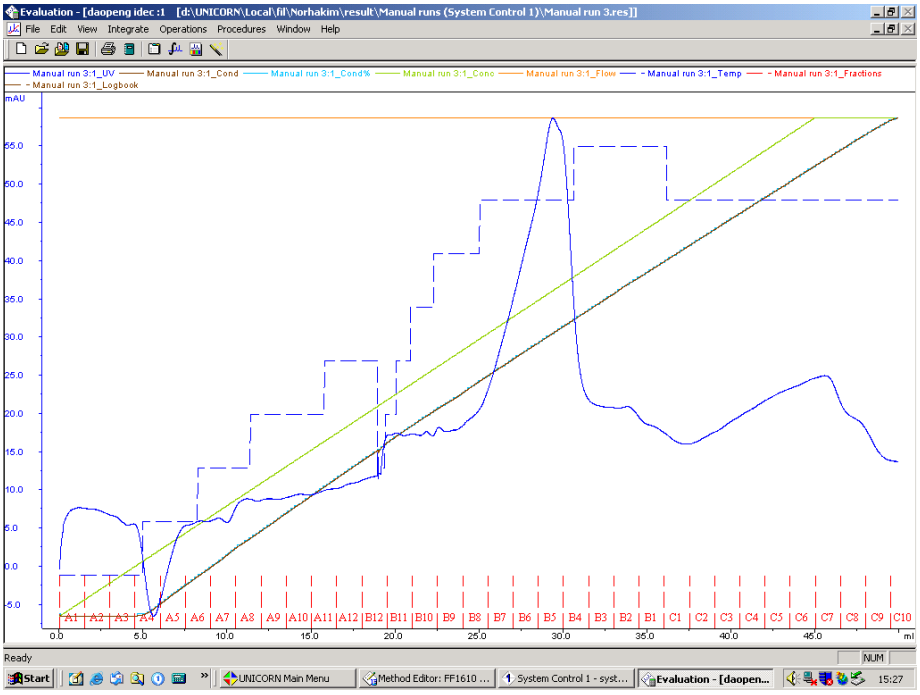

Figure 6.2 Purification profile of IDEC152-Fab by ion exchange column.
Fractions of B10-C6 were collected to run non-reduced SDS-PAGE.
Blue curve: UV; Dotted blue curve: temperature; Brown curve: conductivity; Green curve: concentration of buffer B. (see section 2.9.2).

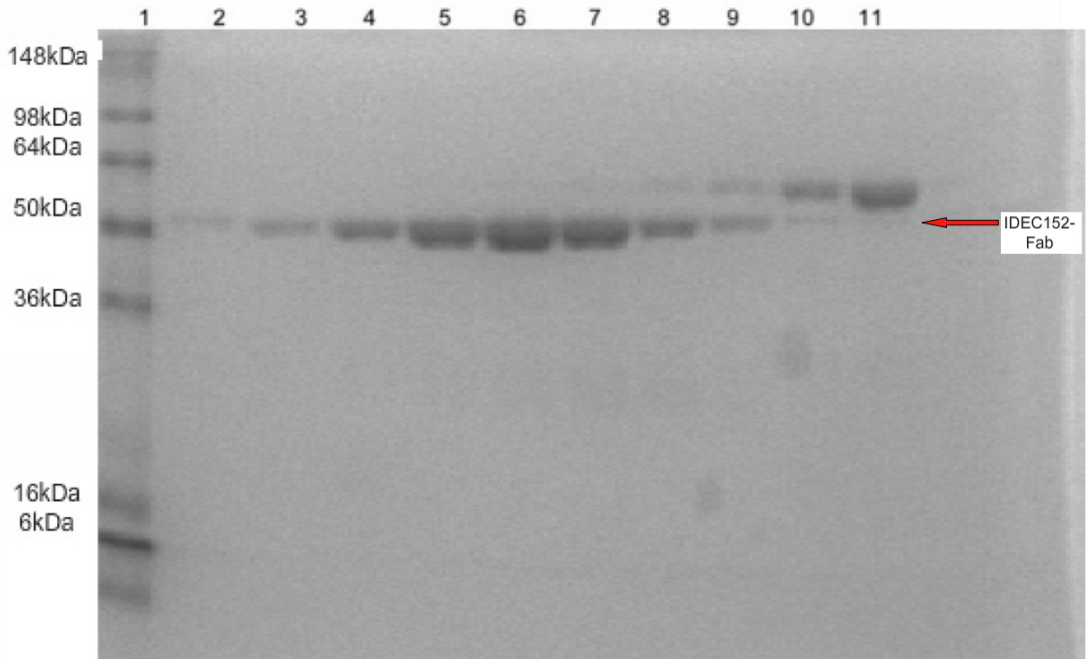

Figure 6.3 15% non-reducing SDS-PAGE indicates that the molecular weight of IDEC152-Fab is about 50 kDa.
Lane 1: marker; Lane 2-8: fractions B10-B4; Lane 9: fractions B3-B1; Lane 10: fractions C1-C3; Lane 11: C4-C6.

6.4 Initial crystallisation trials for the complex of derCD23 and IDEC152-Fab

Initially, 1.75 µl derCD23 at 20 mg/ml and 23.25 µl IDEC152-Fab at 4.37 mg/ml were mixed together at one to one ratio for crystallisation. Crystals of derCD23/IDEC152-Fab complex were observed in 0.1 M Tris pH 8.0, 2.0 M ammonium sulfate after crystal screening at 18°C by the sitting drop vapour diffusion method (Figure 6.4). Optimization of crystallisation conditions was carried out by the micro-seeding method. Single crystals of the complex were obtained (Figure 6.5), which diffracted to about 3.5 Å resolution at the Diamond Synchrotron.

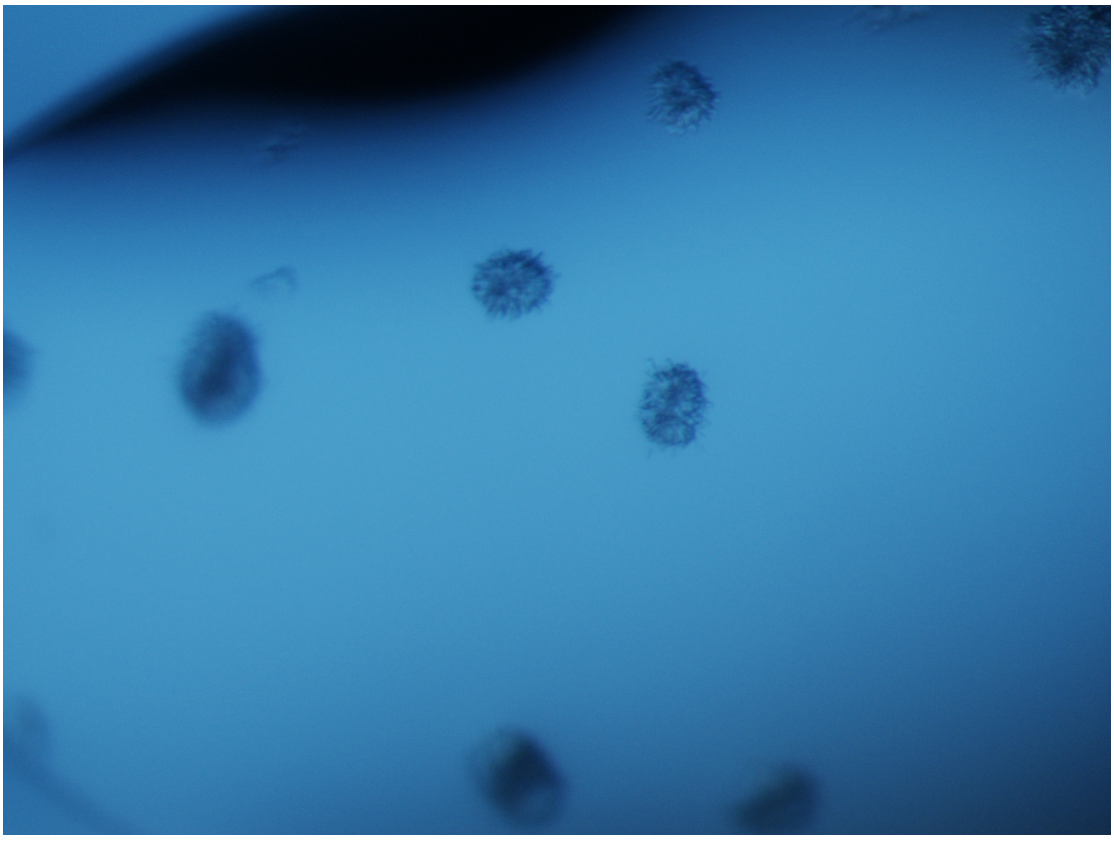

Figure 6.4 Crystals of derCD23/IDEC152-Fab complex.
Crystals of derCD23/IDEC152-Fab complex in 0.1 M Tris pH 8.0, 2.0 M ammonium sulfate after screening. The longest dimension of the crystal clusters is 100 µm.

Figure 6.5 Crystals of derCD23/IDEC152-Fab complex.
Crystals of derCD23/IDEC152-Fab complex in 0.1 M Tris pH 7.5, 1.8 M ammonium sulfate after optimization by the micro-seeding method. The longest dimension of the largest crystal is 150 μm.

6.5 Crystallisation of purified derCD23/IDEC152-Fab complex

6.5.1 Purification of derCD23/IDEC152-Fab complex

The molecular weight of the derCD23/IDEC152-Fab complex (66.5 kD) is much higher than derCD23 (16.5 kD), but is close to IDEC152-Fab (50 kD). So it is more difficult to separate derCD23/IDEC152-Fab from IDEC152-Fab than derCD23 using a size exclusion column. Thus, derCD23 and IDEC152-Fab were mixed at 1.2 to 1 ratio, to form the complex before purification. After purification by size exclusion chromatography, fractions of two peaks were collected and characterized by SDS-PAGE (Figure 6.6 and 6.7). Fractions of the complex were dialysed into the buffer (9 mM Tris pH 7.5, 13.2 mM sodium acetate pH 5.06, 137.6 mM NaCl and 0.08% NaN_3)

used for crystal screening. Then the purified complex was concentrated to the same concentration as used in initial crystal screening.

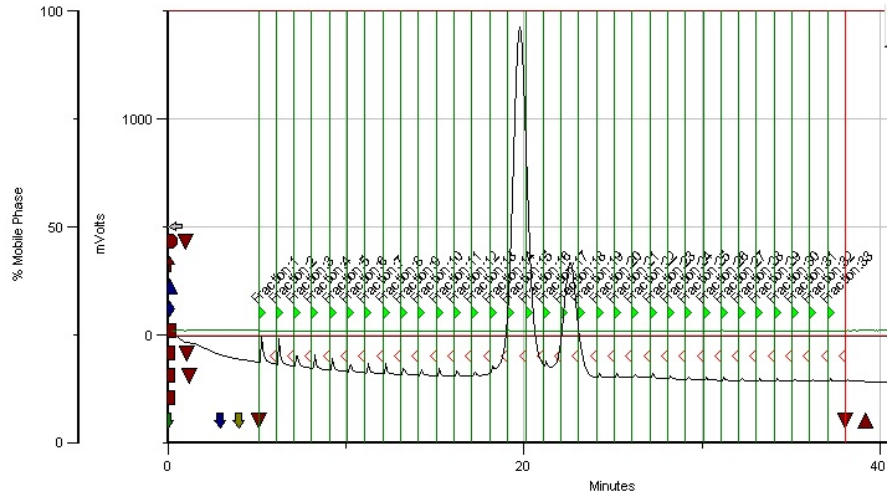

Figure 6.6 Purification profile of the derCD23/IDEC152-Fab complex by size exclusion column.
Fractions of 13-20 were collected to run non-reduced SDS-PAGE.

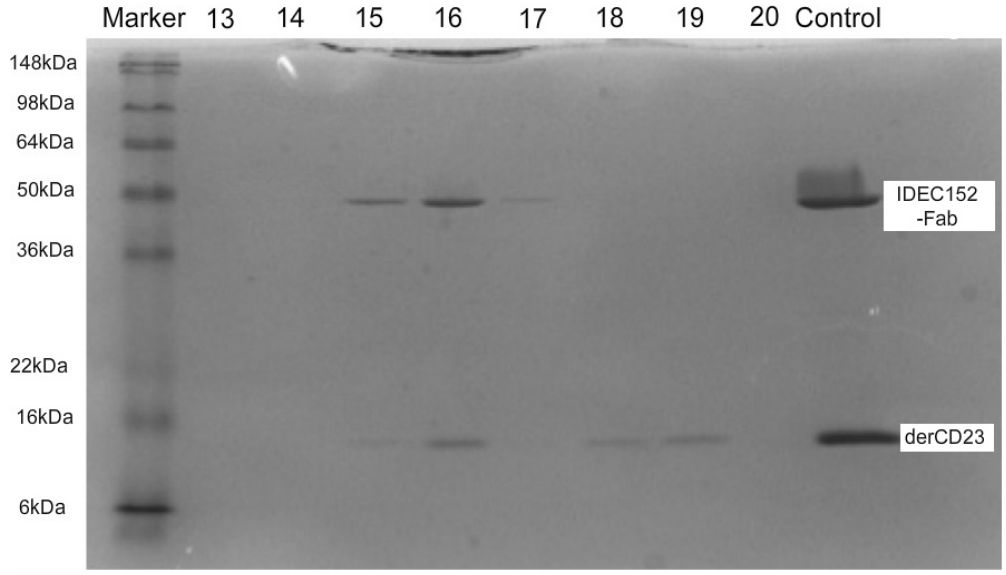

Figure 6.7 15% non-reducing SDS-PAGE indicates the first peak in Figure 6.6 (fractions 14-16) is the derCD23/IDEC152-Fab complex.
Lane 13-20: collected fractions (13-20) after size exclusion column; Control: the mixed derCD23 with IDEC152-Fab at 1.2 to 1 ratio.

6.5.2 Crystallisation of purified derCD23/IDEC152-Fab complex

The purified derCD23/IDEC152-Fab complex was set up for crystallisation in 0.1 M Tris pH 7.5, 1.8 M ammonium sulfate. Crystals (Figure 6.8) obtained in this condition diffracted to about 2.4 Å resolution.

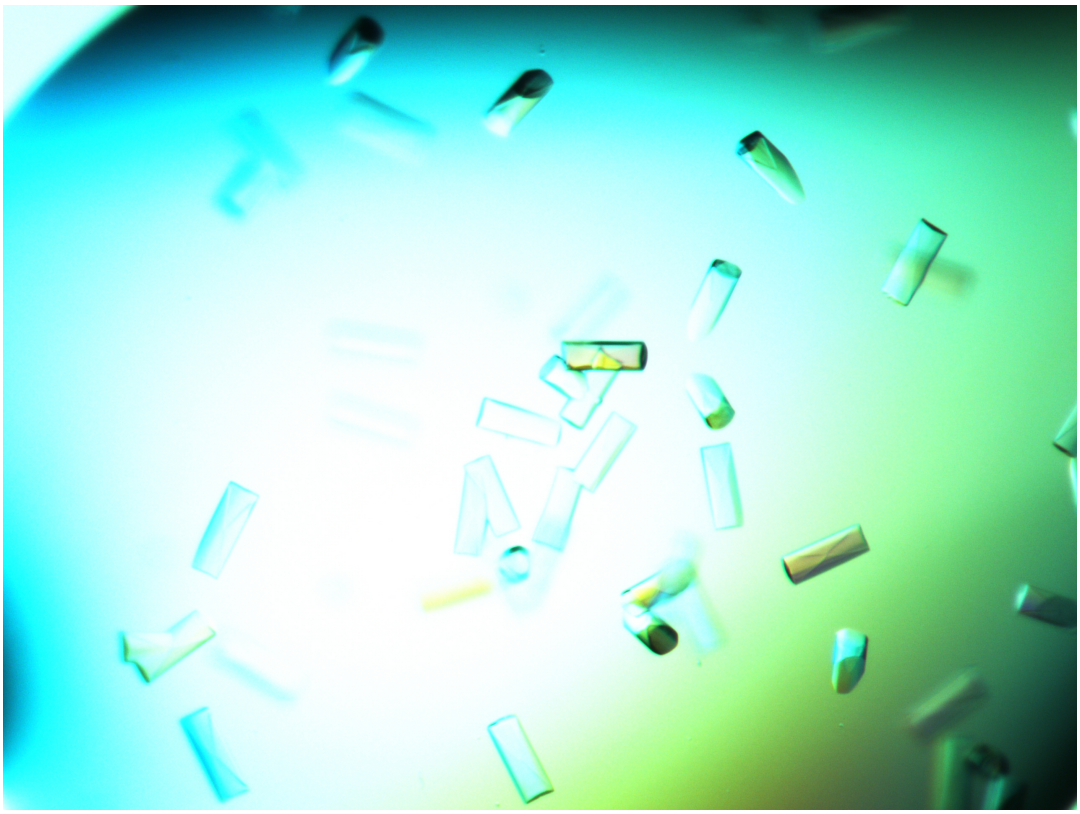

Figure 6.8 Crystals of derCD23/IDEC152-Fab complex.
Crystals of derCD23/IDEC152-Fab complex in 0.1 M Tris pH 7.5, 1.8 M ammonium sulfate using purified complex. The longest dimension of the largest crystal is 200 μm.

6.6 Summary and discussion

This chapter describes the digestion of IDEC152, purification of IDEC152-Fab and crystallisation of the derCD23/IDEC152-Fab complex. The IDEC152-Fab was obtained by papain digestion of IDEC152 IgG antibody and purified using ion exchange chromatography. The crystal screening using mixed derCD23 and IDEC152-Fab at one to one ratio for conditions led to optimized crystals that diffracted to about 3.5 Å

resolution. Because derCD23 binds to IDEC152-Fab with high affinity ($K_A \approx 10^9$ M^{-1}, Dr Balvinder Dhaliwal, unpublished data), it is possible to purify the derCD23/IDEC152-Fab complex for crystallisation. The crystals of the purified complex diffracted to about 2.4 Å resolution.

Quality of protein samples is important for the size and diffraction properties of crystals. Optimization is therefore required not only for crystal growth, but also for the purification of protein samples. This may be particularly important for crystallisation of protein complexes.

The structure of this complex has been solved by Dr. Balvinder Dhaliwal, and a manuscript describing the structure is in preparation.

Chapter 7:
Summary and General Discussion

Allergy is a modern disease that is mainly found in developed countries. IgE plays most important roles in allergic diseases (Sutton and Gould, 1993). It is well established that the role IgE plays in allergic diseases is through its interactions with two receptors: FcεRI (high-affinity Fc receptor) and CD23 (low-affinity Fc receptor). The best characterised function of IgE is performed by interaction with FcεRI on mast cells and basophils mediating immediate hypersensitivity, and on APCs (antigen-presenting cells) presenting allergen to the immune system. CD23 regulates IgE synthesis, and influences the activation and differentiation of B- and T-cells. CD23 also plays important roles in allergen presentation and transporting allergen-IgE complexes across epithelial barriers. The structure of IgE alone, and the complex with FcεRI have been described in detail (Holdom *et al*., 2011; McDonnell *et al*., 2001; Wan *et al*., 2002; Wurzburg *et al*., 2000). However, the structures of CD23 determined by NMR (Hibbert *et al*., 2005) and X-ray crystallography (Wurzburg *et al*., 2006) gave conflicting results concerning calcium binding sites, and no structural information on the IgE/CD23 complex had been reported. In addition, the role of calcium in CD23 binding to IgE remained to be resolved.

IDEC152 is a primatized, IgG1, anti-CD23 monoclonal antibody, which decreases IgE level in serum in clinical trials (Rosenwasser *et al*., 2003) and inhibits allergen-induced responses in antigen-presenting cells and T cells (Poole *et al*., 2005). However, nothing is known of the structural details of IDEC152 binding to CD23.

This thesis describes the crystal structures of Ca^{2+}-bound wild-type derCD23, the complex with the Fcε3-4 sub-fragment of IgE-Fc, and four putative calcium binding site mutants of derCD23. Binding affinities of derCD23 and its mutants for calcium and for IgE-Fc were measured with ITC and SPR. The Fab fragment of IDEC152 IgG was prepared by enzymatic digestion from IDEC152 and crystals of the complex of derCD23 with IDEC152-Fab were grown, which diffracted to 2.4 Å resolution.

7.1 Calcium binding site in derCD23

CD23 is a unique Ig receptor and belongs to the CTLD superfamily (Kikutani *et al*., 1986; Kintner *et al*., 1981; Thorley-Lawson *et al*., 1986). Sequence alignment of Ca^{2+} site ligands in other C-type lectins and various species of CD23 suggested two putative Ca^{2+}-binding sites in human CD23: a poorly conserved "site 1" and a well-conserved "site 2" (Figure 3.2). NMR titration experiments indicated Ca^{2+}-binding to "site 1" (Hibbert *et al*., 2005), but Ca^{2+} was observed in "site 2" in the crystal structure of CD23 double mutant (H213R and G256S) (Figure 3.3A) (Wurzburg *et al*., 2006).

The crystal structure of Ca^{2+}-bound derCD23 at 2 Å resolution shows that calcium binds to "site 2", and has different coordination compared with the previously solved CD23 double mutant crystal structure. Three residues (E249, T251 and D270) provide 4 oxygen atoms and 3 water molecules provide 3 oxygen atoms involved in the binding of calcium. The geometry of the calcium coordination is pentagonal bipyramidal formed by the seven ligands (Section 3.7). The calcium-bound derCD23/Fcε3-4 structure (solved at 3.3 Å resolution) confirms that calcium is bound to "site 2", although the coordination is not so clear due to the limited resolution. According to the alignment of CD23 sequences from various species, N269 is expected to be a calcium ligand, and is seen as such in the derCD23 double mutant structure. Surprisingly, N269 is *not* involved in the binding to Ca^{2+} in this derCD23 structure. Therefore, two mutations of N269 in derCD23 were designed in order to test this observation; it was found that neither mutation weakens calcium binding in ITC, indicating that N269 is not a calcium ligand. Calcium binding to derCD23 causes movement of T251, which drives P250 from the *trans*-conformation to the *cis*-conformation. Isomerisation of this conserved proline residue from *trans* to *cis* for calcium-binding was also observed in mannose-binding protein (Ng *et al*., 1998). The binding affinity of calcium to the other calcium binding site mutants of derCD23, measured by ITC, also supports the coordination of calcium, with the exception of the D258A mutation. Although this residue was excepted to bind calcium, since it is a "site 1" ligand, the crystal structure of this mutant shows that P250 is *trans*, the conformation not preferred for calcium-binding, and furthermore the R253 side chain occupies calcium binding "site 2" (Figure 4.6).

A possible reason for the different coordination in the previously solved crystal structure of CD23 double mutant (Wurzburg *et al*., 2006) is that one of the mutations, G256S, is close to the calcium binding "site 2", and may cause changes in calcium coordination. Comparison of the structures of calcium-bound with calcium-free derCD23 also shows small variations in loop 1, which has two calcium binding "site 1" ligands. This is also consistent with the movement of loop 1 in the NMR titration experiments with calcium, which implied that calcium bound to "site 1" (Hibbert *et al*., 2005).

Carbohydrate binding is a fundamental function of some CTLDs, and this function is limited to calcium binding "site 2" for monosaccharides. But the presence of calcium in "site 2" does not guarantee carbohydrate binding (Zelensky *et al*., 2005). The human CD23 head domain has appearently lost the function to bind carbohydrate (Hibbert *et al*., 2005). The pentagonal bipyramidal geometry of the calcium coordination formed by seven ligands in CD23, instead of the eight ligands in most other carbohydrate binding CTLDs in "site 2", may contribute to the lack of carbohydrate binding by the CD23 head domain. The bisected apex consists of two water molecules in MBP, DC-SIGN and human asialoglycoprotin receptor-I (ASGPR-I) (Meier *et al*., 2000; Snyder *et al*., 2005; Weis *et al*., 1992; Wurzburg *et al*., 2006), while two carbohydrate oxygen atoms occupied this bisected apex in these carbohydrate-bound lectins (Section 3.7). However, an N-linked sugar on domain 5 to 8 of human CD21 was reported to be involved in the CD23/CD21 interaction (Aubry *et al*., 1994). The mechanism for this is still not clear.

7.2 The role calcium plays in CD23 binding to IgE

CD23 regulates IgE synthesis through interaction with IgE and CD21. Structural studies of the IgE/CD23 complex may reveal details of the molecular mechanism of allergic diseases and lead to CD23-targeted drug design. Calcium increases derCD23 binding affinity to IgE-Fc 7-fold as determined in SPR experiments (Hibbert *et al*., 2005). This is confirmed by SPR data reported in this thesis. However, trimeric CD23 binding to IgE may be affected much more than 7-fold by calcium, due to the avidity effect

achieved by the three head domains. Wild-type derCD23 binds calcium with a K_D = 1.5 mM, and the concentration of calcium in human serum is about 2 mM (see chapter 3). This indicates that the calcium-bound and -free CD23 may be in an equilibrium that is sensitive to calcium concentration in physiological conditions. Slight changes of the concentration of calcium in the serum may have large effects on the binding of CD23 to IgE and this affect the regulation of IgE synthesis (Figure 1.7) and other IgE-dependent activities. Comparison of the structures of Ca^{2+}-bound, -free derCD23 and derCD23/Fcε3-4 complexes reveals the role calcium plays in CD23 binding to IgE.

Firstly, the Ca^{2+}-bound derCD23/Fcε3-4 complex confirms that calcium binds to "site 2", and that calcium is not involved in the binding to IgE directly. This indicates that calcium increases the binding affinity of CD23 to IgE by influencing the structure of derCD23.

Secondly, after calcium binding to derCD23 loop 4 is stabilised in a position that is preferred for CD23 binding to IgE. All 6 copies of loop 4 in the Ca^{2+}-bound derCD23/Fcε3-4 complex are ordered, while 5 out of 6 copies of loop 4 in the Ca^{2+}-free structure of the complex are disordered (Dhaliwal *et al*., 2012). Comparison of the structures of Ca^{2+}-bound and Ca^{2+}-free derCD23 also reveals that loop 4 is locked in a particular position after calcium binding. The Ca^{2+}-bound derCD23 has only one conformation for loop 4, whereas two conformations are observed in Ca^{2+}-free derCD23 and some side chains (residues 253-254 in conformation 1) of loop 4 are disordered (Figure 5.12). Calcium-dependent isomerisation of P250 is also involved in the structural changes of loop 4 (Figure 3.15). In the earlier Ca^{2+}-bound structure of CD23 double mutant (Figure 3.3B), the disordered loop 4 (residues 253-257) is inconsistent with the role of Ca^{2+} in stabilizing the loop in other CTLDs (Ng *et al*., 1998; Sun, 2006). A possible reason for this is the unpredicted effect caused by one of the mutations (G256S), which is part of loop 4 in derCD23.

Thirdly, the Ca^{2+}-bound complex reveals new interactions between derCD23 and Fcε3-4. The Ca^{2+}-bound derCD23/Fcε3-4 complex shows two new salt bridges (D258-R440 and D227-R440) between derCD23 and Fcε3-4 after calcium binding (Figure 5.9).

According to an alignment of CD23 sequences in various species and some other C-type lectins, only human CD23 has a poorly conserved calcium binding "site 1" (Figure 3.2). D258 is the only conserved residue in the "site 1", and D227 is a residue that lies between the poorly conserved N225 and K229 residues. It appears that human CD23 lost the function to bind calcium in "site 1", but evolved to bind protein (IgE) directly using "site 1" residue D258.

In contrast with human CD23, the calcium binding "site 1" and "site 2" are *both* well conserved in mouse CD23, and may cause different binding ability of mouse CD23 to mouse IgE, and perhaps further different physiological roles in allergic diseases. In addition, mouse CD23 has a shorter stalk region than human CD23, stronger trimer formation and no C-terminal tail for the binding to CD21. All these differences need to be considered when mouse models are used to study the role of CD23 in allergic diseases.

Finally, calcium bound to derCD23/Fcε3-4 may stabilise the angle between the Cε3 and Cε4 domains. Superposition of the six independent heavy chains of Fcε3-4 in the crystal structure of the calcium-free derCD23/Fcε3-4 complex shows slight variations between the Cε3 and Cε4 domains (Dhaliwal *et al*., 2012). However, the angle between the Cε3 and Cε4 domains remains the same in all the six independent heavy chains in the Ca^{2+}-bound derCD23/Fcε3-4 structure (Section 5.5).

7.3 Structures of putative calcium binding sites mutants

Structures of the calcium binding sites mutants (E249A, S252A, D258A, D270A) of derCD23 were solved to see whether there are unexpected secondary effects in these mutagenesis experiments. Superimposition of wild-type derCD23 and all four mutant structures reveals large differences in loop 4, small differences in loop 1 and essentially the same positions of calcium binding residues (Figure 4.4 and Figure 4.5). These similar positions of calcium binding residues can explain the results of the ITC experiments to measure the binding affinity of calcium, with the exception of D258A. As described above (Section 7.1), the crystal structure of D258A shows that the side

chain of R253 moves to occupy the calcium "site 2".

Large structural differences in loop 4 may be the reason for the unexpected results of the binding affinity of some of these mutants to IgE-Fc by SPR. Calcium increases binding affinity of wild-type derCD23 and the S252A mutant to IgE-Fc 7-fold, which is consistent with previously published SPR data (Hibbert *et al*., 2005). S252A, N269A and N269D can bind calcium (as determined by ITC), therefore they behave in the same way as the binding of wild-type derCD23 to IgE-Fc. However, some of the mutants show unexpected results in their binding affinities to IgE-Fc (Section 4.6). Although E249A and D270A lost the ability to bind calcium, they show binding affinities that are more similar to wild-type derCD23 in the presence of calcium than in the absence of calcium. It is also a surprise to see that the binding affinity between the D258A mutant and IgE-Fc is not measurable in the SPR experiments. One possible reason is disruption of the salt bridge, D258 of derCD23 with R440 of Fcε3-4, which is found in the calcium-bound derCD23/Fcε3-4 structure. Mutation of D258 may also influence other interactions in this region, such as R440 of Fcε3-4 with D227 and Q255 of derCD23. However, further study is needed to answer this question.

7.4 The complex of derCD23 and IDEC152-Fab

Chapter 6 reports the digestion of IDEC152 IgG, purification of IDEC152-Fab and crystallisation of the derCD23/IDEC152-Fab complex. The crystals of purified derCD23/IDEC152-Fab complex diffracted to higher resolution than those grown after mixing these two proteins together in the crystallisation drop. The structure of this complex has been solved by Dr. Balvinder Dhaliwal, and a manuscript is in preparation.

References

Aalberse, R.C., and Schuurman, J. (2002). IgG4 breaking the rules. Immunology *105*, 9-19.

Adams, P.D., Afonine, P.V., Bunkoczi, G., Chen, V.B., Echols, N., Headd, J.J., Hung, L.W., Jain, S., Kapral, G.J., Grosse Kunstleve, R.W., McCoy, A.J., Moriarty, N.W., Oeffner, R.D., Read, R.J., Richardson, D.C., Richardson, J.S., Terwilliger T.C., and Zwart, P.H. (2011). The Phenix software for automated determination of macromolecular structures. Methods *55*, 94-106.

Asherie, N. (2004). Protein crystallization and phase diagrams. Methods *34*, 266-272.

Aubry, J.P., Pochon, S., Gauchat, J.F., Nueda-Marin, A., Holers, V.M., Graber, P., Siegfried, C., and Bonnefoy, J.Y. (1994). CD23 interacts with a new functional extracytoplasmic domain involving N-linked oligosaccharides on CD21. Journal of Immunology *152*, 5806-5813.

Aubry, J.P., Pochon, S., Graber, P., Jansen, K.U., and Bonnefoy, J.Y. (1992). CD21 is a ligand for CD23 and regulates IgE production. Nature *358*, 505-507.

Bajorath, J., and Aruffo, A. (1996). Structure-based modeling of the ligand binding domain of the human cell surface receptor CD23 and comparison of two independently derived molecular models. Protein Science *5*, 240-247.

Basu, M., Hakimi, J., Dharm, E., Kondas, J.A., Tsien, W.H., Pilson, R.S., Lin, P., Gilfillan, A., Haring, P., Braswell, E.H., Nettleton, M.Y., and Kochan, J.P. (1993). Purification and characterization of human recombinant IgE-Fc fragments that bind to the human high affinity IgE receptor. Journal of Biological Chemistry *268*, 13118-13127.

Battye, T.G., Kontogiannis, L., Johnson, O., Powell, H.R., and Leslie, A.G. (2011). iMOSFLM: a new graphical interface for diffraction-image processing with MOSFLM. Acta Crystallographica. Section D, Biological Crystallography *67*, 271-281.

Beavil, A.J., Edmeades, R.L., Gould, H.J., and Sutton, B.J. (1992). Alpha-helical coiled-coil stalks in the low-affinity receptor for IgE (FcεRII/CD23) and related C-type lectins. Proceedings of the National Academy of Sciences of the United States of America *89*, 753-757.

Beck, T., da Cunha, C.E., and Sheldrick, G.M. (2009). How to get the magic triangle and the MAD triangle into your protein crystal. Acta crystallographica. Section F, Structural Biology and Crystallization Communications *65*, 1068-1070.

Bergfors, T. (2003). Seeds to crystals. Journal of Structural Biology *142*, 66-76.

Bestagno, M., Vangelista, L., Mandiola, P.A., Mukherjee, S., Sepulveda, J., and Burrone, O.R. (2001). Membrane immunoglobulins are stabilized by interchain disulfide bonds occurring within the extracellular membrane-proximal domain. Biochemistry *40*, 10686-10692.

Bettler, B., Maier, R., Ruegg, D., and Hofstetter, H. (1989). Binding site for IgE of the human lymphocyte low-affinity Fc epsilon receptor (FcεRII/CD23) is confined to the domain homologous with animal lectins. Proceedings of the National Academy of Sciences of the United States of America *86*, 7118-7122.

Bettler, B., Texido, G., Raggini, S., Ruegg, D., and Hofstetter, H. (1992). Immunoglobulin E-binding site in Fc epsilon receptor (FcεRII/CD23) identified by homolog-scanning mutagenesis. Journal of Biological Chemistry *267*, 185-191.

Billaud, M., Busson, P., Huang, D., Mueller-Lantzch, N., Rousselet, G., Pavlish, O., Wakasugi, H., Seigneurin, J.M., Tursz, T., and Lenoir, G.M. (1989). Epstein-Barr virus (EBV)-containing nasopharyngeal carcinoma cells express the B-cell activation antigen

blast2/CD23 and low levels of the EBV receptor CR2. Journal of Virology *63*, 4121-4128.

Bjorklund, J.E., Karlsson, T., and Magnusson, C.G. (1999). N-glycosylation influences epitope expression and receptor binding structures in human IgE. Molecular Immunology *36*, 213-221.

Bonnefoy, J.Y., Gauchat, J.F., Life, P., Graber, P., Mazzei, G., and Aubry, J.P. (1996). Pairs of surface molecules involved in human IgE regulation: CD23-CD21 and CD40-CD40L. European Respiratory Journal. Supplement *22*, 63s-66s.

Bonnefoy, J.Y., Henchoz, S., Hardie, D., Holder, M.J., and Gordon, J. (1993). A subset of anti-CD21 antibodies promote the rescue of germinal center B cells from apoptosis. European Journal of Immunology *23*, 969-972.

Borthakur, S., Hibbert, R.G., Pang, M.O., Yahya, N., Bax, H.J., Kao, M.W., Cooper, A.M., Beavil, A.J., Sutton, B.J., Gould, H.J., and McDonnell, J.M. (2012). Mapping of the CD23 binding site on IgE and allosteric control of the IgE-FcεRI interaction. Journal of Biological Chemistry.

Byrd, J.C., O'Brien, S., Flinn, I.W., Kipps, T.J., Weiss, M., Rai, K., Lin, T.S., Woodworth, J., Wynne, D., Reid, J., Molina, A., Leigh, B., and Harris, S. (2007). Phase 1 study of lumiliximab with detailed pharmacokinetic and pharmacodynamic measurements in patients with relapsed or refractory chronic lymphocytic leukemia. Clinical Cancer Research *13*, 4448-4455.

Capron, M., Capron, A., Dessaint, J.P., Torpier, G., Johansson, S.G., and Prin, L. (1981). Fc receptors for IgE on human and rat eosinophils. Journal of Immunology *126*, 2087-2092.

Carlsson, F., Hjelm, F., Conrad, D.H., and Heyman, B. (2007). IgE enhances specific antibody and T-cell responses in mice overexpressing CD23. Scandinavian Journal of

Immunology *66*, 261-270.

Chen, V.B., Arendall, W.B., 3rd, Headd, J.J., Keedy, D.A., Immormino, R.M., Kapral, G.J., Murray, L.W., Richardson, J.S., and Richardson, D.C. (2010). MolProbity: all-atom structure validation for macromolecular crystallography. Acta Crystallographica. Section D, Biological Crystallography *66*, 12-21.

Chretien, I., Helm, B.A., Marsh, P.J., Padlan, E.A., Wijdenes, J., and Banchereau, J. (1988). A monoclonal anti-IgE antibody against an epitope (amino acids 367-376) in the CH3 domain inhibits IgE binding to the low affinity IgE receptor (CD23). Journal of Immunology *141*, 3128-3134.

Cooper, A.M., Hobson, P.S., Jutton, M.R., Kao, M.W., Drung, B., Schmidt, B., Fear, D.J., Beavil, A.J., McDonnell, J.M., Sutton, B.J., and Gould, H.J. (2012). Soluble CD23 Controls IgE Synthesis and Homeostasis in Human B Cells. Journal of Immunology *188*, 3199-3207.

Cooper, M.A. (2002). Optical biosensors in drug discovery. Nature Reviews Drug Discovery *1*, 515-528.

Dauter, Z. (1999). Data-collection strategies. Acta Crystallographica. Section D, Biological Crystallography *55*, 1703-1717.

Delespesse, G., Suter, U., Mossalayi, D., Bettler, B., Sarfati, M., Hofstetter, H., Kilcherr, E., Debre, P., and Dalloul, A. (1991). Expression, structure, and function of the CD23 antigen. Advances in Immunology *49*, 149-191.

Dhaliwal, B., Yuan, D., Pang, M.O.Y., Henry, A.J., Cain, K., Oxbrow, A., Fabiane, S.M., Beavil, A.J., McDonnell, J.M., Gould, H.J., and Sutton, B.J. (2012). Crystal structure of IgE bound to its B-cell receptor CD23 reveals a mechanism of reciprocal allosteric inhibition with high affinity receptor FcεRI. Proceedings of the National Academy of Sciences of the United States of America *109*, 12686-12691.

Dierks, S.E., Bartlett, W.C., Edmeades, R.L., Gould, H.J., Rao, M., and Conrad, D.H. (1993). The oligomeric nature of the murine FcεRII/CD23. Implications for function. Journal of Immunology *150*, 2372-2382.

Drickamer, K. (1999). C-type lectin-like domains. Current Opinion in Structural Biology *9*, 585-590.

Emsley, P., Lohkamp, B., Scott, W.G., and Cowtan, K. (2010). Features and development of Coot. Acta Crystallographica. Section D, Biological Crystallography *66*, 486-501.

Evans, P. (2006). Scaling and assessment of data quality. Acta Crystallographica. Section D, Biological Crystallography *62*, 72-82.

Evans, P., and McCoy, A. (2008). An introduction to molecular replacement. Acta Crystallographica. Section D, Biological Crystallography *64*, 1-10.

Evans, P.R. (1999). Some notes on choices in data collection. Acta Crystallographica. Section D, Biological Crystallography *55*, 1771-1772.

Fernandez, E.J., Joachimiak, A., and Lolis, E. (2000). A cryocooling technique for protein crystals grown by dialysis from volatile solvents. Journal of Applied Crystallography *33*, 168-171.

Frey, M. (1994). Water-Structure Associated with Proteins and Its Role in Crystallization. Acta Crystallographica. Section D, Biological Crystallography *50*, 663-666.

Garman, E. (1999). Cool data: quantity AND quality. Acta Crystallographica. Section D, Biological Crystallography *55*, 1641-1653.

Garman, E.F. (2010). Radiation damage in macromolecular crystallography: what is it and why should we care? Acta Crystallographica. Section D, Biological Crystallography *66*, 339-351.

Garman, E.F., and Schneider, T.R. (1997). Macromolecular cryocrystallography. Journal of Applied Crystallography *30*, 211-237.

Garman, S.C., Wurzburg, B.A., Tarchevskaya, S.S., Kinet, J.P., and Jardetzky, T.S. (2000). Structure of the Fc fragment of human IgE bound to its high-affinity receptor FcεRIα. Nature *406*, 259-266.

Geha, R.S., Helm, B., and Gould, H. (1985). Inhibition of the Prausnitz-Kustner reaction by an immunoglobulin epsilon-chain fragment synthesized in E. coli. Nature *315*, 577-578.

Gonzalez-Molina, A., and Spiegelberg, H.L. (1976). Binding of IgE myeloma proteins to human cultured lymphoblastoid cells. Journal of Immunology *117*, 1838-1845.

Gordon, J. (1991). CD23: novel disease marker with a split personality. Clinical and Experimental Immunology *86*, 356-359.

Gould, H.J., and Sutton, B.J. (2008). IgE in allergy and asthma today. Nature Reviews Immunology *8*, 205-217.

Gould, H.J., Sutton, B.J., Beavil, A.J., Beavil, R.L., McCloskey, N., Coker, H.A., Fear, D., and Smurthwaite, L. (2003). The biology of IgE and the basis of allergic disease. Annual Review of Immunology *21*, 579-628.

Harp, J.M., Timm, D.E., and Bunick, G.J. (1998). Macromolecular crystal annealing: overcoming increased mosaicity associated with cryocrystallography. Acta Crystallographica. Section D, Biological Crystallography *54*, 622-628.

Hassell, A.M., An, G., Bledsoe, R.K., Bynum, J.M., Carter, H.L., 3rd, Deng, S.J., Gampe, R.T., Grisard, T.E., Madauss, K.P., Nolte, R.T., Rocque, W.J., Wang, L., Weaver, K.L., Williams, S.P., Wisely, G.B., Xu, R., and Shewchuk, L.M. (2007). Crystallization of protein-ligand complexes. Acta Crystallographica. Section D, Biological Crystallography *63*, 72-79.

Helm, B., Marsh, P., Vercelli, D., Padlan, E., Gould, H., and Geha, R. (1988). The mast cell binding site on human immunoglobulin E. Nature *331*, 180-183.

Helm, B.A., Ling, Y., Teale, C., Padlan, E.A., and Bruggemann, M. (1991). The nature and importance of the inter-epsilon chain disulfide bonds in human IgE. European Journal of Immunology *21*, 1543-1548.

Heras, B., and Martin, J.L. (2005). Post-crystallization treatments for improving diffraction quality of protein crystals. Acta Crystallographica. Section D, Biological Crystallography *61*, 1173-1180.

Hibbert, R.G., Teriete, P., Grundy, G.J., Beavil, R.L., Reljic, R., Holers, V.M., Hannan, J.P., Sutton, B.J., Gould, H.J., and McDonnell, J.M. (2005). The structure of human CD23 and its interactions with IgE and CD21. The Journal of Experimental Medicine *202*, 751-760.

Holdom, M.D., Davies, A.M., Nettleship, J.E., Bagby, S.C., Dhaliwal, B., Girardi, E., Hunt, J., Gould, H.J., Beavil, A.J., McDonnell, J.M., Owens, R.J., and Sutton, B.J. (2011). Conformational changes in IgE contribute to its uniquely slow dissociation rate from receptor FcεRI. Nature Structural & Molecular Biology *18*, 571-576.

Hope, H. (1990). Crystallography of biological macromolecules at ultra-low temperature. Annual Review of Biophysics and Biophysical Chemistry *19*, 107-126.

Jackson, M. (2001). Allergy: the making of a modern plague. Clinical and Experimental

Allergy *31*, 1665-1671.

Keegan, A.D., Fratazzi, C., Shopes, B., Baird, B., and Conrad, D.H. (1991). Characterization of new rat anti-mouse IgE monoclonals and their use along with chimeric IgE to further define the site that interacts with FcεRII and FcεRI. Molecular Immunology *28*, 1149-1154.

Kessler, H., Mronga, S., Muller, G., Moroder, L., and Huber, R. (1991). Conformational analysis of a IgG1 hinge peptide derivative in solution determined by NMR spectroscopy and refined by restrained molecular dynamics simulations. Biopolymers *31*, 1189-1204.

Kikutani, H., Inui, S., Sato, R., Barsumian, E.L., Owaki, H., Yamasaki, K., Kaisho, T., Uchibayashi, N., Hardy, R.R., Hirano, T., Tsunasawa, S., Sakiyama, F., Suemura, M., and Kishimoto,T. (1986). Molecular structure of human lymphocyte receptor for immunoglobulin E. Cell *47*, 657-665.

Kim, Y., and Haren, A.M. (1995). The application of crystal soaking technique to study the effect of zinc and cresol on insulinotropin crystals grown from a saline solution. Pharmaceutical Research *12*, 1664-1670.

Kintner, C., and Sugden, B. (1981). Identification of antigenic determinants unique to the surfaces of cells transformed by Epstein-Barr virus. Nature *294*, 458-460.

Kriminski, S., Caylor, C.L., Nonato, M.C., Finkelstein, K.D., and Thorne, R.E. (2002). Flash-cooling and annealing of protein crystals. Acta Crystallographica. Section D, Biological Crystallography *58*, 459-471.

Laemmli, U.K. (1970). Cleavage of structural proteins during the assembly of the head of bacteriophage T4. Nature *227*, 680-685.

Lawrence, D.A., Weigle, W.O., and Spiegelberg, H.L. (1975). Immunoglobulins

cytophilic for human lymphocytes, monocytes, and neutrophils. The Journal of Clinical Investigation *55*, 368-376.

Lecoanet-Henchoz, S., Gauchat, J.F., Aubry, J.P., Graber, P., Life, P., Paul-Eugene, N., Ferrua, B., Corbi, A.L., Dugas, B., Plater-Zyberk, C., and Bonnefoy, J.Y. (1995). CD23 regulates monocyte activation through a novel interaction with the adhesion molecules CD11b-CD18 and CD11c-CD18. Immunity *3*, 119-125.

Lemieux, G.A., Blumenkron, F., Yeung, N., Zhou, P., Williams, J., Grammer, A.C., Petrovich, R., Lipsky, P.E., Moss, M.L., and Werb, Z. (2007). The low affinity IgE receptor (CD23) is cleaved by the metalloproteinase ADAM10. Journal of Biological Chemistry *282*, 14836-14844.

Liu, Y.J., Cairns, J.A., Holder, M.J., Abbot, S.D., Jansen, K.U., Bonnefoy, J.Y., Gordon, J., and MacLennan, I.C. (1991). Recombinant 25-kDa CD23 and interleukin 1 alpha promote the survival of germinal center B cells: evidence for bifurcation in the development of centrocytes rescued from apoptosis. European Journal of Immunology *21*, 1107-1114.

Loeb, J.A., and Drickamer, K. (1988). Conformational changes in the chicken receptor for endocytosis of glycoproteins. Modulation of ligand-binding activity by Ca2+ and pH. Journal of Biological Chemistry *263*, 9752-9760.

Matthews, B.W. (1968). Solvent content of protein crystals. Journal of Molecular Biology *33*, 491-497.

Mavromatis, B.H., and Cheson, B.D. (2004). Novel therapies for chronic lymphocytic leukemia. Blood Reviews *18*, 137-148.

McCloskey, N., Hunt, J., Beavil, R.L., Jutton, M.R., Grundy, G.J., Girardi, E., Fabiane, S.M., Fear, D.J., Conrad, D.H., Sutton, B.J., and Gould, H.J. (2007). Soluble CD23 monomers inhibit and oligomers stimulate IGE synthesis in human B cells. Journal of

Biological Chemistry *282*, 24083-24091.

McCoy, A.J., Grosse-Kunstleve, R.W., Adams, P.D., Winn, M.D., Storoni, L.C., and Read, R.J. (2007). Phaser crystallographic software. Journal of Applied Crystallography *40*, 658-674.

McDonnell, J.M., Calvert, R., Beavil, R.L., Beavil, A.J., Henry, A.J., Sutton, B.J., Gould, H.J., and Cowburn, D. (2001). The structure of the IgE Cε2 domain and its role in stabilizing the complex with its high-affinity receptor FcεRIα. Nature Structural Biology *8*, 437-441.

Meier, M., Bider, M.D., Malashkevich, V.N., Spiess, M., and Burkhard, P. (2000). Crystal structure of the carbohydrate recognition domain of the H1 subunit of the asialoglycoprotein receptor. Journal of Molecular Biology *300*, 857-865.

Melewicz, F.M., Kline, L.E., Cohen, A.B., and Spiegelberg, H.L. (1982). Characterization of Fc receptors for IgE on human alveolar macrophages. Clinical and Experimental Immunology *49*, 364-370.

Miescher, S.M., and Vogel, M. (2002). Molecular aspects of allergy. Molecular Aspects of Medicine *23*, 413-462.

Mimura, Y., Sondermann, P., Ghirlando, R., Lund, J., Young, S.P., Goodall, M., and Jefferis, R. (2001). Role of oligosaccharide residues of IgG1-Fc in Fc gamma RIIb binding. Journal of Biological Chemistry *276*, 45539-45547.

Mudde, G.C., Bheekha, R., and Bruijnzeel-Koomen, C.A. (1995). Consequences of IgE/CD23-mediated antigen presentation in allergy. Immunology Today *16*, 380-383.

Murshudov, G.N., Skubak, P., Lebedev, A.A., Pannu, N.S., Steiner, R.A., Nicholls, R.A., Winn, M.D., Long, F., and Vagin, A.A. (2011). REFMAC5 for the refinement of macromolecular crystal structures. Acta Crystallographica. Section D, Biological

Crystallography *67*, 355-367.

Nave, C. (1999). Matching X-ray source, optics and detectors to protein crystallography requirements. Acta Crystallographica. Section D, Biological Crystallography *55*, 1663-1668.

Ng, K.K., Park-Snyder, S., and Weis, W.I. (1998). Ca2+-dependent structural changes in C-type mannose-binding proteins. Biochemistry *37*, 17965-17976.

Ng, K.K., and Weis, W.I. (1998). Coupling of prolyl peptide bond isomerization and Ca2+ binding in a C-type mannose-binding protein. Biochemistry *37*, 17977-17989.

Nissim, A., Jouvin, M.H., and Eshhar, Z. (1991). Mapping of the high affinity Fc epsilon receptor binding site to the third constant region domain of IgE. The European Molecular Biology Organization Journal *10*, 101-107.

Otwinowski, Z., and Minor, W. (1997). Processing of X-ray diffraction data collected in oscillation mode. Methods in Enzymology *276*, 307-326.

Padlan, E.A., and Davies, D.R. (1986). A model of the Fc of immunoglobulin E. Molecular Immunology *23*, 1063-1075.

Padlan, E.A., and Helm, B.A. (1993). Modeling of the lectin-homology domains of the human and murine low-affinity Fc epsilon receptor (FcεRII/CD23). Receptor *3*, 325-341.

Painter, J., and Merritt, E.A. (2006). Optimal description of a protein structure in terms of multiple groups undergoing TLS motion. Acta Crystallographica. Section D, Biological Crystallography *62*, 439-450.

Palaniyandi, S., Tomei, E., Li, Z., Conrad, D.H., and Zhu, X. (2011). CD23-dependent transcytosis of IgE and immune complex across the polarized human respiratory

epithelial cells. Journal of Immunology *186*, 3484-3496.

Pflugrath, J.W. (2004). Macromolecular cryocrystallography--methods for cooling and mounting protein crystals at cryogenic temperatures. Methods *34*, 415-423.

Poole, J.A., Meng, J., Reff, M., Spellman, M.C., and Rosenwasser, L.J. (2005). Anti-CD23 monoclonal antibody, lumiliximab, inhibited allergen-induced responses in antigen-presenting cells and T cells from atopic subjects. The Journal of Allergy and Clinical Immunology *116*, 780-788.

Prota, A.E., Sage, D.R., Stehle, T., and Fingeroth, J.D. (2002). The crystal structure of human CD21: Implications for Epstein-Barr virus and C3d binding. Proceedings of the National Academy of Sciences of the United States of America *99*, 10641-10646.

Ramachandran, G.N., Ramakrishnan, C., and Sasisekharan, V. (1963). Stereochemistry of polypeptide chain configurations. Journal of Molecular Biology *7*, 95-99.

Ramakrishnan, C., and Ramachandran, G.N. (1965). Stereochemical criteria for polypeptide and protein chain conformations. II. Allowed conformations for a pair of peptide units. Biophysical Journal *5*, 909-933.

Richards, M.L., and Katz, D.H. (1990). The binding of IgE to murine FcεRII is calcium-dependent but not inhibited by carbohydrate. Journal of Immunology *144*, 2638-2646.

Roozendaal, R., and Carroll, M.C. (2007). Complement receptors CD21 and CD35 in humoral immunity. Immunological Reviews *219*, 157-166.

Rosenwasser, L.J., Busse, W.W., Lizambri, R.G., Olejnik, T.A., and Totoritis, M.C. (2003). Allergic asthma and an anti-CD23 mAb (IDEC-152): results of a phase I, single-dose, dose-escalating clinical trial. The Journal of Allergy and Clinical Immunology *112*, 563-570.

Rosenwasser, L.J., and Meng, J. (2005). Anti-CD23. Clinical Reviews in Allergy & Immunology *29*, 61-72.

Rubinson, K.A., Ladner, J.E., Tordova, M., and Gilliland, G.L. (2000). Cryosalts: suppression of ice formation in macromolecular crystallography. Acta Crystallographica. Section D, Biological Crystallography *56*, 996-1001.

Salunke, D.M., Veerapandian, B., Kodandapani, R., and Vijayan, M. (1985). Water-Mediated Transformations in Protein Crystals. Acta Crystallographica. Section B, Structural Science *41*, 431-436.

Sarfati, M., Nutman, T., Fonteyn, C., and Delespesse, G. (1986). Presence of antigenic determinants common to Fc IgE receptors on human macrophages, T and B lymphocytes and IgE-binding factors. Immunology *59*, 569-575.

Sayers, I., Housden, J.E., Spivey, A.C., and Helm, B.A. (2004). The importance of Lys-352 of human immunoglobulin E in FcεRII/CD23 recognition. Journal of Biological Chemistry *279*, 35320-35325.

Schulz, O., Laing, P., Sewell, H.F., and Shakib, F. (1995). Der p I, a major allergen of the house dust mite, proteolytically cleaves the low-affinity receptor for human IgE (CD23). European Journal of Immunology *25*, 3191-3194.

Schulz, O., Sutton, B.J., Beavil, R.L., Shi, J., Sewell, H.F., Gould, H.J., Laing, P., and Shakib, F. (1997). Cleavage of the low-affinity receptor for human IgE (CD23) by a mite cysteine protease: nature of the cleaved fragment in relation to the structure and function of CD23. European Journal of Immunology *27*, 584-588.

Shi, J., Ghirlando, R., Beavil, R.L., Beavil, A.J., Keown, M.B., Young, R.J., Owens, R.J., Sutton, B.J., and Gould, H.J. (1997). Interaction of the low-affinity receptor CD23/FcεRII lectin domain with the Fcε3-4 fragment of human immunoglobulin E.

Biochemistry *36*, 2112-2122.

Snyder, G.A., Colonna, M., and Sun, P.D. (2005). The structure of DC-SIGNR with a portion of its repeat domain lends insights to modeling of the receptor tetramer. Journal of Molecular Biology *347*, 979-989.

Sousa, R. (1995). Use of glycerol, polyols and other protein structure stabilizing agents in protein crystallization. Acta Crystallographica. Section D, Biological Crystallography *51*, 271-277.

Stanworth, D.R. (1993). The discovery of IgE. Allergy *48*, 67-71.

Sun, P.D. (2006). Human CD23: is it a lectin in disguise? Structure *14*, 950-951.

Sutton, B.J., and Gould, H.J. (1993). The human IgE network. Nature *366*, 421-428.

Szakonyi, G., Guthridge, J.M., Li, D., Young, K., Holers, V.M., and Chen, X.S. (2001). Structure of complement receptor 2 in complex with its C3d ligand. Science *292*, 1725-1728.

Tao, M.H., and Morrison, S.L. (1989). Studies of aglycosylated chimeric mouse-human IgG. Role of carbohydrate in the structure and effector functions mediated by the human IgG constant region. Journal of Immunology *143*, 2595-2601.

Thorley-Lawson, D.A., Swendeman, S.L., and Edson, C.M. (1986). Biochemical analysis suggests distinct functional roles for the BLAST-1 and BLAST-2 antigens. Journal of Immunology *136*, 1745-1751.

Tu, Y., Salim, S., Bourgeois, J., Di Leo, V., Irvine, E.J., Marshall, J.K., and Perdue, M.H. (2005). CD23-mediated IgE transport across human intestinal epithelium: inhibition by blocking sites of translation or binding. Gastroenterology *129*, 928-940.

Vercelli, D., Helm, B., Marsh, P., Padlan, E., Geha, R.S., and Gould, H. (1989). The B-cell binding site on human immunoglobulin E. Nature *338*, 649-651.

Wan, T., Beavil, R.L., Fabiane, S.M., Beavil, A.J., Sohi, M.K., Keown, M., Young, R.J., Henry, A.J., Owens, R.J., Gould, H.J., and Sutton, B.J. (2002). The crystal structure of IgE Fc reveals an asymmetrically bent conformation. Nature Immunology *3*, 681-686.

Weber, P.C. (1997). Overview of protein crystallization methods. Methods in Enzymology *276*, 13-22.

Weis, W.I., Drickamer, K., and Hendrickson, W.A. (1992). Structure of a C-type mannose-binding protein complexed with an oligosaccharide. Nature *360*, 127-134.

Weskamp, G., Ford, J.W., Sturgill, J., Martin, S., Docherty, A.J., Swendeman, S., Broadway, N., Hartmann, D., Saftig, P., Umland, S., Sehara-Fujisawa, A., Black, R.A., Ludwig, A., Becherer, J.D., Conrad, D.H., Blobel, C.P. (2006). ADAM10 is a principal 'sheddase' of the low-affinity immunoglobulin E receptor CD23. Nature Immunology *7*, 1293-1298.

Wurzburg, B.A., Garman, S.C., and Jardetzky, T.S. (2000). Structure of the human IgE-Fc Cε3-Cε4 reveals conformational flexibility in the antibody effector domains. Immunity *13*, 375-385.

Wurzburg, B.A., Tarchevskaya, S.S., and Jardetzky, T.S. (2006). Structural changes in the lectin domain of CD23, the low-affinity IgE receptor, upon calcium binding. Structure *14*, 1049-1058.

Yeh, J.I., and Hol, W.G. (1998). A flash-annealing technique to improve diffraction limits and lower mosaicity in crystals of glycerol kinase. Acta Crystallographica. Section D, Biological Crystallography *54*, 479-480.

Yokota, A., Kikutani, H., Tanaka, T., Sato, R., Barsumian, E.L., Suemura, M., and Kishimoto, T. (1988). Two species of human Fc epsilon receptor II (FcεRII/CD23): tissue-specific and IL-4-specific regulation of gene expression. Cell *55*, 611-618.

Zelensky, A.N., and Gready, J.E. (2005). The C-type lectin-like domain superfamily. Federation of European Biochemical Societies Journal *272*, 6179-6217.